Simplifying Biological Assays Using Open Microscale Platforms

By
Duane S. Juang

A dissertation submitted in partial fulfillment of
the requirements for the degree of

Doctor of Philosophy
(Biomedical Engineering)

at the
UNIVERSITY OF WISCONSIN-MADISON
2021

Date of final oral examination: 08/04/2021

The dissertation is approved by the following members of the Final Oral Committee:

David J. Beebe, Professor, Biomedical Engineering
Joshua M. Lang, Associate Professor, Department of Medicine
Jo Handelsman, Professor, Wisconsin Institute for Discovery
Ophelia S. Venturelli, Assistant Professor, Biochemistry
Aviad Hai, Assistant Professor, Biomedical Engineering

To family and friends.

Acknowledgements

I need to thank Dr. David Beebe for giving me so much freedom and encouragement to explore new ideas, but also helping me stay anchored to what's important when I wander off course. You are truly a wonderful mentor, not just in science, but also in showing me the importance of setting priorities in life. I really appreciate my committee, Drs. Joshua Lang, Jo Handelsman, Ophelia Venturelli, and Aviad Hai for providing guidance on my scientific endeavors. I'm grateful to my mentors from the MMB lab and collaborating labs, Scott Berry for introducing me to the world of sample extraction technologies and teaching me grant writing skills, Chao Li for generously sharing his knowledge on surface chemistry and material science, Jamie Sperger for teaching me molecular biology techniques and encouraging me even when my assays don't work, Gabriel Lozano for tirelessly mentoring me on microbiology and experimental design, Layla Barkal for asking important scientific questions and making smart life decisions (such as trying to graduate in 4 years). Will Wightman for being an absolutely outstanding undergrad researcher, all my fellow lab mates and collaborators, especially Jay Warrick, Jason Yu, Mouhita Humayun, Tamara Rodems for their encouragement and tireless discussions in science, and Terry Juang, for being a great brother and partner in research. And of course, the world's best lab manager Pete Geiger, for always being there to help and putting up with my strange order requests, and Alice Golubiewski for guiding me through administrative jungles.

To my Mom and Dad, for their love and encouragement, and for telling me to pursue dreams, not wealth. To Yun-Han, for being so supportive and bringing joy into my life. Lastly, to my wonderful friends who made my PhD life so much more fun and colorful.

Abstract

Precision medicine, heralded to be one of the next major advancements in medical treatment and disease prevention, involves the holistic integration of multiple levels of biological information from the individual, including lifestyle, environment, and diagnostic data from various clinical assays, to provide more accurate disease diagnostics and tailored treatment strategies. Recent years have seen dramatic advancements in genomic technologies which can identify hereditary genetic risk factors of disease. However, many disease risk factors, biomarkers or treatment targets are more affected by “nurture” (i.e. lifestyle/environment) than “nature” (genomic sequence), such as the epigenome, human microbiome, and exposure to infectious diseases. However, current technologies for studying or profiling of these non-hereditary biomarkers are often complex, costly, or require a large abundance of sample, hampering their broader accessibility to the public.

The primary focus of my PhD work is in developing open, accessible platforms for simplifying previously challenging biological assays to accelerate diagnostics and discovery in these fields. Two major platforms which enable a broad range of bioassays are developed in my PhD work: 1) a multi-liquid-phase microfluidic system called the Oil Immersed Lossless Total Analysis System (OIL-TAS) for performing efficient, low-loss analyte processing and analysis for epigenetic assays and COVID-19 diagnostics (chapters 2-3); and 2) a Microbial Community Fitness Landscape (μCFL) platform for assaying polymicrobial interactions (chapter 6). Chapter 4 is an extension of the OIL-TAS technology, describing an efficient reagent delivery method for microscale assay systems, and chapter 5 reports an alternative sample extraction technology with similar physical principles as the OIL-TAS, but does not require any custom devices or instrumentation.

Although the various assay platforms presented in this dissertation are designed to target different biological questions, at a high level the end goal is to provide simple and accessible tools to better explore and measure the complex parameter space in human diseases.

List of Figures

List of Tables

Contents

Chapter 1

Introduction

Modern day medical diagnostics are heavily based on the core philosophies of the scientific method: making observations (i.e., a patient is experiencing symptoms), asking a question (why does the patient have these symptoms?), forming a hypothesis (perform an initial diagnosis to narrow down the potential disease cause), performing experiments (perform diagnostic assays or treatments to test the hypothesis), analysis (examine the diagnostic test results or initial treatment efficacy to determine if the diagnosis was correct), and if the analysis suggests otherwise, re-evaluate. This approach is rigorous, allows for cost reduction/more efficient use of limited medical resources, and avoids undue treatment of non-diseased individuals. However, it's also a somewhat passive and retrospective approach to medicine (i.e., the process only begins after the patient reports symptoms), and only tests for diseases which conform to the symptoms, and as such, one can only find the diseases they're testing for. The passive approach to diagnostics also has other drawbacks including missed treatment opportunities (many diseases don't start showing symptoms until after the golden window for treatment has passed) or failing to catch asymptomatic diseases (underscored by the widespread asymptomatic transmission of COVID-19).

I think there is potential for future medical diagnostics to become more proactive (i.e., actively test for diseases before symptoms arise), less targeted (testing for a wide range of diseases, not just what one's looking for), and morph into the background of normal everyday life, subconsciously keeping track of an individual's health, only resurfacing to

alert the individual before or at the early stages of a disease. I'd like to call this approach "ambient diagnostics".

However, there are significant technological hurdles to overcome in order to realize the goal of ambient diagnostics. Modern *in vitro* diagnostic assays are often slow, labor intensive, single plex (i.e., only tests for one target at a time), and prohibitively expensive. Moreover, many are commonly designed to work with an abundance of sample which are invasively acquired (i.e., a tube of blood, a tissue biopsy, etc.), making patient self-collection unfeasible. As such, there is an unmet need for diagnostic assays which can operate with less sample, greater multiplexing capability, higher sensitivity, faster turnaround, less manual operation, and much lower cost, to make medical diagnostics more accessible to the public.

Many of these needed improvements to *in vitro* diagnostic assays can potentially be realized using microfluidic/microscale technologies, in which their microscale nature affords various advantages including low sample consumption (because of their microscale volumes), assay sensitivity (smaller volumes mean that rare samples can be more concentrated with shorter diffusion distances), reduced cost (smaller volumes reduces reagent consumption), and increased throughput and multiplexing capability for performing complex assays.

In my PhD research, I employ a microscale technology called "open microfluidics", which refers to microscale fluid systems where at least one boundary of the fluidic system is open, and fluid behavior is primarily modulated by surface tension. Open microfluidics have the advantage of being easily accessible (compared to traditional closed-channel microfluidics) and allows for more degrees of freedom in reconfiguration and manipulation

of the microscale liquids. Employing these open microfluidic principles, two major platforms which enable a broad range of bioassays are developed in my PhD work: 1) a multi-liquid-phase open microfluidic system called the “Oil Immersed Lossless Total Analysis System (OIL-TAS) for performing efficient bioanalyte extraction and analysis (Chapters 2 and 3); and 2) a “microbial community fitness landscape” platform for performing functional assays on microbial communities (Chapter 6). Chapter 4 is an extension of the OIL-TAS technology from Chapters 2 and 3, describing a novel method for performing reagent delivery in microscale assay systems, and Chapter 5 describes an alternative sample extraction technology with similar physical principles as the OIL-TAS extraction technology, but does not require any custom devices or instrumentation. Although these developed platforms are designed to target different biological questions, at a high level the end goal is to provide simple and accessible tools to better explore and measure the complex parameter space in human diseases, towards realizing the objective of achieving ambient diagnostics.

Chapter 2

Enhancing DNA methylation analysis for rare analytes with an Oil Immersed Lossless Total Analysis System

Epigenetic modifications such as DNA methylation are involved in the regulation of gene expression and have been implicated in a variety of human diseases such as cancer. Although in recent years there have been dramatic improvements in the tools available for performing rare sample (e.g. single cell) genomic analyses, our ability to study epigenetics is comparatively lagging, due to inherent limitations in assay sensitivity for epigenetic analysis technologies. Traditional assays for measuring DNA methylation typically require a relatively large sample. The large sample required for these assays is necessary due to the long and complex procedures involved during the processing of epigenetically modified DNA, resulting in significant sample loss. Thus, technologies that reduce the time and complexity for rare sample processing have the potential to have broad impact across different epigenetic assays.

Here we report a modular and accessible open microfluidic platform that enables low-loss extraction of methylated DNA, to allow detection of DNA methylation events with single cell sensitivity. The platform is designed using two microfluidic methods: Exclusion-based Sample Preparation (ESP), which utilizes the dominance of surface tension over inertial forces at the microscale to create “virtual walls” between immiscible (oil) and aqueous phases to streamline the isolation of bioanalytes, and Exclusive Liquid Repellency (ELR), a recently discovered multi-liquid phase phenomenon for manipulation of microfluidic droplets that ensures favorable binding and lossless recovery of analytes. Surface

functionalized paramagnetic particles (PMPs) are used as a means for extraction of methylated DNA in the integrated ESP-ELR platform. The processing and extraction of methylated DNA from biosamples can be done with low loss and minimal external liquid handling (pipetting) in the platform and is compatible with traditional qPCR-based detection methods. Results show that our method allows for detection of methylated DNA events from prostate cancer cells down to single cell sensitivity, even in the presence of a large number of contaminating patient white blood cells, suggesting its potential to become a platform for processing and assaying cancer liquid biopsy samples.

2.1 Preface

This chapter summarizes our efforts in developing a “general purpose” sample processing platform aimed for assaying DNA methylation in rare samples. The developed platform, named the Oil Immersed Lossless Total Analysis System (OIL-TAS), enables a streamlined in situ sample processing workflow with multiple capabilities including magnetic bead-based analyte isolation, enzymatic reactions, heating/cooling operations, microscopic imaging, and lossless sample recovery, all on one device.

2.2 Introduction

The last 15 years have shown a dramatic increase in our understanding of the molecular drivers of solid tumors, ranging from genomic aberrations to immune evasion in the tumor microenvironment and others. And while the genomic revolution has identified important alterations that can drive cancer, it has become clear that only a minority of patients benefit from therapies that target these mutations. For example, mutations in DNA repair

pathway genes are present in less than 10% of patients with prostate cancer[1,2]. Thus, significant research efforts are now focused on understanding other molecular alterations in cancer that may drive aggressive disease and also serve as novel targets for drug development.

One emerging area of interest lies in the aberrant epigenetic landscape that has been identified across a broad range of malignancies. Epigenetics refers to a series of modifications that alter gene expression without changing the base pair sequence, with diverse proteins that modulate how epigenetic marks are placed (e.g., DNA methylation enzymes and histone methyltransferases), removed (e.g., DNA demethylation enzymes and histone deacetylases), or read (e.g., methyl CpG binding proteins) by transcriptional machinery (Figure 2.1)[3-5].

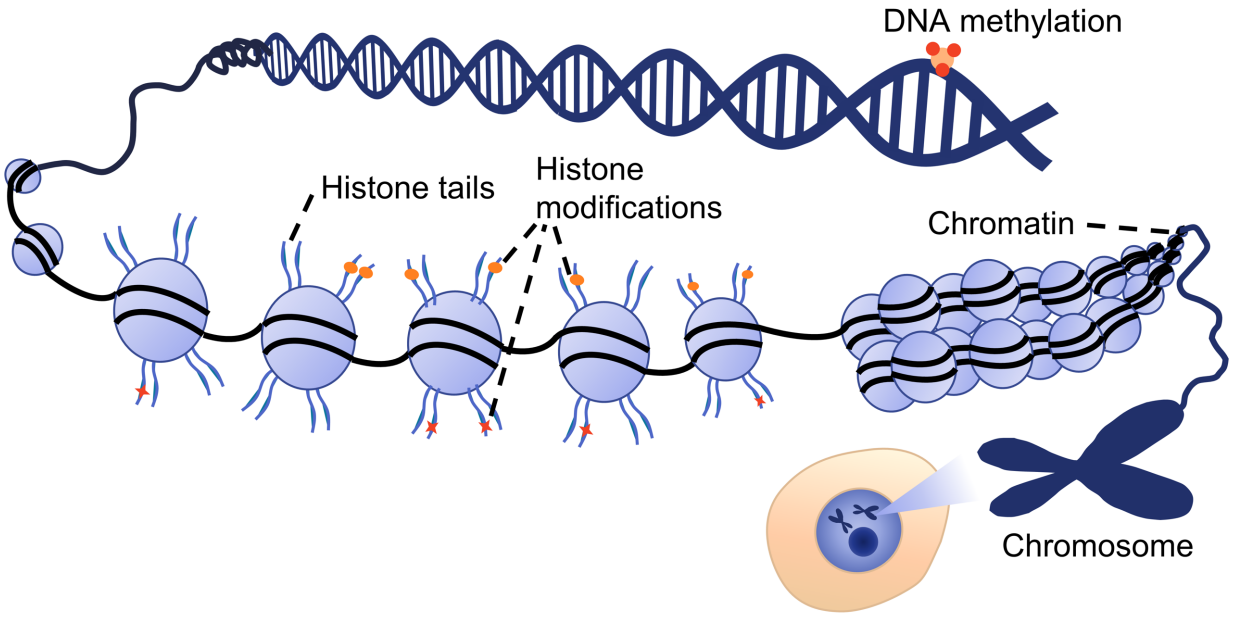

Figure 2.1: Epigenetic modifications include DNA methylation and histone tail modifications such as methylation, acetylation, etc.

The broad cancer epigenome has been shown to trend towards a global increase in DNA hypomethylation accompanied by an increase in CpG island hypermethylation in specific gene promoters[6-9]. This landscape results in large scale dysregulation of gene expression favoring expression of proto-oncogenes and silencing of tumor suppressor genes. There is growing interest to use epigenetic alterations as diagnostic and prognostic biomarkers for cancer given the high prevalence of these changes across a broad range of tumor types. However, there are currently no biomarkers available to identify those patients whose cancer is driven by these distinct epigenetic alterations. Thus, there is a critical need to develop technologies[10] that can extend the concepts of precision medicine beyond genomic aberrations to include epigenomic alterations that can drive aggressive cancers and treatment resistance. Epigenetic alterations are particularly common in prostate cancers, with some alterations such as hypermethylation of the GSTP1 promoter found in more than 90% of prostate cancer primary tumors, which suggest their potential as a diagnostic biomarker of the disease[11-13].

In recent years there has been increasing interest in developing less invasive cancer diagnostic tools such as liquid biopsies (blood tests). In particular, circulating tumor cells (CTCs) have shown great promise for use as a diagnostic and prognostic biomarker. However, the low abundance nature of CTCs has made the sample immensely challenging or incompatible with many genomic and epigenetic assays. Although we've seen dramatic improvements in the tools available for performing rare sample (e.g., single cell) genomic analyses such as PCR and sequencing, our ability to study epigenetics lags considerably, due to inherent limitations in assay sensitivity. Traditional assays for measuring epigenetic alterations in DNA require a large number of input cells, thus

preventing interrogation of many rare clinical sample types (e.g., CTCs and circulating tumor DNA (ctDNA)). For example, bisulfite sequencing involves the bisulfite conversion of cytosine nucleotides to uracil whereas 5-methylcytosine cytosines remain intact, the changes of which are then identified with Sanger sequencing. The destructive nature of the bisulfite conversion procedure often leads to a loss of as much as 90% of the starting DNA sample[14], impacting assay sensitivity. As such, these assays commonly require a large number of input cells due to their long or harsh procedures resulting in significant sample loss. More recently, alternative DNA methylation assays such as those employing methyl-DNA binding (MBD) proteins (e.g. MBD2) allow for isolation of epigenetically-modified DNA under milder conditions[15], better preserving the integrity of the DNA and improving sensitivity. Importantly, many of these newer epigenetic assays are heavily dependent on the ability to efficiently manipulate intact DNA-protein complexes (i.e., capture, isolation, and elution) without significant loss. Thus, technologies that directly improve this functionality have the potential to have broad impact across multiple different epigenetic analysis techniques.

To these ends, we have developed a modular and accessible microfluidic platform that enables low-loss extraction of methylated DNA, to allow for detection of DNA methylation events with single cell sensitivity. The platform which we named the “Oil-Immersed Lossless Total Analysis System (OIL-TAS)” (coined after the “Micro Total Analysis System (μTAS) concept first proposed by Manz et al. in 1990)[16] employs two microfluidic methods developed in our lab: Exclusion-based Sample Preparation (ESP)[17-22], which utilizes the dominance of surface tension over inertial forces at the microscale to create “virtual walls” between immiscible (oil) and aqueous phases to streamline analyte

isolation, and Exclusive Liquid Repellency (ELR)[23-25], a recently discovered multi-liquid phase phenomenon for manipulation of microfluidic droplets that ensures favorable binding conditions and lossless recovery of analytes. Surface functionalized magnetic beads are used as a means to perform extraction of methylated DNA analytes in the OIL-TAS. The processing and extraction of methylated DNA from rare samples can be achieved with low loss and minimal external liquid handling (pipetting) in the OIL-TAS platform and is compatible with traditional off-chip molecular detection methods.

2.3 Results and Discussion

We have extensively tested and optimized various aspects of the microfluidic devices and assay design to enable detection of methylation events down to single cell sensitivity. These optimizations include significant geometrical changes to the device design, device fabrication methods, and assay process optimizations including magnetic bead type, bead amount, binding time, cell lysis methods, sequence of steps in the assay, among others. The results of these optimizations are summarized below.

2.3.1 Device development

We've developed 2 different ESP and ELR-based extraction platforms for enrichment of methylated DNA from rare samples. In the 1st generation platform (Figure 2.2A), we patterned an array of hydrophilic spots on an ELR substrate via selective oxygen plasma etching to form individual droplets that are anchored to the bottom substrate and isolated from each other via an oil overlay[24]. This design allows microscale droplets to be patterned with high throughput and doesn't require physical solid barriers to keep the

droplets apart. We discovered that this technique works well when operated with care but is more prone to accidental sample cross contamination resulting from operator error in pipetting or external force (like a vigorous “bump” or “jolt” of the device, which can dislodge the patterned droplets). The hydrophilicity of the patterned spots also results in sample loss due to residual volume from the anchored droplets being left on the device surface (albeit minor).

To overcome these challenges and also increase the robustness of the platform, we’ve thus performed a number of significant design changes. We found that a solution to the above-described problems is to employ a “walled” design comprising of an array of droplet wells interconnected by oil extraction channels on top of a fully ELR (non-patterned) surface. All the surfaces of the device (including the wells, channels, and bottom substrate are ELR treated to make them liquid repellent, and hence, any given droplet in the platform is fully recoverable without loss, whereas the previous technique employing surface patterning has more sample loss (Figure 2.2). We named this new device design the “Oil Immersed Lossless Total Analysis System (OIL-TAS) (Figure 2.2B). The addition of physical “walls” (wells) also greatly mitigates concerns with operator error as it provides a visible cue for pipette tip insertion and also the physical confinement prevents droplets from becoming dislodged with external force. We found that droplets within the new OIL-TAS device are highly stable with no observed droplet escape or dislodging even when vigorously shaken on an orbital shaker at 1200 RPM for 1 hour. We’ve also characterized the performance of the OIL-TAS platform and found the carryover volume after ESP extraction to be improved from 0.35% in the original 1st generation platform to a mere 0.17% in the 2nd generation platform. This revised OIL-TAS platform also uses a unibody

construction polycarbonate (PC) material which is thermally stable up to 135°C (the 1st generation platform has a polystyrene-glass hybrid construction which is not heat resistant). This enables a wide temperature operating window for reagent freezer storage (-20 ºC), assay incubation (37 ºC) and heat elution (65~98 ºC) directly on the device, further simplifying the operation process. The optically clear thin device bottom (127 µm) design allows for efficient magnetic manipulation, rapid heat transfer, and optical access, which also makes the device compatible with visual, absorbance, fluorescence, luminescence, and microscopy-based readouts.

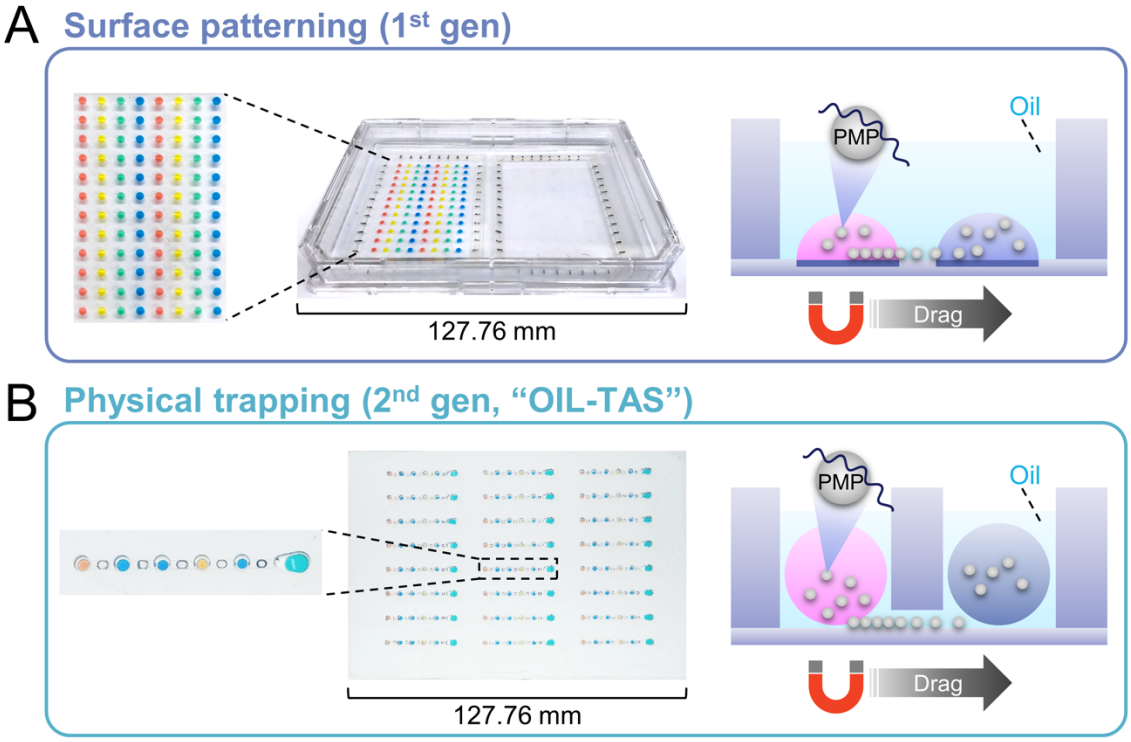

Figure 2.2: Development of under oil ESP/ELR devices for methylated DNA extraction. (A) 1st generation device for methylated DNA extraction. An ELR substrate is surface patterned via oxygen plasma to create hydrophilic spots which anchor aqueous droplets. (B) 2nd generation "OIL-TAS" device which employs physical walls (wells) to trap individual droplets. The 2nd generation OIL-TAS device enables fully lossless droplet recovery, more robust liquid handling, greater flexibility in droplet volumes, and a larger operating temperature range.

During the optimization of the 2nd generation OIL-TAS device design, we found that aqueous solutions containing detergents/surfactants (Tween-20) can reduce the surface tension of the droplets and occasionally result in the aqueous droplet "creeping" into the oil-filled extraction channels after extended periods of shaking or vigorous pipetting. We discovered that adding a well in the ceiling of the extraction channel traps an air bubble inside the channel, preventing the aqueous droplet from creeping into the channel (Figure 2.3). The mechanism behind this phenomenon is likely due to the Laplace pressure of the air bubble, which prevents the flow of the oil during vigorous device operations.

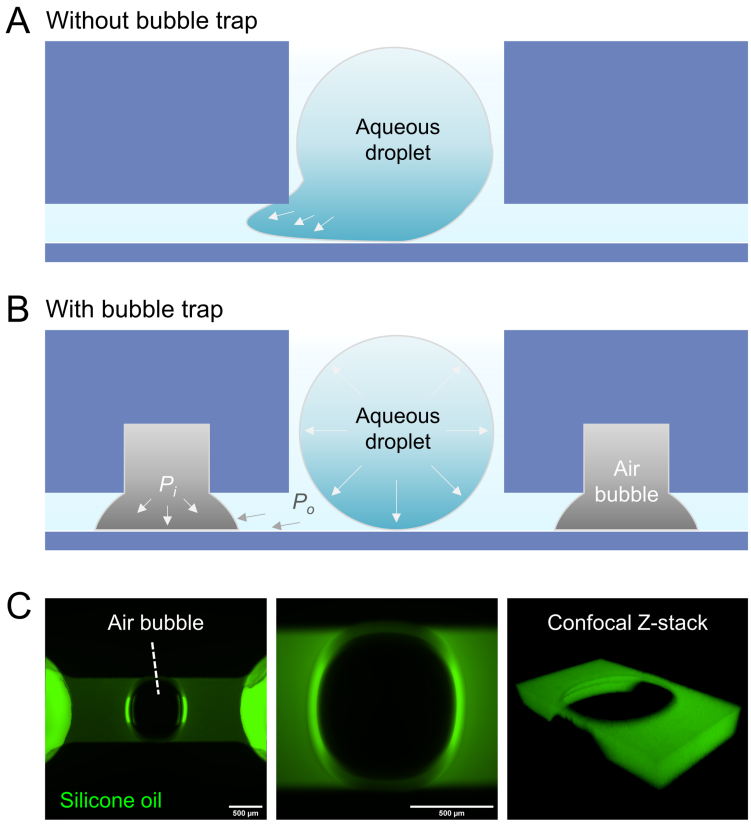

Figure 2.3: An "air bubble trap" design within the extraction channels of the OIL-TAS device to prevent aqueous droplets from "creeping" into the channels during shaking or vigorous pipetting. (A) Schematic of aqueous droplet "creeping" without air bubble trap design. (B) Air bubble traps within the extraction channels prevent the aqueous droplet from creeping into the channels. (C) Fluorescence microscopy images of the air bubble within the extraction channel. The silicone oil is stained fluorescent green with an oil-soluble fluorescent dye (Nile Red). Scale bars: 500 μm.

2.3.2 Assay process optimization

We further optimized the methylated DNA assay process using the 2nd generation (OIL-TAS) device. Using positive control hypermethylated DNA from HCT116 cells, we tested various assay parameters to achieve the highest sensitivity (lowest Ct value as determined using qPCR). These include bead binding time (Figure 2.4A), bead amount (Figure 2.4B), as well as magnetic bead type (TALON beads from Takara vs. His-tag Dynabeads from Thermo Fisher).

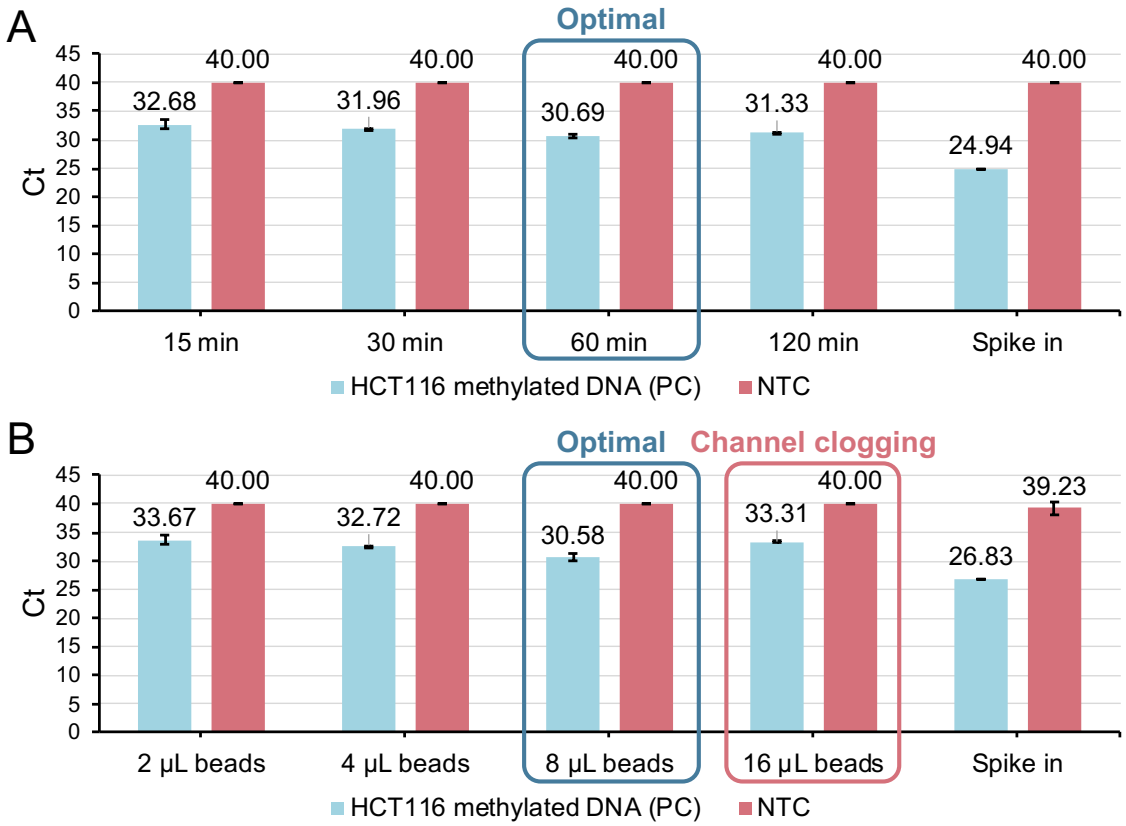

Figure 2.4: Optimization of bead binding parameters for methylated DNA extraction. (A) Optimization of MBD2 bead binding time for capture of methylated DNA. A positive control (PC) hypermethylated DNA from HCT116 cells was used for evaluating capture performance. NTC: No template control. (B) Optimization of MBD2 bead amount for capture of methylated DNA. qPCR gene target: LINE1. Spike in: input sample without restriction enzyme digestion and bead capture/enrichment. Error bars denote the standard deviation from 2 technical replicates.

We found that a combination of 60 min bead binding (with shaking), and 8 µL of beads yielded the highest sensitivity. We've also found that His-tag Dynabeads yielded better extraction performance (better magnetic responsiveness) and mixing performance (they settle slower) than TALON beads. These initial experiments were performed using purified DNA as an input sample to reduce the number of variables during assay optimization. However, clinical CTC samples come as a cell suspension. We thus developed and tested different methods to enable intact cells to be used as an input sample on the platform. Two main methods were investigated: 1) integrating an additional DNA extraction step onto the same device using silica bead/guanidine salt chemistry, and 2) direct cell lysis (without DNA extraction) using an enzyme-based approach (Qiagen protease) (Figure 2.5). In the first method (DNA extraction), a 1 µL cell suspension is pipetted into each input well of the OIL-TAS device under oil forming a droplet. The 1 µL droplets are then imaged under a conventional epifluorescence microscope to quantify the number of cells within each droplet. After imaging, a chemical lysis buffer (Qiagen Buffer RLT plus)/magnetic silica bead (Promega MagneSil) mixture is added to the cell droplet, lysing the cells and binding the released DNA onto the magnetic silica beads. The beads are then magnetically extracted (via ESP) through the oil channels in the device, through wash buffers, and into the next assay solution. In the second method (direct cell lysis), cells are deposited and imaged in the same way, followed by the addition of an enzyme (Qiagen protease) to perform cell lysis. Following lysis and digestion, the protease is inactivated by heating at 70 ºC. In this method, no total DNA extraction is performed. After testing both methods, we found that the DNA extraction method yielded higher sensitivity than direct cell lysis for methylated DNA extraction (Figure 2.6).

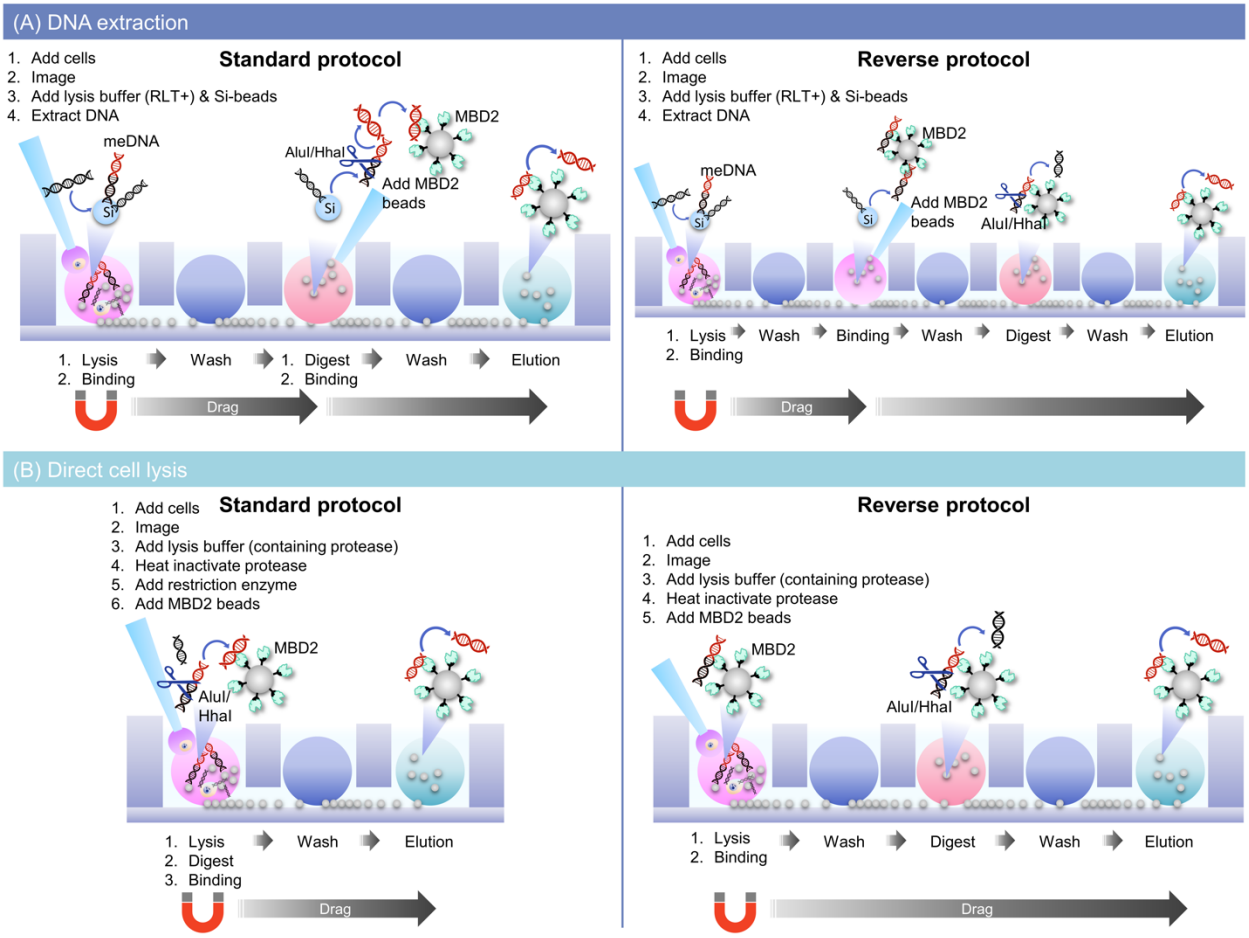

Figure 2.5: Comparison of OIL-TAS assay format for methylated DNA extraction. This involves (A) DNA extraction from cells or (B) direct cell lysis. We've also compared running the assay using a standard protocol (DNA enzyme digest followed by methylated DNA capture, left panel), vs. a reverse protocol (methylated DNA capture followed by digest, right panel).

We further investigated alternating the sequence of DNA digest and methylated DNA capture, i.e., performing DNA digest followed by methylated DNA capture (standard protocol) vs. performing capture first followed by digest (reverse protocol) (Figure 2.5). Results show that the standard protocol yielded higher sensitivity across all sample concentrations (Figure 2.7).

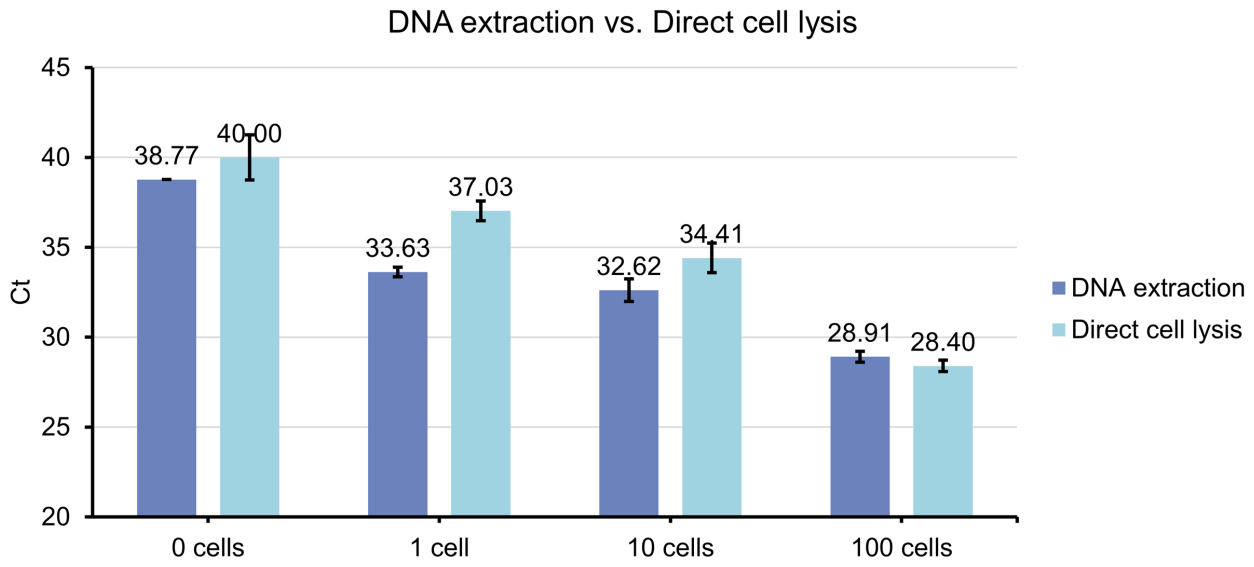

Figure 2.6: Comparison of assay sensitivity using a DNA extraction protocol vs. a direct cell lysis protocol. LNCaP cells were used as the sample. qPCR gene target: LINE1. Error bars denote the standard deviation from 3 technical replicates.

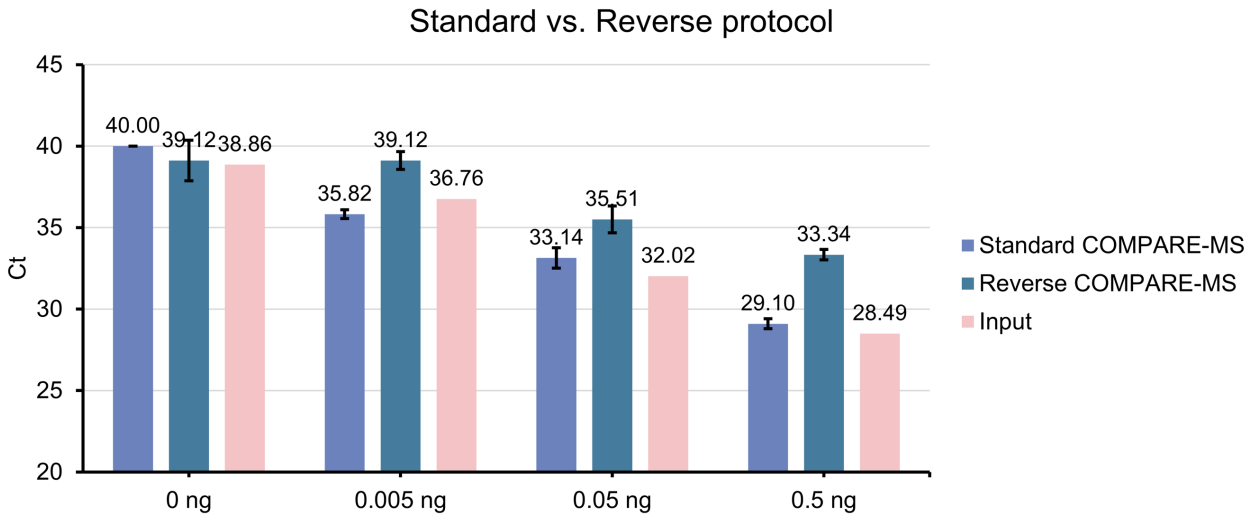

Figure 2.7: Comparison of assay sensitivity using a standard protocol (DNA digest followed by methylated DNA capture) vs. a reverse protocol (methylated DNA capture followed by digest). HCT116 hypermethylated DNA was used as the sample. Input: DNA that was directly added to the qPCR reaction without undergoing methylated DNA digest and extraction. qPCR gene target: LINE1. Error bars denote the standard deviation from 2 technical replicates.

2.3.3 Detection of DNA methylation events from prostate cancer cells and contrived CTC samples with low cell numbers

The final optimized form of the assay starts from dispensing droplets containing a cell suspension into the device, fluorescence microscopy imaging of the droplets, cell lysis and total DNA capture using a guanidine salt/silica bead chemistry, ESP-based magnetic bead washing, restriction enzyme digest, methylated DNA capture using MBD2-functionalized magnetic beads, another ESP-based wash, and heat elution (Figure 2.8).

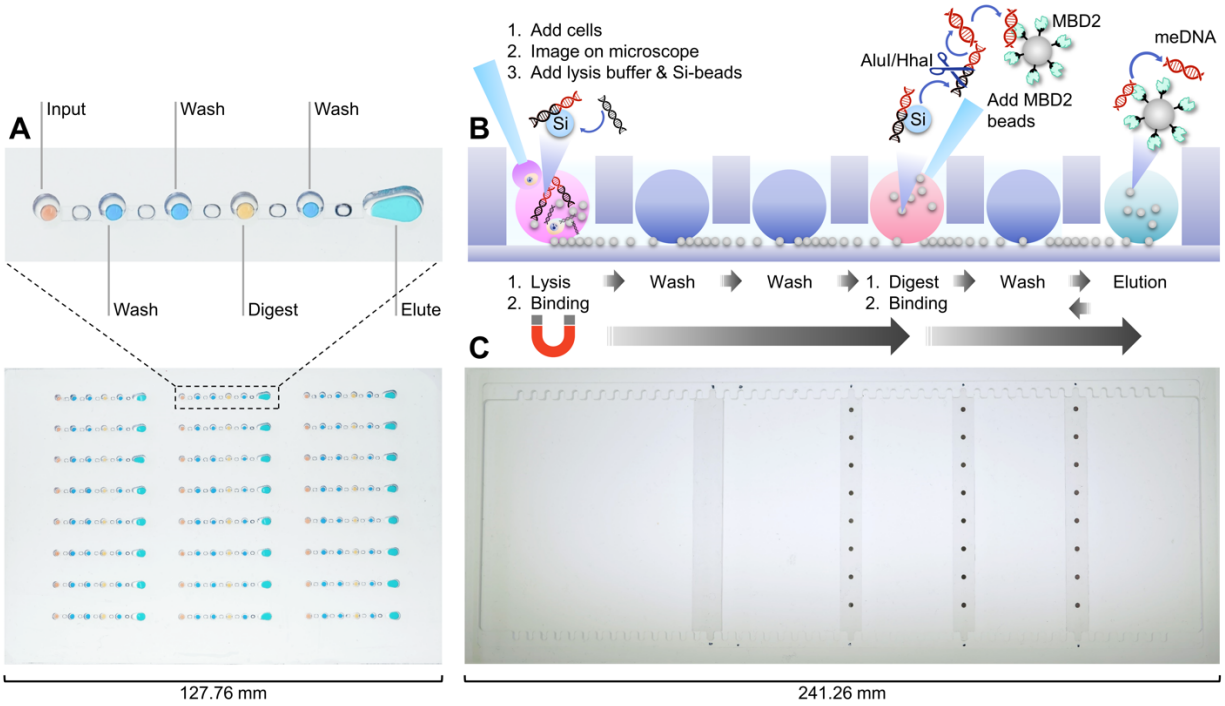

Figure 2.8: Final optimized form of the OIL-TAS assay for performing methylated DNA extraction and enrichment from rare samples. (A) Whole device and closeup image of the OIL-TAS device consisting of an array of wells interconnected by oil-filled extraction channels. The wells are filled with droplets containing food coloring to aid in visualization. (B) Sideview operation schematic for performing methylated DNA extraction and enrichment in the OIL-TAS device. (C) Image of the modular magnetic extractor for performing magnetic bead extraction in the OIL-TAS device.

After optimizing the assay performance on the OIL-TAS platform, we used GSTP1 methylation in prostate cell lines as a model system. We are able to detect GSTP1

methylation in LNCaP prostate cancer cells down to single cells, with little GSTP1 methylation signal from RWPE1 (a normal prostate cell which is commonly non-methylated for GSTP1) (Figure 2.9), demonstrating the platform's ability to accurately assay gene methylation events at very low cell input numbers.

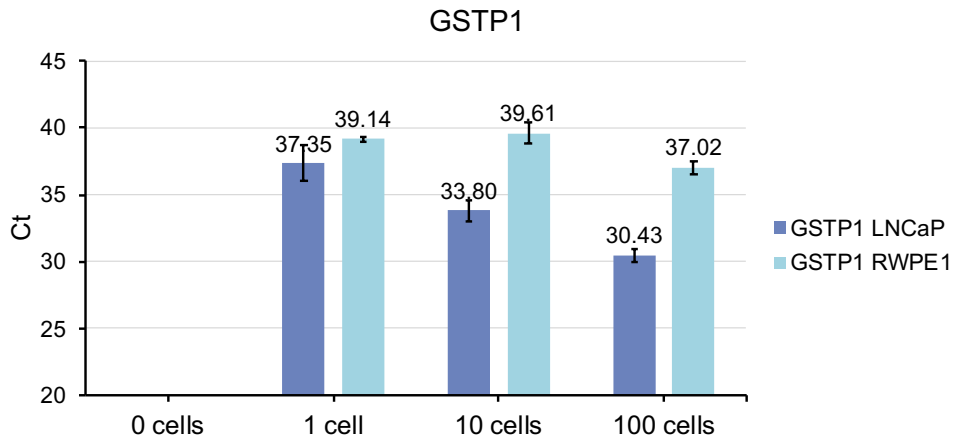

Figure 2.9: Differential methylation levels of GSTP1 in LNCaP cells (a prostate cancer cell) and RWPE1 cells (a normal prostate cell) assayed using OIL-TAS. qPCR gene target: GSTP1. Results show a higher level of methylation (lower Ct) for the GSTP1 gene in LNCaP cells compared to RWPE1 cells. Error bars denote the standard deviation from 3 technical replicates.

Although we've obtained great results with pure prostate cancer cell lines, true clinical CTC samples are more difficult to process. A major issue in clinical CTC samples is the presence of a high number of contaminating white blood cells (WBCs) in addition to the tumor cells in the samples. This poses a major challenge to any assay targeting CTCs as a sample analyte owing to the inherent high background "noise" contributed from the WBCs. Thus, to assess how the OIL-TAS assay would perform in such a scenario, we spiked 0, 1, 10, and 100 LNCaP cells into 2 healthy donor WBCs at a tumor cell to WBC ratio of 0:1, 1:1, 1:10, 1:100 to model patient CTC samples. Results show that the assay was able to pick up methylation events for the GSTP1 gene down to single cells even in

the presence of a high background of contaminating WBCs (Figure 2.10), demonstrating the robustness of the assay and its potential to be used on true clinical CTC samples.

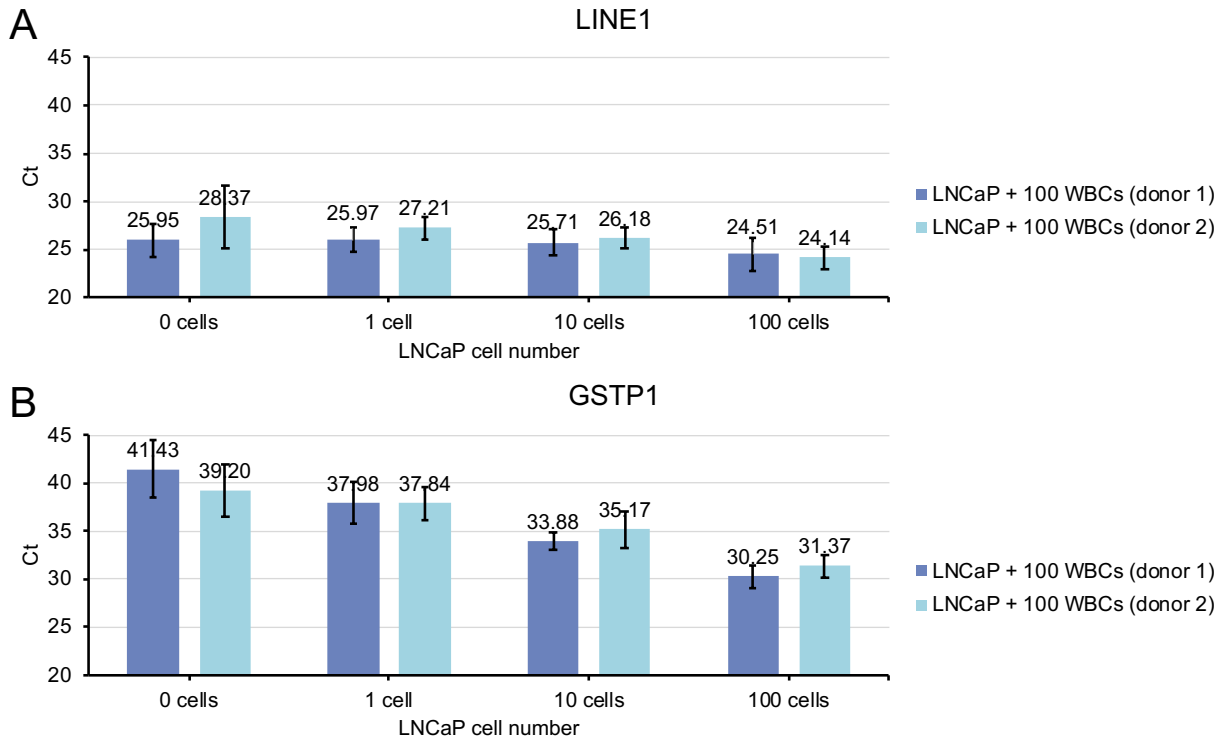

Figure 2.10: Detection of DNA methylation in LNCaP cells spiked into 2 healthy donor WBCs at a ratio of 0:100, 1:100, 10:100, and 100:100 to model a clinical CTC sample. (A) Detection of gene targets LINE1 and (B) GSTP1 using the OIL-TAS assay followed by qPCR. Error bars denote the standard deviation from 9 technical replicates.

2.4 Materials and Methods

2.4.1 Fabrication of 1st generation ESP device

A 43 mm x 60 mm area was cut out of the bottom of an OmniTray single-well plate (Thermo Scientific Nunc) using a computer numerical control (CNC) 3-axis mill (Tormach, PCNC 770). Medical grade double-sided tape (Adhesives Research, ARCare 90106) was cut using a laser engraver (Automation Technology, 350-60W CO_2 Laser). After removal of the protective backing on the double-sided tape, a 48 mm x 65 mm x 0.17 mm coverslip

(Gold Seal Cover Glass) was aligned and adhered to the double-sided tape. The coverslip with the attached tape was then aligned and adhered to the bottom of the OmniTray cutout. To further prevent oil leakage, the outer edges along the coverslip was sealed using Duro Super Glue. The coverslip-bottom OmniTray was then treated with oxygen plasma for 2 min at 100 W (Diener Electronic Femto, Plasma Surface Technology). After plasma treatment, the OmniTray was placed in a vacuum desiccator with 2 trays (20 µL each) of PDMS silane (1,3'dichlorotetramethylsiloxane, Gelest, SID3372.0). The desiccator was then pumped down to vaporize and condense the PDMS silane onto the device surface at RT for 1 hour to functionalize the device surface. The OmniTray was then thoroughly rinsed with 100% isopropyl alcohol then dried using an air gun. To pattern the hydrophilic regions on the ELR surface, a PDMS mask with 2 mm circular cutouts (fabricated using a laser engraver (Automation Technology, 350-60W CO_2 Laser)) was attached to the surface of the coverslip via physical adsorption, then oxygen plasma treated for 2 min at 100 W (Diener Electronic Femto, Plasma Surface Technology). The plasma treatment etches away the PDMS-silane on the exposed regions of the PDMS mask, rendering them hydrophilic, whereas protected areas retain their ELR hydrophobic property. Lastly, the PDMS mask was removed, and the device was UV treated for 10 min to prevent contamination.

2.4.2 Fabrication of 2nd generation (OIL-TAS) device

OIL-TAS devices were machined out of 4.5 mm thick polycarbonate sheets (LEXAN 9034, United States Plastic Corporation) using a computer numerical control (CNC) mill (Tormach, PCNC 770). After machining, the devices were cleaned with 100% isopropyl

alcohol and dried with an air gun. The OIL-TAS device was then bonded to a 0.005 inch (127 μm) thick polycarbonate sheet (TAP Plastics) using a thermal press (Carver Press, 3889.1NE1001) with a pressure of 2500 Kg for 30 min to form the assembled device. The assembled OIL-TAS device was then treated with oxygen plasma for 2 min at 100 W (Diener Electronic Femto, Plasma Surface Technology). After plasma treatment, the device was placed in a vacuum desiccator with 2 trays (40 μL each) of PDMS silane (1,3'dichlorotetramethylsiloxane, Gelest, SID3372.0). The desiccator was then pumped down to vaporize and deposit the PDMS silane onto the device surface at room temperature overnight to functionalize the device surface. After silane treatment, the device was thoroughly rinsed with 100% isopropyl alcohol to remove residual unattached PDMS silane then dried using an air gun.

2.4.3 Fabrication of magnetic manipulator

A 5.8 mm thick Polymethylmethacrylate (PMMA) sheet was CNC machined to fabricate the magnetic manipulator for performing magnetic bead extractions. The magnetic extractor base consists of 2 rows of “teeth” on the top and bottom edge, each “tooth” has a horizontal pitch of 4.5 mm and fits a 3 mm thick vertical magnet array insert (also CNC machined). Each magnet array insert is fitted with 8 rare-earth circular magnets (diameter 1/16 inch (~1.6 mm), thickness 1/8 inch (~3.2 mm) (K&J Magnetics), with a vertical pitch of 9 mm corresponding to the vertical well pitch in the OIL-TAS device.

Integrated cell imaging, total DNA extraction, DNA digestion, and methylated DNA extraction on the OIL-TAS device

We assayed prostate cell lines with known methylated (meDNA) or non-methylated (non-meDNA) regions (LNCaP and RWPE1). 1 µL droplets of SuperBlock Blocking Buffer (Thermo) containing 0, 1, 10, and 100 cells stained with a fluorescent tracking dye (Calcein AM) was added into the OIL-TAS device under oil, then imaged on an inverted epifluorescence microscope (Nikon Ti Eclipse) to quantify cell numbers within each droplet. Following imaging, a lysis/binding buffer (Buffer RLT plus, Qiagen) mixed with magnetic silica beads (MagneSil beads, Promega) was added to the cell droplets to lyse the cells and bind the released DNA onto the silica beads. The magnetic silica beads were then magnetically transported through 2 wash buffers and into a droplet containing two restriction enzymes: AluI, to fragment DNA, and HhaI, to further digest DNA only at unmethylated CGCG restriction sites, preserving the methylated DNA (meDNA) fragments. Separately, Dynabeads His-Tag (Thermo) magnetic beads were coupled with the methyl-CpG binding domain of methyl-CpG binding domain protein 2 (MBD2-MBD) via His-tag chemistry. The MBD2- conjugated magnetic beads were added to the digested DNA to allow the MBD2 protein to bind to methylated regions of DNA within the digested total DNA fragments. The bound fraction was transferred magnetically through the oil and a droplet of wash buffer then into an elution solution. The device was then heated to 65 ºC for 15 min to elute the meDNA from the MBD2 protein beads. Beads were removed from the eluted DNA by magnetically extracting the beads in the opposite direction on the device. The droplet containing enriched meDNA was then pipetted into a prepared PCR plate containing PCR master mix and primers targeting LINE1 (as an internal methylation control) and GSTP1 (a gene that is commonly methylated in prostate cancer cells).

2.5 Conclusions

To summarize, we've developed a simple, modular, flexible, and open "total analysis system" called OIL-TAS to enable the streamlined processing and analysis of rare samples. We've successfully integrated the multiple complex processes for methylated DNA extraction into a single device, starting from cell isolation, cell imaging, DNA extraction, DNA digestion, methylated DNA enrichment, and elution. The developed OIL-TAS assay showed good assay sensitivity, achieving single-cell level sensitivity for DNA methylation analysis, even in the presence of background contaminating non-target white blood cells.

The technological advances described in this chapter will, in the short term, enable us to assay the underlying epigenetic landscape in rare clinical specimens such as CTCs with relative ease, which has previously been difficult to do. We anticipate that by expanding on our ability to assay rare samples, it gives us the unique opportunity to discover novel epigenetic biomarkers in cancer which point to future diagnostic, prognostic, or therapeutic targets. The operational simplicity of the developed assay also provides the potential to adapt the assay for use in clinical diagnostics with already known epigenetic biomarkers of cancer (such as GSTP1). Currently no epigenetic assay yet exists for use in clinical cancer diagnostics.

After demonstrating the performance of the developed assay using prostate cancer cell lines and contrived patient samples, we plan to use the assay to test CTC samples from prostate cancer patients. However, due to the COVID-19 pandemic, acquiring patient CTC samples for experiments has been difficult. We plan to start testing prostate cancer CTC samples on the developed platform in the near future.

To summarize, the OIL-TAS platform enables the following functionalities:

Ability to process rare samples with minimal loss:

- The ELR system enables lossless liquid handling (full sample recovery).
- The oil overlay minimizes evaporation and contamination in microscale droplets.

Ability to perform heating and cooling:

- Polycarbonate (PC) unibody construction enables heating (up to 115 ºC) and cooling (down to -40 ºC).
- Enables enzyme reactions at elevated temperatures, heat inactivation, DNA elution, among other temperature-sensitive processes to be performed in situ.

Ability to perform optical readouts:

- Device bottom is an optically clear, thin (127 µm) PC sheet.
- Enables high magnification (short working distance) microscopy, as well as fluorescence, absorbance, and luminescence readouts via a plate reader.

Ability to perform magnetic manipulation:

- The thin device bottom enables efficient magnetic manipulation of magnetic beads for performing solid-phase analyte extraction.

Compatible with standard instrumentation:

- The OIL-TAS device was designed to have the same outer dimensions and well pitch as a conventional multi-well plate, enabling liquid handling via multi-channel pipets and data acquisition with commercial optical plate readers.

2.6 Acknowledgements

This study was funded by the National Institutes of Health (NIH 1R01CA247479, NIH P30CA014520) and a UW Institute for Clinical and Translational Research pilot grant (NIH UL1TR002373).

Chapter 3

Oil Immersed Lossless Total Analysis System for Integrated RNA Extraction and Detection of SARS-CoV-2[1]

The COVID-19 pandemic exposed difficulties in scaling current quantitative PCR (qPCR)-based diagnostic methodologies for large-scale infectious disease testing. Bottlenecks include lengthy multi-step processes for nucleic acid extraction followed by qPCR readouts, which require costly instrumentation and infrastructure, as well as reagent and plastic consumable shortages stemming from supply chain constraints. Here we report an Oil Immersed Lossless Total Analysis System (OIL-TAS), which integrates RNA extraction and detection onto a single device that is simple, rapid, cost effective, and requires minimal supplies and infrastructure to perform. We validated the performance of OIL-TAS using contrived SARS-CoV-2 viral particle samples and clinical nasopharyngeal swab samples. OIL-TAS showed a 93% positive predictive agreement (n=57) and 100% negative predictive agreement (n=10) with clinical SARS-CoV-2 qPCR assays in testing clinical samples, highlighting its potential to be a faster, cheaper, and easier-to-deploy alternative for infectious disease testing.

---

[1]This chapter has been modified from a published manuscript (*Nat. Comm.* 2021, 12, 4317). The manuscript includes as authors Duane S. Juang, Terry D. Juang, Dawn M. Dudley, Christina M. Newman, Molly A. Accola, William M. Rehrauer, Thomas C. Friedrich, David H. O'Connor, and David J. Beebe.

3.1 Preface

Although the OIL-TAS platform was initially developed for epigenetic assays (as described in Chapter 2), the modularity and generalizability of its core design and functional capabilities (lossless liquid handling, magnetic sample extraction, optical accessibility, wide working temperature range, flexible working volumes, minimized evaporation and contamination) allow OIL-TAS to be used as a "general purpose" assay platform capable of a broad range of bioassays, not just an application-specific platform. This chapter summarizes such an application: employing a variant of the OIL-TAS platform to perform integrated RNA extraction and detection of SARS-CoV-2, which was developed during the height of the COVID-19 pandemic in year 2020.

3.2 Introduction

Broad testing is crucial for monitoring and controlling the spread of infectious disease outbreaks. The coronavirus disease 2019 (COVID-19) pandemic caused by severe acute respiratory syndrome coronavirus 2 (SARS-CoV-2) spread rapidly around the world after its initial outbreak from Wuhan China in December 2019[26,27], quickly overwhelming current diagnostic testing capacity and supply chains. The go-to gold standard diagnostic technique for novel infectious diseases is usually molecular-based (i.e. quantitative polymerase chain reaction (qPCR)), owing to the relative ease to develop a highly sensitive and specific test within a short timeframe. However, existing methodologies for molecular testing have proven difficult to scale, owing to the assay's complexity, lengthy

operation, requirement of dedicated centralized testing infrastructure, and supply chain constraints.

The current standard method for SARS-CoV-2 nucleic acid testing is a multi-step protocol involving RNA extraction from patient samples (most commonly nasal, nasopharyngeal or oropharyngeal swabs, and saliva) using magnetic bead-based or column-based methods, followed by reverse transcription quantitative PCR (RT-qPCR) based detection of the extracted RNA. The RNA extraction process typically involves: 1) mixing the sample with lysis/binding buffer, 2) solid-phase capture of the viral RNA via magnetic beads or columns, 3) multiple washes involving magnetic separation or centrifugation for each wash, 4) elution of viral RNA with water or a low salt buffer, 5) adding the eluted RNA to a PCR plate containing RT-qPCR master mix and primers, followed by thermocycling and data capture in a qPCR machine. This process often takes up to 4 hours and is challenging to scale because of the complexity of the RNA extraction process, coupled with the RT-qPCR process itself which requires over 1 hour of on-machine real-time fluorescence measurements, significantly limiting assay turnaround time. The nature of this complex multi-step process also necessitates the use of a significant amount of plastic consumables (pipet tips, tubes, plates, columns, etc.) which become biohazardous waste after the assay. For example, it is estimated that up to 10 pipet tips (6 for RNA extraction, 4 for PCR setup) are consumed per sample for a SARS-CoV-2 qPCR-based molecular test[28]. This has also led to widespread shortages of essential plastic consumables to perform the tests, significantly bottlenecking testing capacity[29].

To address these challenges for scaling up testing, here we report an alternative molecular assay we termed the Oil Immersed Lossless Total Analysis System (OIL-TAS) which integrates RNA extraction and detection into a single device with the footprint of a generic 96-well plate. The OIL-TAS is an integration of three main technologies: 1) an underoil droplet microfluidic technology called Exclusive Liquid Repellency (ELR) that allows for lossless sample processing[23-25]; 2) a rapid solid-phase analyte extraction method called Exclusion-based Sample Preparation (ESP)[17,19-22]; and 3) isothermal amplification with colorimetric readout (Loop-Mediated Isothermal Amplification, LAMP[30,31]). The OIL-TAS has advantages over traditional RT-qPCR assays including simplicity, lossless sample handling, less reagent/plastic consumable consumption, lower cost, and increased speed and throughput. Importantly, the OIL-TAS can be operated using pipettes, a shaker, an oven, and an image capture device, which are widely available in biomedical laboratories without the need for costly or specialized instruments. We also deliberately engineered the assay to be compatible with open source, non-proprietary reagents and employ a colorimetric isothermal detection method to reduce assay time and avoid adding burden to current qPCR testing supply chains and clinical workflows. We demonstrate that the OIL-TAS can reliably detect a concentration of 10 copies/μL and sporadically detect down to 1 copy/μL with contrived SARS-CoV-2 viral particle samples. When testing clinical nasopharyngeal swab samples, OIL-TAS showed a 93% positive predictive agreement (n=57) and 100% negative predictive agreement (n=10) with clinical SARS-CoV-2 qPCR assays.

3.3 Results and Discussion

3.3.1 Operation principle and design of the OIL-TAS

The OIL-TAS builds upon our previously reported ELR technology, which describes physical conditions where an aqueous droplet can be fully repelled from a solid surface (contact angle = 180°) in the presence of an oil phase when a specific set of oil and solid interfacial energy properties are met. The conditions in which ELR will occur are when the sum of the interfacial energies of the solid/oil and aqueous/oil interface are equal to, or less than the solid/aqueous interfacial energy. Through experimentation, we found that this condition can be accomplished by employing a Polydimethylsiloxane (PDMS)-silane functionalized surface paired with silicone oil as the oil phase[25]. The most significant advantage of ELR is that it prevents adsorption of biological samples to surfaces and thus has very little, if any, associated sample loss. With ELR, one can create individually isolated aqueous droplets immersed under a common oil phase, each droplet providing a completely isolated reaction condition with no crosstalk with the solid surface of the reservoir, enabling liquid handling without loss.

Although ELR can effectively mitigate surface adsorption-mediated sample loss, another common source of loss during sample processing often occurs during solid-phase extraction processes: namely, target analytes (such as RNA) that are bound to a solid phase (magnetic beads or column resin) can fall off prematurely during the multiple washing steps that are common in solid-phase extraction processes such as RNA extraction. This issue can be effectively reduced by employing Exclusion-based Sample Preparation (ESP), which refers to a collection of solid-phase analyte extraction

techniques by which analytes bound to a solid-phase (magnetic beads) can be extracted out of a complex sample by transporting the beads via a magnet through an immiscible interface (oil or air) to “exclude” non-target contaminants from the sample. The ESP process replaces the multiple washing operations in traditional solid-phase extraction techniques with a simple magnetic dragging operation through the immiscible interfaces, resulting in a much shorter processing time and higher sample recovery[17,19-22,32-34].

OIL-TAS combines the ELR and ESP technologies into a rapid and flexible integrated analyte extraction and detection platform. The OIL-TAS consists of an array of immobilized ELR droplets immersed under an oil bath, where each droplet can contain a sample, wash solution, or reaction solution (Figure 3.1).

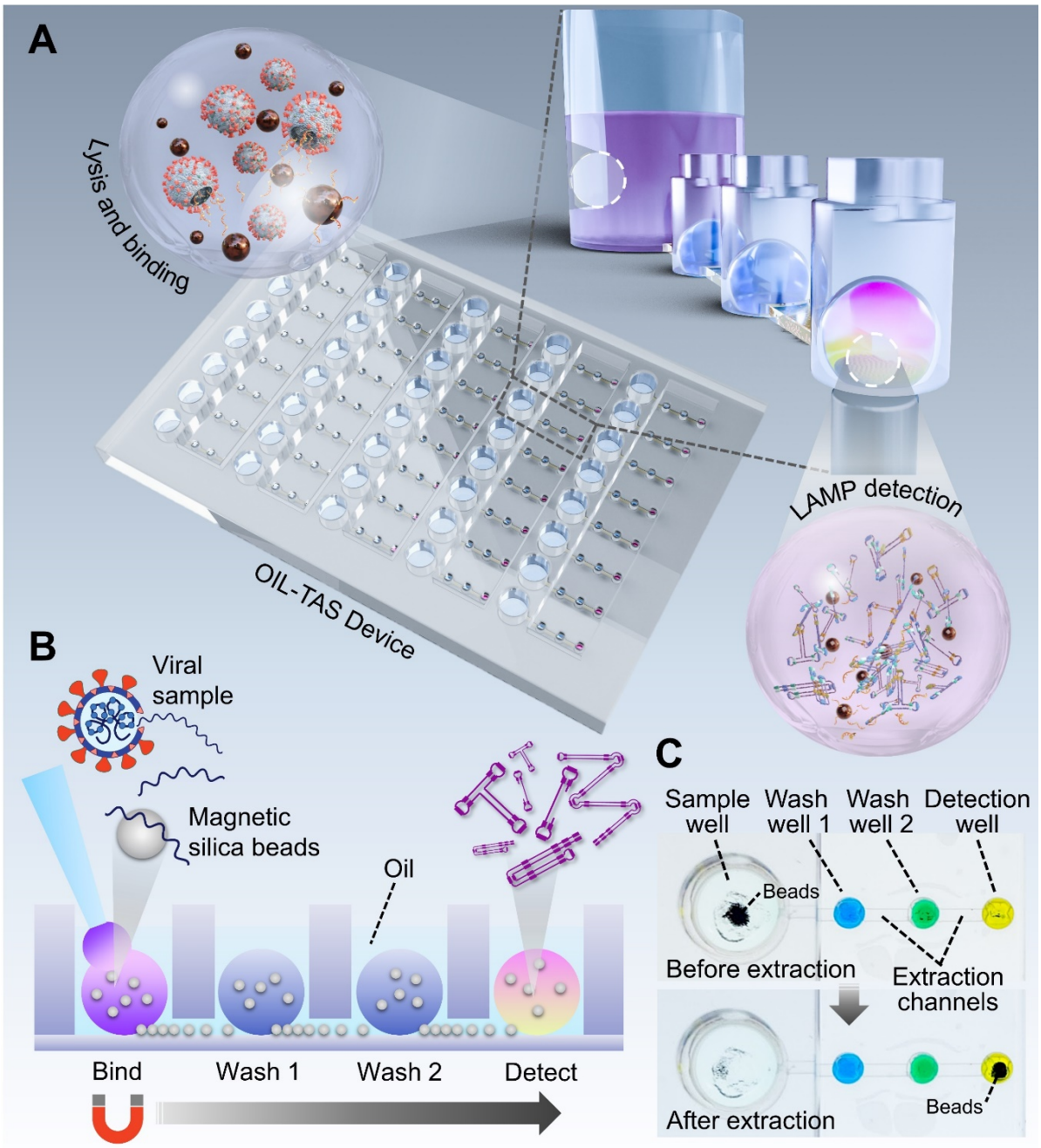

Figure 3.1: Integrated RNA extraction and detection with the OIL-TAS assay. (A) Schematic depicting the design and essential components of the OIL-TAS. (B) Side view cartoon illustrating the operation principle of OIL-TAS sample extraction. Owing to the exclusive liquid repellent (ELR) nature of the device surface, droplets appear spherical which minimizes contact with the device surface and hence biofouling-associated sample loss. (C) Images of a single unit of the OIL-TAS device before and after extraction. Each unit includes a large sample well for sample lysis and binding, followed by two washing wells and a detection well. Interconnecting the wells are oil-filled extraction channels. Wells are filled with droplets of food coloring for visualization.

The oil phase provides droplet isolation and liquid repellent properties, and also serves as a water-immiscible extraction interface for performing ESP: magnetic beads can be added to the aqueous droplets and “extracted” from one droplet to another by dragging a magnet across the bottom of the device for analyte purification (Figure 3.1). Additionally, the oil overlay also provides many other advantages including: 1) it prevents evaporation of droplets, thus enabling reactions that require heating (such as isothermal amplification) to be performed using much smaller volumes, 2) it prevents cross-contamination of reagents/samples and LAMP-amplified products, 3) it prevents aerosol formation during operation, as aerosols would be effectively trapped under the oil overlay, 4) it prevents contamination from the environment, as dust particles/other contaminants would be shielded by the oil overlay, and 5) it enables longer-term storage of individual aqueous reagents in the plate via freezing (-20 ºC).

In order to robustly immobilize the spherical ELR droplets, we designed an array of wells for trapping the droplets, with shallow extraction channels interconnecting the wells for performing extraction (Figure 3.1). One extraction unit of the device consists of a large sample well connected to 3 small wells (for wash 1, wash 2, and detection) (Figure 3.1B and 1c). Each device the size of a microtiter plate (127.76 mm x 85.48 mm) contains 40 extraction units which allows for the simultaneous parallel processing of 40 samples. The whole device is treated using ELR chemistry, which ensures that any given surface of the device is fully repellent to aqueous media to prevent biomolecule adsorption. Adding silicone oil into the sample well fills all downstream wells and extraction channels concurrently with oil, owing to hydrophobic wetting from the ELR surface coating. When

aqueous droplets are pipetted into the oil-filled wells, it forms an array of oil-immersed aqueous droplets separated by oil-filled extraction channels (Figure 3.1). The hydrophobicity of the ELR coating also prevents the aqueous droplets from wicking into the extraction channels. The device is fabricated from 3 sheets of heat-resistant, optically transparent plastic (polycarbonate, Lexan) which provides advantages including a wide working temperature range (-40 ºC to 115 ºC), uniform chemical properties throughout the device, and compatibility with mass manufacturing injection molding processes (Figure 3.2A).

The optically clear thin device bottom (127 μm) allows for efficient magnetic manipulation, rapid heat transfer, and optical access, making the device compatible with visual, absorbance, fluorescence, luminescence, and microscopy-based readouts. The vertical pitch of the wells is 9 mm to enable parallel operation via a standard multichannel pipet, whereas the horizontal pitch is 4.5 mm (corresponding to a conventional 384-well plate) to enable data acquisition via microplate readers. The inlets of the small wells (wash well 1, wash well 2, and detection well) incorporate a non-circular collar to help align the pipet tip during liquid dispensing (Figure 3.2B). The non-circular collar design can prevent the circular pipet tip from forming a tight seal over the inlet, allowing oil to escape over the top of the well when being displaced by pipetting aqueous media into the well. The collar also prevents the aqueous droplet from accidental escape from the top of the well, as long as the diameter of the dispensed droplet is larger than the opening of the collar.

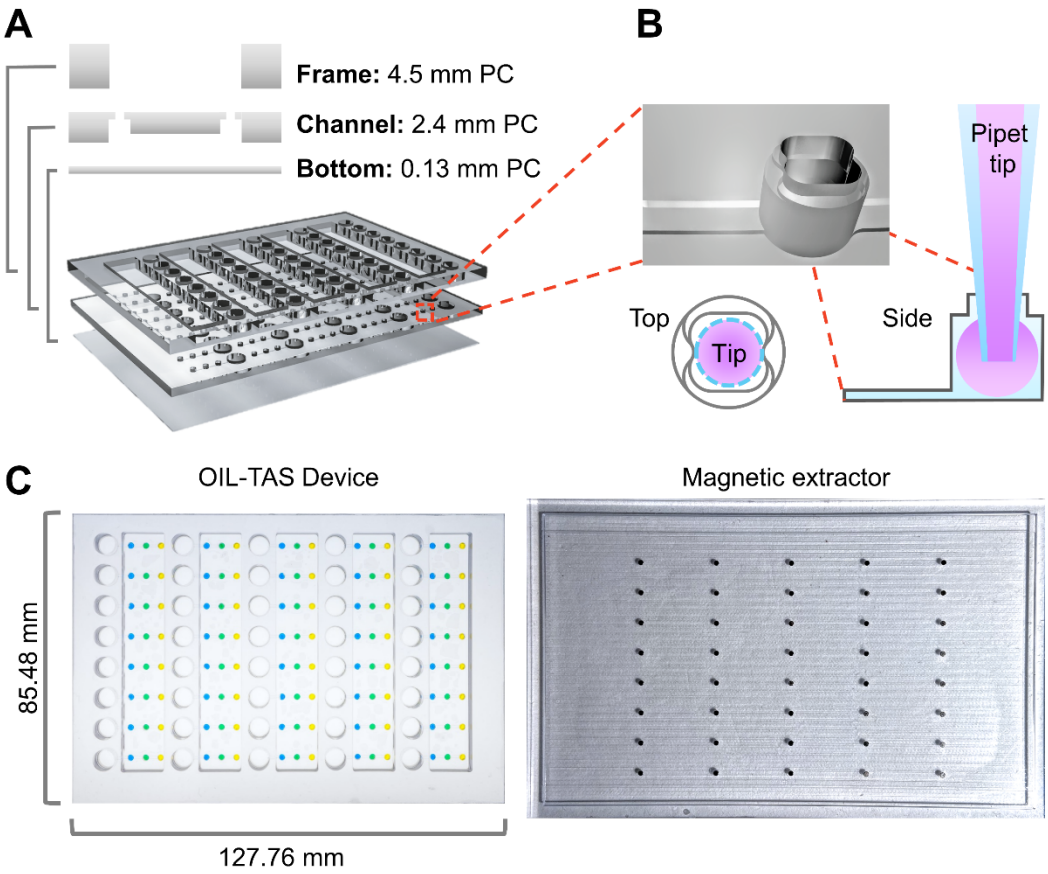

Figure 3.2: Design and assembly of the OIL-TAS device. (A) Exploded view of the OIL-TAS device consisting of 3 layers fabricated from polycarbonate (PC). (B) Design of well collar for pipet tip alignment and preventing droplet escape. (C) Images of the OIL-TAS device (left) and magnetic extractor (right). Food coloring was added to the wells to facilitate visualization.

3.3.2 Assay design and characterization

When using the OIL-TAS device for SARS-CoV-2 testing, the number of operation steps is minimized to 1) add oil, washing solutions, and LAMP reaction solution into the device, 2) mix sample and lysis buffer/beads in a plate, 3) transfer the bead/sample mixture to the device via a pipet, and perform extraction by dragging a magnet across the bottom of the device, 4) place the device in an oven for isothermal amplification, and 5) data readout via visual inspection or an image acquisition device (flatbed scanner, camera/smartphone, or plate reader) (Figure 3.3).

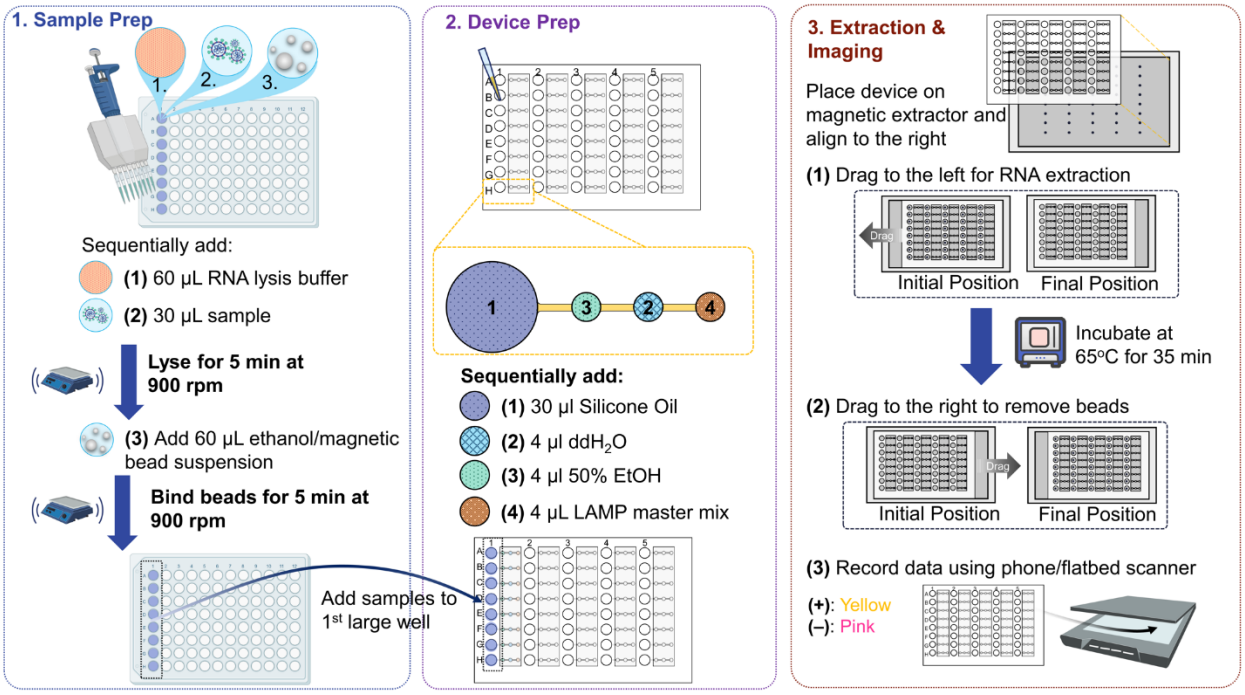

Figure 3.3: Graphical operation protocol for SARS-CoV-2 testing using OIL-TAS.

An operator can perform the whole process manually in less than 30 min for a 40-sample device (excluding the isothermal amplification time), although this can be significantly shortened by using reagent pre-loaded plates and an automated liquid handling system. This compares favorably to commercial automated RNA extraction systems, which commonly take between 45~120 min to process 96 samples[35-37]. It's worth noting that the reason for performing the sample lysis/bead binding step off-device on a well plate is to enable bead mixing via orbital shaker, as well plates are available with taller walls to prevent spillage and cross-well contamination during shaking. Fabricating the OIL-TAS device with comparably tall walls to enable on-device bead mixing is feasible with injection molding processes but is more challenging and impractical to manufacture at scale using lab prototyping techniques (CNC milling).

To quantify the sample purification performance of the OIL-TAS method, we evaluated the amount of liquid carryover from one droplet to another during the magnetic extraction process in the OIL-TAS device using a fluorescent molecule (acridine orange) as a model contaminant (Figure 3.4). Results show only 46.4 nL of aqueous solution was carried over from one droplet to another during the magnetic extraction process (equivalent to 1.16% of the 4 µL droplet), which means that approx. ~0.00015% of contaminating solution will remain after the 3 sequential extractions (Figure 3.4).

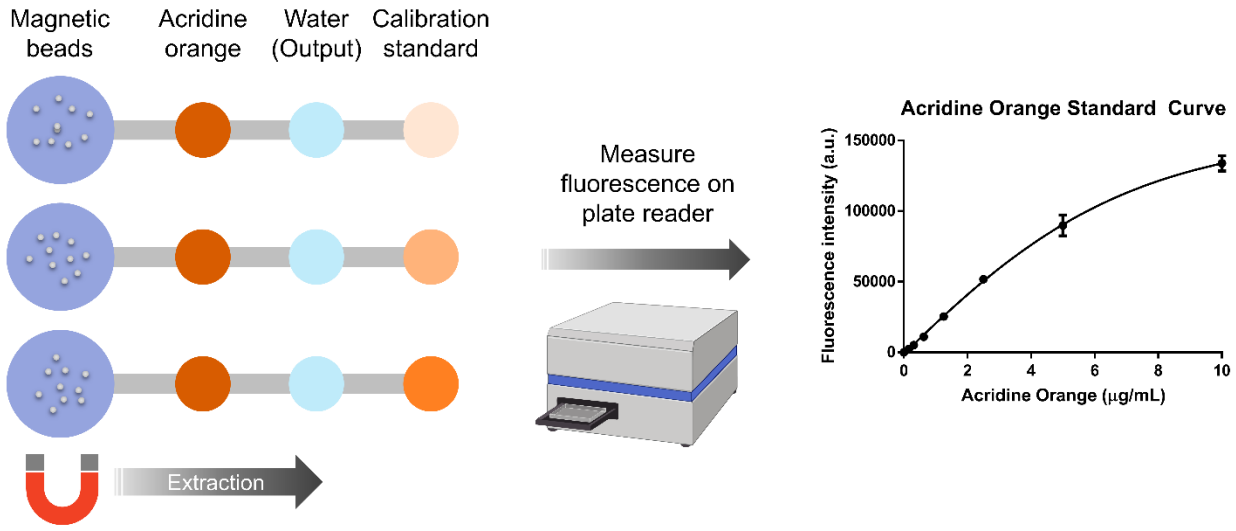

Figure 3.4: Extraction carryover in the OIL-TAS. The amount of carryover was calculated by fitting the fluorescence intensity of the water (output) droplet to the serially diluted acridine orange standard curve.

Owing to the harsh protein denaturing properties of the lysis/binding buffer, we implemented 2 washes as a fail-safe measure to prevent any residual carryover from inhibiting the downstream LAMP reaction. We also tested a variety of channel heights ranging between 100 µm to 600 µm and found that magnetic extraction works throughout this broad range of channel heights. However, to prevent bead clogging during extraction or accidental droplet escape through the extraction channels during device handling, we

selected an optimized height of 200 µm and a width of 800 µm for the extraction channels. We validated that the droplets in this design were highly stable without any observed escape or cross contamination after rocking on a rocking platform shaker at 30 rpm for 30 min (Figure 3.5) or even after vigorous shaking on an orbital plate shaker at 900 rpm.

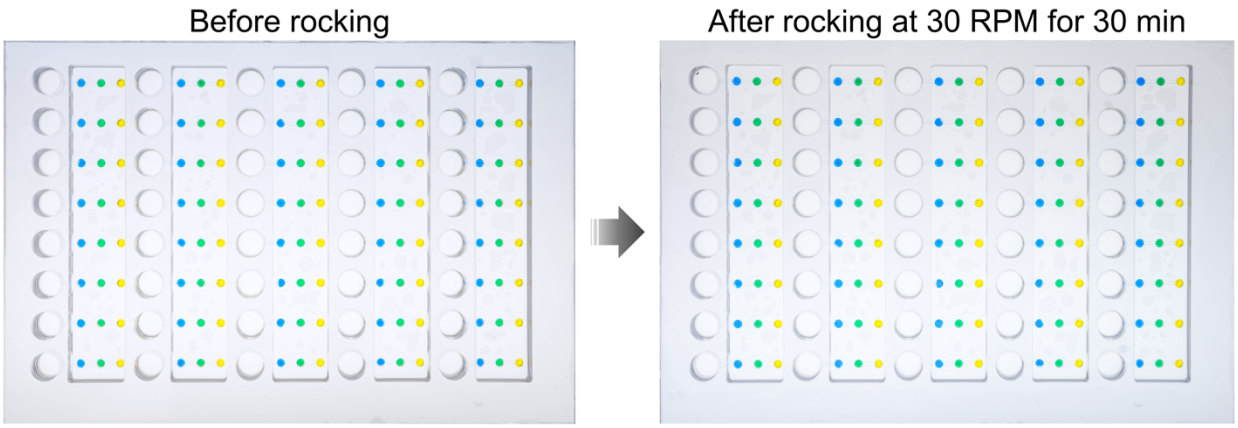

Figure 3.5: Droplet stability of the OIL-TAS. No droplets were dislodged from the wells in the device after rocking on a rocking platform shaker at 30 RPM for 30 min.

To avoid the shortage and supply chain issues with scaling up testing for SARS-CoV-2, we designed our assay to 1) be compatible with completely open source, non-proprietary materials and reagents for RNA extraction, and 2) use very little (4 µL) proprietary reagent (colorimetric LAMP master mix) per reaction to conserve on limited materials and reduce cost. A main bottleneck in RNA extraction supplies is the proprietary nature of most reagents in commercial RNA extraction kits, including the lysis/binding buffer, washing buffers, as well as magnetic beads, which constrains supply to the production capacity of a given company. However, it is known that the majority of commercial solid-phase RNA extraction methods employ variants of a guanidine salt/silica binding chemistry reported in 1990 by Boom et al[38]. RNA binds to silica surfaces (such as silica columns or magnetic silica beads) under high guanidine salt conditions in the presence of an alcohol

(commonly ethanol or isopropanol), which are the major active ingredients in RNA lysis/binding buffers. There have been efforts to develop various open-source RNA lysis/binding buffer recipes from the scientific community[39-43], which were demonstrated by the authors to be similar in performance to commercial proprietary kits. We adopted a lysis buffer recipe reported by Escobar et al.[39] with slight modifications (recipe in Materials and Methods section) and found it to perform well in our system. We also tested magnetic silica beads from different vendors (MagAttract beads from Qiagen, MagneSil beads from Promega, MagBinding beads from Zymo Research, and SeraSil-Mag beads from Cytiva) for compatibility with this open-source RNA extraction chemistry and our OIL-TAS system. We found that the beads from these vendors were all compatible with OIL-TAS extraction process and successfully extracted RNA from gamma-irradiated inactivated SARS-CoV-2 viral particles spiked into viral transport media (VTM) to yield good sensitivity via LAMP detection with an *N* gene primer set[44] targeting SARS-CoV-2 (Figure 3.6).

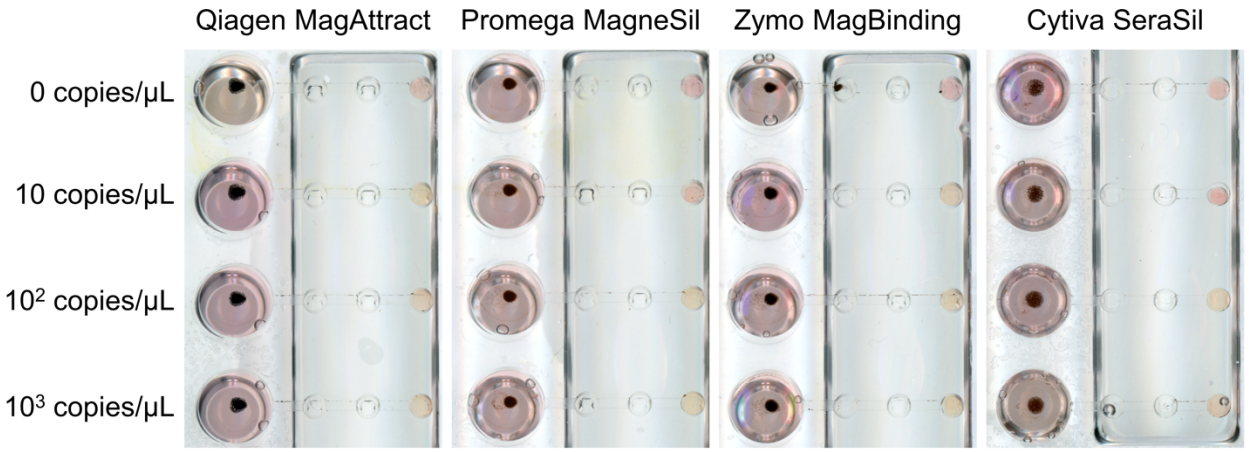

Figure 3.6: Integrated extraction and LAMP detection of γ-irradiated inactivated SARS-CoV-2 particles with OIL-TAS. Performance of the OIL-TAS assay with magnetic silica beads from various vendors paired with an open-source lysis buffer (recipe in Methods section) for integrated RNA extraction and LAMP detection of SARS-CoV-2. Magnetic beads are magnetically moved back into the sample (large) well following LAMP amplification to enable clearer visualization of color change.

We selected the *N* Gene primer set reported by Broughton et al.[44] because it was granted emergency use authorization (EUA) by the U.S. Food and Drug Administration for Mammoth Biosciences[45] and Color Genomics[46] for SARS-CoV-2 testing. We did observe minor differences in magnetic responsiveness and performance between the beads from different vendors, although minor optimizations for each bead type may further improve performance. Qiagen MagAttract beads were selected for following experiments due to their higher magnetic responsiveness and sensitivity.

To further improve on-site assay throughput and operation simplicity, we also tried preloading the OIL-TAS device to contain most of the necessary assay reagents (oil, washing solutions, and LAMP master mix) followed by freezer storage (-20 ºC). We found that after a week-long storage at -20 ºC (longer periods were not tested), the OIL-TAS device still retained similar performance after the freeze-thaw compared to a freshly prepared device (Figure 3.7), suggesting the potential for pre-packaging assays into a ready-to-run format in OIL-TAS.

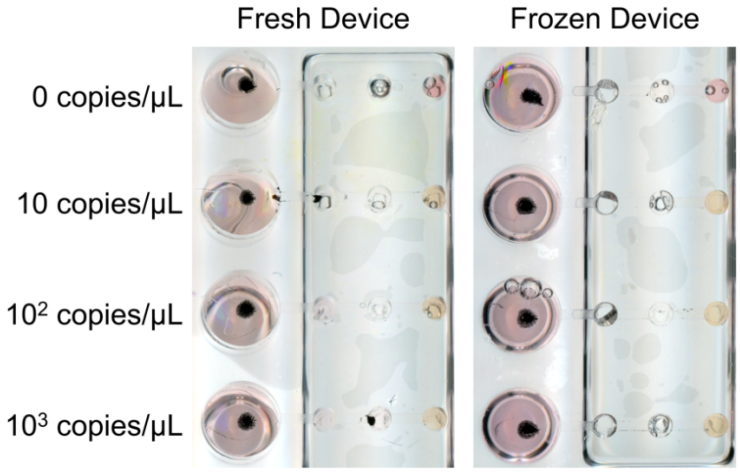

Figure 3.7: Performance of OIL-TAS using a reagent freshly loaded device (left) compared to a reagent pre-loaded device that was frozen for a week at -20 ºC (right).

3.3.3 Performance of the OIL-TAS assay in detecting SARS-CoV-2

We further validated the performance and sensitivity of the assay using replication deficient viral particle samples (SeraCare AccuPlex SARS-CoV-2 Verification Panel) in viral transport media. Results show that we were able to detect down to 1 copy/μL (Figure 3.8A, left panel) using the *N* Gene primer set. The assay also showed no false positives using the RNase P negative extraction control samples included in the SeraCare AccuPlex kit. We observed similar sensitivity of the assay using BEI gamma-irradiated inactivated SARS-CoV-2 viral particles spiked into VTM (Figure 3.8A, right panel). The analytical limit of detection (LoD) of the assay for SARS-CoV-2 viral particles was evaluated by 3 serial 10-fold dilutions of gamma-irradiated viral particles with 10 replicates. Results show that we were able to detect 6/10 samples for 1 copy/μL, and 10/10 for 10 copies/μL and 100 copies/μL concentrations (Figure 3.8B and Figure 3.8C), with none detected (0/10) for 0 copies/μL. These results show that our assay can reliably detect down to 10 copies/μL and approach 1 copy/μL sensitivity, with good specificity.

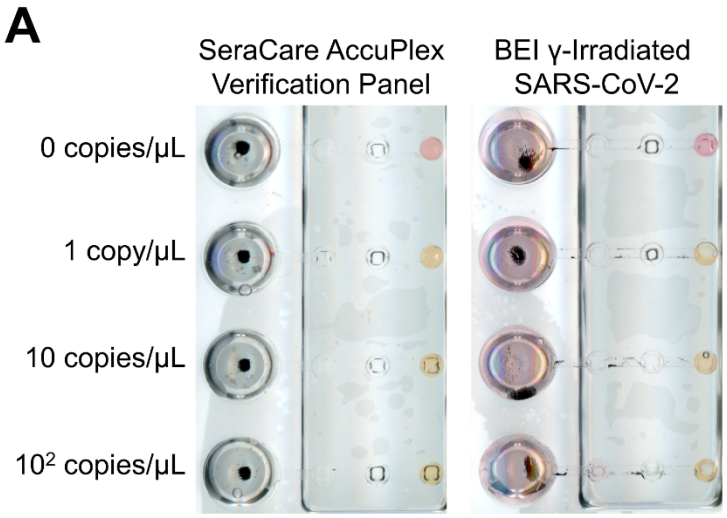

C

Concentration	Detection rate (%)
0 copies/μL	0/10 (0%)
1 copy/μL	6/10 (60%)
10 copies/μL	10/10 (100%)
10^2 copies/μL	10/10 (100%)

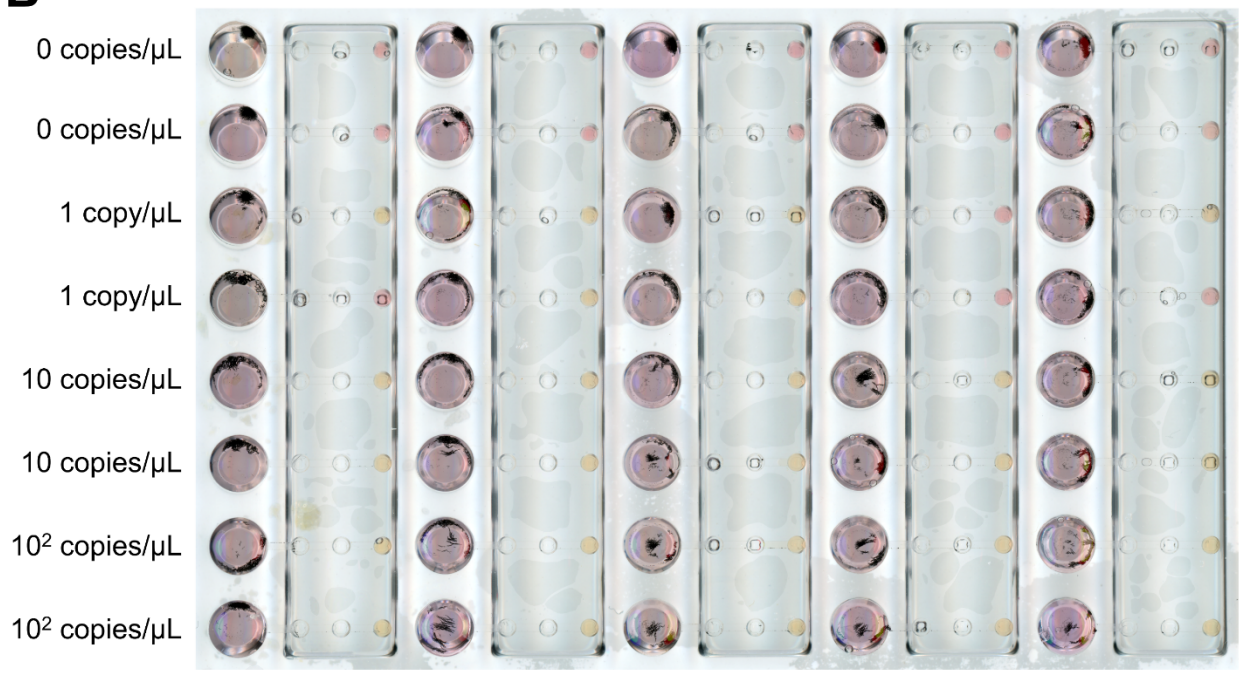

Figure 3.8: Extraction and detection of contrived SARS-CoV-2 viral particle samples using OIL-TAS. (A) RNA extraction and detection of viral particles. Left, synthetic viral particles containing SARS-CoV-2 consensus sequences (AccuPlex verification panel, SeraCare Life Sciences Inc.). Right, γ-irradiated inactivated SARS-CoV-2 particles (strain USA-WA1/2020) from BEI. (B) Sensitivity of the OIL-TAS assay for detecting SARS-CoV-2 viral particles across 10 replicates. (C) Detection rate of the OIL-TAS assay across different viral particle concentrations, quantified from panel (B).

We next tested the performance of OIL-TAS in assaying nasopharyngeal (NP) swab clinical samples from 57 SARS-CoV-2 PCR-positive and 10 SARS-CoV-2 PCR-negative patients stored in 4 different transport medias (universal transport media (UTM), room temperature M4 (RT M4), phosphate-buffered saline (PBS) and saline). The positive samples comprise a wide range of threshold cycle (Ct) values ranging from 14.4 to 39. Results show that OIL-TAS was able to successfully assay NP swab samples across all 4 transport medias with 93% positive percent agreement (PPA) (53/57, n=3) and 100% negative percent agreement (NPA) (10/10, n=3) with RT-qPCR (Figure 3.9A, Table A.1). Out of the 4 discrepant PCR-positive samples, 2 were inconclusive (1/3 detected, RT-qPCR Ct = 34.22 and 32.7, respectively), and 2 were negative (0/3 detected, RT-qPCR Ct = 39 and 36.5, respectively) (Figure 3.9B, Table A.1). Worth noting is that all clinical samples were heat inactivated at 65 ºC for 30 min (to enable safe handling at biosafety level 2) and underwent a freeze-thaw cycle (stored at -80 ºC then thawed at room temperature) prior to running the OIL-TAS assay, which may have a minor impact on sensitivity. On the other hand, the RT-qPCR clinical assays were directly performed on samples without heat inactivation or freeze-thawing.

A

	RT-qPCR positive	RT-qPCR negative
OIL-TAS positive	53	0
OIL-TAS negative or inconclusive	4	10
Agreement	PPA: 53 of 57 = 93%	NPA: 10 of 10 = 100%

B

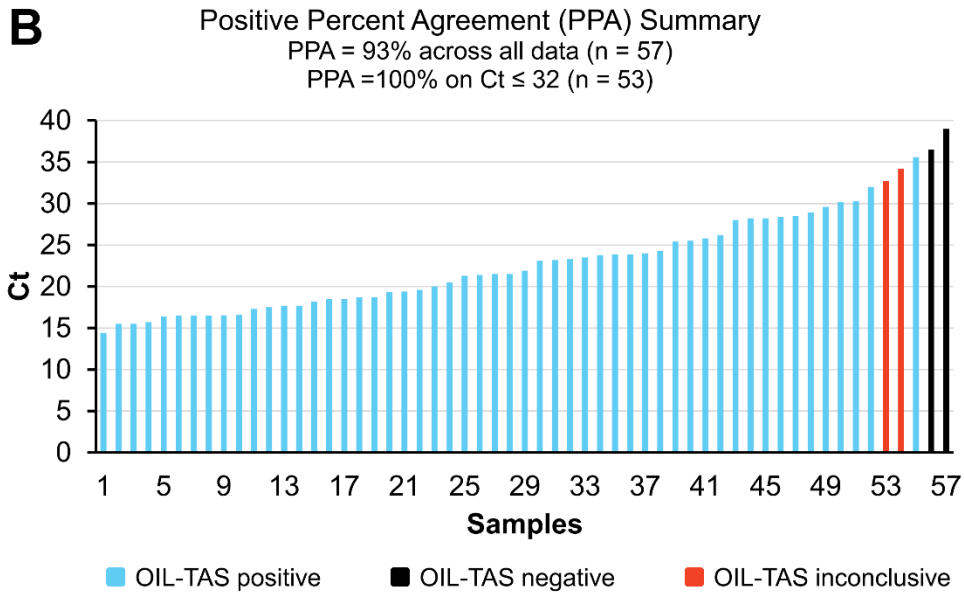

Figure 3.9: Clinical sample assay performance of OIL-TAS compared to RT-qPCR. (A) A total of 67 clinical NP swab samples (57 positive and 10 negative for SARS-CoV-2 determined by RT-qPCR) were tested using the OIL-TAS assay (n=3). PPA, positive percent agreement; NPA, negative percent agreement. (B) Summary of PPA with RT-qPCR Ct values across 57 SARS-CoV-2 positive samples. Out of the 57 PCR-positive samples, 53 tested positive with OIL-TAS (3/3 detected), 2 samples tested negative (0/3 detected), and 2 samples were inconclusive (1/3 detected). RT-qPCR Ct values are plotted in increasing order.

3.3.4 Multiplex detection with the OIL-TAS assay

Most nucleic acid-based diagnostic assays include an extraction (process) control readout in addition to the target sequence to validate that the assay is performing correctly. Thus, we designed a single input, dual output version of the OIL-TAS device (Figure 3.10A) to enable simultaneous multiplexed readout from a single sample to increase the

robustness of the assay. The dual output device footprint remains the same and also has the same number of input sample wells (40 samples) as the single output device, but the number of small wells (wash wells and detection wells) were doubled (Figure 3.10B). This was accomplished by halving the horizontal pitch between the small wells to 4.5 mm, corresponding to that of a 384-well plate, and increasing the size of the sample wells to accommodate larger sample volumes. We employed this design for the simultaneous detection of the *N* gene from SARS-CoV-2 and human RNase P as an extraction process control, or the simultaneous detection of two genomic targets from SARS-CoV-2 (*N* gene and *ORF1a*). This was done by using different primer sets in the 2 output wells, including primers for the *N* gene targeting SARS-CoV-2[44], As1e targeting the open reading frame (*ORF1a*) of SARS-CoV-2[47], and RNase P targeting human cells as a process control[48]. We spiked human A549 cells at a concentration of 10 cells/μL into VTM containing 0, 1, 10, and 100 copies/μL inactivated SARS-CoV-2 particles as a contrived sample. Results show that the sensitivity of the assay was similar with the dual output device, detecting down to 1 copy/μL SARS-CoV-2 viral particles, with all the RNase P extraction controls positive (Figure 3.10C). Multiplexed detection of SARS-CoV-2 using two primers also show similar sensitivity (Figure 3.10D). Worth mentioning is that at 1 copy/μL concentrations, our detection rate was 6/10 using the single output device (Figure 3.8C), but the sensitivity and reliability can be potentially improved in the dual output device as 1 of the 2 primer sets can still detect a positive signal (Figure 3.10D). Multiplexed detection of the *N* gene and RNase P on clinical NP swab samples 1–8 using the dual-output device showed consistent results with the single output device (Figure 3.10E, Table A.1).

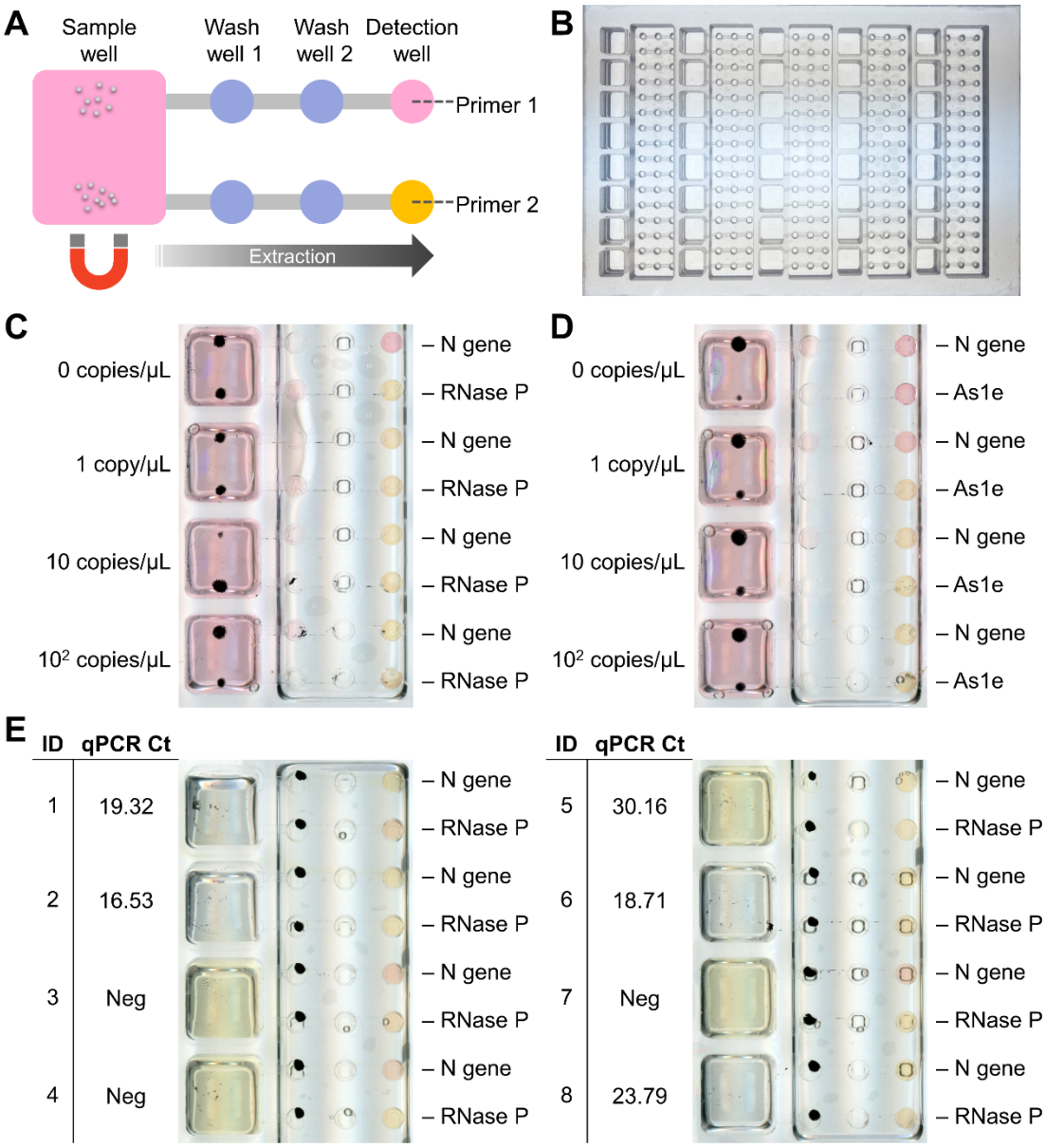

Figure 3.10: Dual output OIL-TAS device enables simultaneous multiplexed detection from a single sample. (A) OIL-TAS can be designed with multiple extraction outputs (2 outputs shown here) leading from a single input sample well, enabling multiplexed detection of a sample by using different primers in the detection well. (B) Image of the dual-output OIL-TAS device which has the same footprint as a 96-well plate (127.76 mm x 85.48 mm). (C) Multiplexed detection of the SARS-CoV-2 *N* gene with an extraction positive control (RNase P). γ-irradiated inactivated SARS-CoV-2 particles were spiked into a cell suspension containing 10 A549 cells/µL in VTM to mimic a clinical sample. (D) Multiplexed detection of two different regions of the SARS-CoV-2 genome (As1e, which targets the open reading frame (*ORF1a*), and the *N* gene). (E) Multiplexed detection of the *N* gene and RNase P on clinical NP swab samples 1–8 (Table A.1).

Simultaneous dual extraction of an RNase P sample also showed that the 2 outputs have equivalent extraction performance as indicated by time to threshold values of LAMP RNase P amplification (Figure 3.11). Worth noting is that the number of output wells (and hence multiplexing targets) may be scaled up with just minor modifications to the current design.

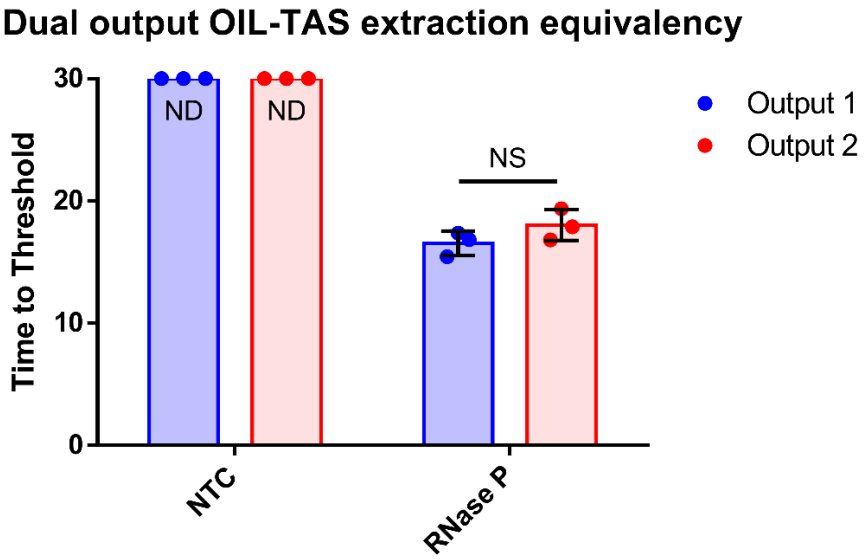

Figure 3.11: Extraction equivalency of the dual output OIL-TAS device. A sample containing RNase P RNA was extracted in parallel into detection well 1 and detection well 2 of the dual output OIL-TAS device. Extraction equivalency of the two wells was evaluated by time to threshold values of LAMP RNase P amplification. NTC: no template control, ND: Not detected, NS: Not significant, determined using 2-tailed Student's t-test. Data are represented as mean values +/- SD from 3 replicates.

3.4 Conclusions

In summary, the OIL-TAS method provides a simple and fast integrated solution from sample to answer for SARS-CoV-2 testing. The OIL-TAS is advantageous in several ways: 1) greatly reduced operation steps. RNA extraction and data acquisition are performed

on the same device; 2) reduction in biohazardous medical waste; 3) extraction process is done under an oil overlay, preventing cross-contamination and aerosol formation; 4) endpoint readout decouples reaction (isothermal amplification at 65 ºC in an oven) from detection (flatbed scanner), thus freeing up instrument time for increased assay turnaround. A single operator can process a device (40 samples) within 30 minutes manually, which, including the 35 min incubation time adds up to a sample-to-result time of approx. 70 min; 5) very low assay reagent and instrumentation cost; and 6) high specificity and good sensitivity. Importantly, although here we demonstrated the OIL-TAS using a manual operation protocol, the conventional plate format of the OIL-TAS device makes it very easily adaptable to an automated workflow using commercially available automated liquid handling systems and plate readers for further increased throughput. We've also shown that the OIL-TAS assay has good sensitivity for a LAMP-based test and was able to detect all SARS-CoV-2 positive NP swab samples with a qPCR Ct ≤ 32. However, we acknowledge that further validation and potential assay modifications would be required for using the OIL-TAS assay on different sample types (i.e., oropharyngeal swabs, saliva, etc.). Worth noting is that the thermoresistant construction of the OIL-TAS device makes it compatible with thermocycling operations, potentially enabling alternative readouts such as qPCR.

A variant of the OIL-TAS design, scaled down for single patient, point-of-care at home testing is also currently under development.

3.5 Materials and Methods

3.5.1 Device Fabrication

Devices were milled out of 2.4 mm (for channels) and 4.5 mm (for top frame) thick polycarbonate sheets (LEXAN 9034, United States Plastic Corporation) using a computer numerical control (CNC) 3-axis mill (Tormach, PCNC 770). Following milling, the two pieces were thoroughly washed with 100% isopropyl alcohol and air dried using an air gun. The two milled pieces were then aligned and placed on top of a 0.005 inch (127 μm) thick polycarbonate sheet (TAP Plastics) and bonded together in a thermal press (Carver Press, 3889.1NE1001) with a pressure of 3000 Kg for 40 min. The bonded device was then treated with oxygen plasma for 2 min at 100 W (Diener Electronic Femto, Plasma Surface Technology). After plasma treatment, the device was placed in a vacuum desiccator with 2 trays (40 μL each) of PDMS silane (1,3'dichlorotetramethylsiloxane, Gelest, SID3372.0). The desiccator was then pumped down to vaporize and condense the PDMS silane onto the device surface at RT overnight to functionalize the device surface. The device was then thoroughly rinsed with 100% isopropyl alcohol then dried using an air gun to remove residual unattached PDMS silane.

3.5.2 Reagent and sample preparation

Colorimetric LAMP master mix was prepared by mixing 100 μL of WarmStart Colorimetric LAMP 2X Master Mix (New England Biolabs), 20 μL of 10X LAMP primer mix, and 80 μL of nuclease free water (for 1 OIL-TAS device). LAMP primer sets were purchased from Integrated DNA Technologies, with primer sequences shown in Table A.2. The primers used include an *N* Gene primer[44], As1e primer[47], and RNase P primer[48], The RNA lysis

buffer was prepared using 4 M Guanidine thiocyanate, 10 mM MES (2-ethanesulfonic acid), 1% Triton X-100, with 1% ß-Mercaptoethanol added right before use. Qiagen MagAttract magnetic silica beads were diluted in 99% ethanol to reach an equivalent of 0.25 µL bead stock/extraction. For bead washing, 50% ethanol and nuclease free water was used for wash 1 and wash 2, respectively. Worth noting is that the rapid (~1 s) and gentle nature of "washing" in the OIL-TAS method (dragging beads through a droplet) allowed us to use water as a washing solution while retaining good sensitivity. Gamma-irradiated inactivated SARS-CoV-2 viral particles (strain USA-WA1/2020) were obtained from the Biodefense and Emerging Infections Research Resources Repository (BEI), (cat# NR-52287) and serially diluted in VTM.

3.5.3 Device operation (single output device)

To prepare the OIL-TAS device, 30 µL of silicone oil was added to each of the sample wells, which, due to the nature of the ELR surface treatment, the oil simultaneously wicks into the extraction channels and wells, forming an oil barrier to separate each well and also prevents sample evaporation. Using a p20 pipette, 4 µL of nuclease-free water, 50% ethanol, and LAMP master mix was sequentially added to washing well 2, washing well 1 and the detection well, respectively. SARS-CoV-2 sample lysis was performed on a 96-well round bottom plate. Briefly, 60 µL of RNA lysis buffer was added to each well, followed by addition of 30 µL sample. The plate was then placed on an orbital plate shaker for 5 min at 900 rpm to lyse the sample. After lysis, 60 µL of MagAttract beads/ethanol suspension (equivalent to 0.25 µL bead stock) was added to the wells and then placed on the plate shaker again for 5 min at 900 rpm for binding. (Note: the sample lysis and

bead binding steps can also be performed in eppendorf tubes or other vessels). The bead/sample mixture with a total volume of 150 µL was transferred to the sample well of the OIL-TAS device to perform extraction. The OIL-TAS device was then placed onto a custom magnetic extractor plate containing an array of neodymium magnets with a diameter of 0.0625 inches (1.6 mm) (Rare-Earth Disc Magnets, MAGCRAFT) positioned under each well, which causes the beads to coalesce above each magnet. The OIL-TAS device was then slid from right to left over the magnetic extractor to perform RNA extraction, which transports each magnetic bead cluster from the sample well through the two washing wells and into the detection well, a process which takes less than 10 seconds. The beads were then left in the detection well for isothermal amplification by placing the device in an incubator/oven set at 65 ºC for 35~50 min. After amplification, beads were removed from the detection well (to allow for better colorimetric visualization) by placing the device on the magnetic extractor and sliding from left to right. Results of the colorimetric LAMP were then recorded by placing the device in a flatbed scanner (Epson Perfection V600 Photo with Epson Scan software). A positive reaction results in a color change of the droplet from pink to yellow, while a negative reaction droplet will remain pink.

3.5.4 Device operation (dual output device)

Minor modifications to the operation protocol were made for the dual output OIL-TAS device (Figure 3.10). The dual output OIL-TAS device was loaded with 50 µL of silicone oil to each of the sample wells. Using a p20 pipette, 4 µL of nuclease-free water, 50% ethanol, and LAMP master mix were sequentially added to washing well 2, washing well

1 and the detection well, respectively in the same manner as the single output device (except different primer sets were used in the two output detection wells). SARS-CoV-2 sample lysis and bead binding was performed in a 96-well deep well plate (or eppendorf tubes). 120 µL of RNA lysis buffer was added to each well of the well plate, followed by addition of 60 µL sample to the lysis buffer. The plate was then placed on an orbital plate shaker for 5 min at 900 rpm to lyse the sample. After lysis, 90 µL of MagAttract beads/ethanol suspension (equivalent to 0.5 µL bead stock) was added to the individual wells and then placed on the plate shaker again for 5 min at 900 rpm for binding. The bead/sample mixture with a total volume of 270 µL was transferred to the sample well of the OIL-TAS device to perform extraction. Magnetic extraction, amplification, and detection was performed as in the single output device.

3.5.5 Human clinical sample collection

Residual diagnostic nasopharyngeal (NP) swab specimens from routine testing were obtained from individuals who met Coronavirus disease 2019 (COVID-19) clinical and/or epidemiological testing criteria. NP swabs were collected in various validated transport media (universal transport media (UTM), room temperature M4 (RT M4), phosphate-buffered saline (PBS) and saline). All samples were de-identified (i.e., stripped of all 18 HIPAA identifiers using the “Safe Harbor” method in accordance with Sections 164.514(b)(2) of the HIPAA privacy rule) prior to testing with OIL-TAS assays. Analyses of residual de-identified diagnostic specimens was performed under biosafety level-2 containment. In order to enable safe handling for OIL-TAS assays, samples were heat inactivated at 65 ºC for 30 min as previously described[49] and then stored at -80 ºC prior

to running the assays. For real time RT-qPCR clinical assays, samples were directly tested without heat inactivation or freezing.

3.5.6 RT-qPCR assay

SARS-CoV-2 RNA was detected by RT-qPCR using either the Hologic Panther Fusion Emergency Use Authorized (EUA) SARS-CoV-2 Assay (Hologic, San Diego, CA) or a United States Centers for Disease Control and Prevention (CDC) multiplex EUA assay (UW Health) using Promega Maxwell Viral TNA reagents on the Promega Maxwell RSC48 and Promega MaxPrep instruments followed by amplifications run on the Roche LightCycler 480 real-time PCR instrument using Promega GoTaq® Probe qPCR Master mix (dUTP) and Promega GoScript™ RT Mix for 1-Step RT-qPCR. The Hologic Panther Fusion EUA and the CDC multiplex EUA (UW Health) assays target *ORF1a*/*ORF1b* and *N1*/*N2* viral sequences, respectively.

3.5.7 Quantification of carryover

Sample purification performance in the OIL-TAS process was evaluated by quantifying the amount of aqueous liquid carryover from one well to another following extraction. This was done by extracting magnetic beads through a fluorescent dye solution (acridine orange) as a model contaminant (Figure 3.4). In brief, a 4 µL droplet of 500 µg/mL acridine orange solution in water was added to washing well 1 (input droplet) of the OIL-TAS device, and a 4 µL droplet of deionized water was added to washing well 2 (output droplet). Carryover was defined by the amount of aqueous liquid that is carried over from the input droplet to the output droplet. In order to obtain a standard curve for fluorescence

quantification, 4 µL droplets of 2-fold serially diluted acridine orange solution ranging from 10 µg/mL to 0 µg/mL were added to the detection wells. 100 µL of 1:400 diluted Qiagen MagAttract bead suspension in deionized water was added to the sample well, then extracted using the magnetic extractor through the acridine orange input droplets and into the water output droplets. The beads were subsequently removed from the output droplets by magnetic extraction in the opposite direction. The OIL-TAS device was then placed in a plate reader (PHERAstar FS, BMG Labtech), and the fluorescence intensity of the output droplets and standard curve droplets was measured with an excitation of 485 nm and emission of 520 nm. Amount of carryover was determined by fitting the fluorescence intensity of the output droplet to the serially diluted acridine orange standard curve.

3.5.8 Data analysis and figure plotting

Data analysis and figure plotting was performed using Microsoft Excel, GraphPad Prism, and Roche LightCycler 480 software. Graphical illustrations were created with BioRender.com, Microsoft PowerPoint, Adobe Illustrator, and Blender (blender.org).

3.6 Acknowledgements

We would like to thank Dr. Brianna Mullins, Dr. Jay Warrick, and Dr. Scott Berry for helpful input and suggestions for the project. This study was funded by a UW WARF COVID-19 Accelerator Challenge award and the National Institutes of Health (NIH 1R01CA247479, NIH P30CA014520, NIH 1R01CA247479-01, NIH OD011106, NIH 5UL1TR002373-03).

Chapter 4

Volumeless reagent delivery: a liquid handling method for adding reagents to droplets without increasing volume[1]

The addition of reagents for assays in digital microfluidic (DMF) systems is traditionally done by merging of droplets containing different analytes or reagents in solution. However, this process significantly increases droplet volume after each step, resulting in dilution of the analyte and reagents. Here, we report a new technique for performing reagent additions to aqueous droplets without significantly increasing the droplet's volume: volume-less reagent delivery (VRD). VRD is enabled by a physical phenomenon we call "exclusive liquid repellency (ELR), which describes a 3-phase system where the aqueous phase can be completely repelled from a solid phase (contact angle ~180°). When performing VRD, a reagent of interest in solution is deposited onto the ELR solid surface and allowed to dry. The ELR surface containing the dried reagent is then immersed under oil, followed by introduction of an aqueous droplet. By dragging the aqueous droplet over the spot of dried reagent using paramagnetic particles or via a physical sliding wall, the droplet can then fully recover and reconstitute the reagent with little increase in its total volume, returning the ELR surface back to its initial liquid repellent state in the process. We demonstrate that VRD can be performed across a wide range of reagent types including sugars, proteins, nucleic acids, antibiotics, and even complex enzyme "kit" mixtures. We believe VRD is a flexible and powerful technique which can further the development of self-contained, multi-step assays in DMF and other microfluidic systems.

[1]This chapter has been modified from a manuscript in preparation. The manuscript includes as authors Duane S. Juang, Joshua M. Lang, and David J. Beebe.

4.1 Preface

This chapter describes a novel liquid handling method enabled by the ELR technologies developed in the prior chapters. The method, named Volumeless Reagent Delivery (VRD), solves a liquid handling issue that has always affected microscale droplet assays: the addition of reagents to an existing droplet. In microscale droplet-based reactions, the addition of reagents generally involves the merging of another similar-sized droplet containing the reagent of interest. This process significantly increases the total volume of the droplet and also dilutes the analytes/reagents of interest after each reagent addition, which is especially problematic for assays requiring sequential, multi-step reagent additions. VRD enables the multistep addition of reagents to microscale droplets without adding volume, and also opens up possibilities for building self-contained assays that don't require manual pipet-based delivery of aqueous reagents.

4.2 Introduction

Digital microfluidics (DMF) is a technique that allows the manipulation of discrete droplets on a planar surface without requiring a sophisticated network of microfluidic channels, valves, or pumps. The manipulation of droplets can be accomplished via a variety of techniques, including, most commonly, electrowetting on dielectric (EWOD)[50,51], dielectrophoresis (DEP)[52,53], magnetic actuation[54,55], surface acoustic waves[56,57], among others. Each droplet can serve as an isolated condition for discrete processes or reactions

to occur in each droplet. DMF has been utilized in various biological assays or processes such as immunoassays[58,59], DNA library preparation[60-62], enzymatic assays[63,64], and a variety of other bioassays. Despite its numerous advantages and potential, the translation of the technology for real-world use has encountered challenges such as reliability[65], biofouling of the DMF surface when transporting protein-rich solutions[66-68], and the significant increase in droplet volumes when performing reagent addition via droplet merging. There have been some efforts in developing DMF systems with dried reagents/analytes deposited on the device surface[69,70], which mitigates the issue of droplet size increases after reagent delivery and potentially enables the development of fully self-contained DMF systems without the need for the end user to pipet individual reagent solutions for a given experiment. However, these prior studies have neither demonstrated full recovery of the dried reagents from the DMF device surface, nor shown sequential, multi-step recovery of dried reagents via DMF droplets (only single-step), suggesting that surface fouling-mediated loss of reagents or analytes is still a major challenge. Here we report a method which helps address some of these challenges: volumeless reagent delivery (VRD), which enables the sequential delivery and full recovery of dried reagents (even high concentration proteins) into aqueous droplets with hardly any increase in volume, made possible via a 3-phase system we call exclusive liquid repellency (ELR).

ELR describes a physical phenomenon in which an aqueous phase can be completely repelled from a solid phase (contact angle ~180°) in the presence of an oil phase given specific oil and solid surface chemical properties[25]. This physical phenomenon is

governed by the fine balance of interfacial energies between the solid, oil, and aqueous phases. Namely ELR will occur if the sum of the solid/oil and aqueous/oil interfacial energies is equal to or less than the solid/aqueous interfacial energy; otherwise adhesion of the aqueous solution to the surface (contact angle < 180°) will occur. We found that this condition can be realized when using a PDMS-silane modified surface as the solid phase paired with silicone oil as the oil phase. The aqueous liquid repellent properties of the ELR 3-phase system allows aqueous solutions to be fully repelled from the solid phase, preventing adsorption or fouling of biomolecules onto the surface and mitigates issues with droplet-to-surface adhesion during operation.

VRD harnesses the liquid repellent properties of ELR to enable delivery and full recovery of dried reagents into an aqueous droplet with hardly any change in the droplet's volume (Figure 4.1). In VRD, a reagent of interest in solution is deposited onto an ELR surface and allowed to dry under a vacuum. The ELR surface containing the dried reagent is then immersed under oil, followed by introduction of an aqueous droplet (which can contain paramagnetic particles (PMPs)) into the oil. By dragging the aqueous droplet over the spot of dried reagent using a magnet or via a physical "sliding wall" which entraps the droplet, the aqueous droplet can then fully pick-up and reconstitute the dried reagent with hardly any increase in its total volume (Figure 4.1), simultaneously returning the device surface back to its original liquid repellent state in the process. Importantly, VRD contrasts with the more traditional reagent addition method in DMF systems done by merging of two discrete droplets, which results in a large increase in droplet volume[71].

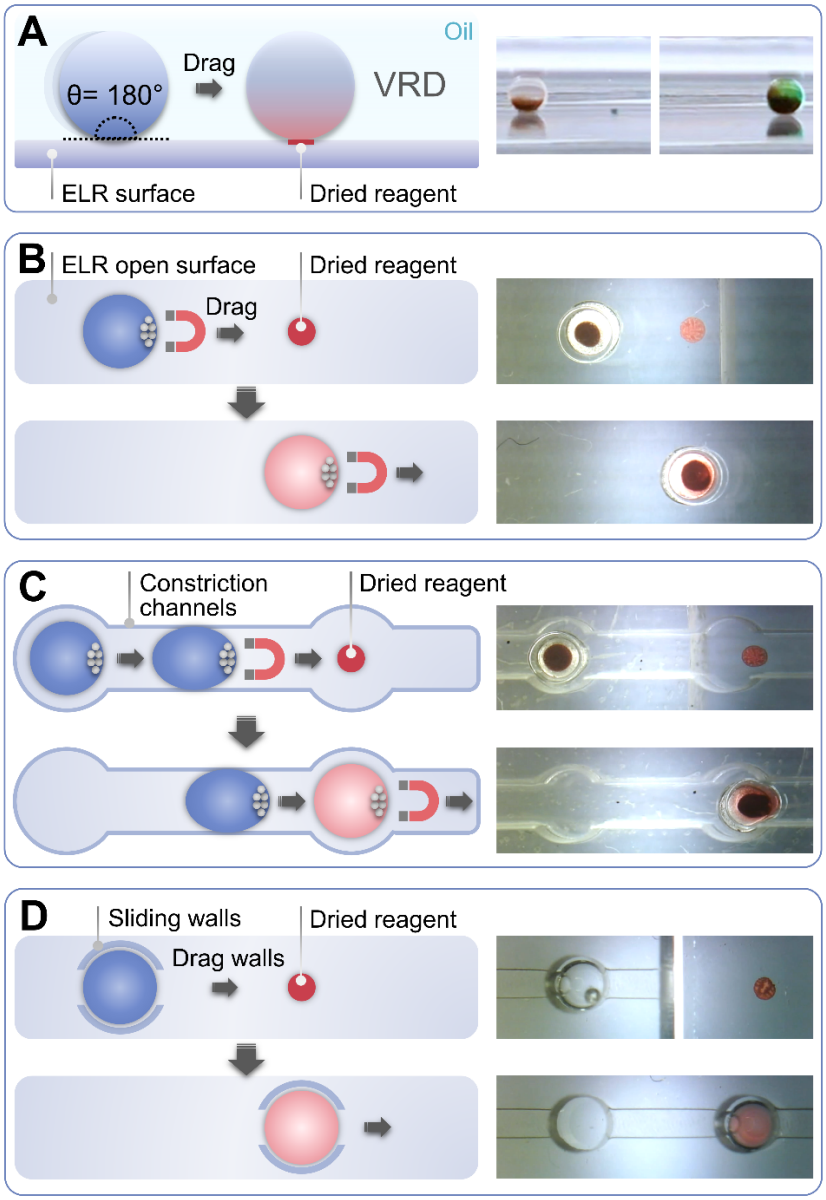

Figure 4.1: Operation principle and different configurations of VRD. (A) Side view of VRD process. An aqueous droplet is dragged across an ELR surface and into contact with a dried reagent spot on the surface (green food dye spot on right panel image), which picks up and reconstitutes the dried reagent. (B) The "open surface" configuration of VRD. An aqueous droplet containing PMPs is added to the device above a magnet, which holds the droplet in place. The droplet is then dragged across the ELR surface and into contact with a spot of dried reagent using the magnet. The droplet can fully pick up and reconstitute the dried reagent, returning the surface back to its original liquid repellent state. (C) The "constriction channel" configuration of VRD. To prevent the movement of droplets after removal of the magnetic field, we designed a device insert consisting of an array of wells with interconnecting constriction channels which are narrower than the

diameter of the droplet. The constriction channel insert is also treated with ELR chemistry, which prevents aqueous droplets from sticking to the device walls and impeding droplet movement. (D) The “sliding wall” configuration of VRD. This configuration employs a sliding ELR-treated physical “wall” insert which entraps the aqueous droplet and allows the droplet to be pushed along the surface of the device by physically sliding the insert. The wall has a 200 μm tall channel cutout to provide clearance for the dried reagent to pass under during droplet manipulation.

The VRD technique is made possible primarily due to the highly aqueous-repellent characteristic of ELR, which prevents fouling-mediated sample/reagent loss caused by nonspecific adsorption of molecules to the device surface. Importantly, the near complete reagent recovery capability of VRD allows the operation to be performed multiple times sequentially, enabling the multi-step addition of different reagents in a row via a simple droplet dragging operation, all while keeping the total volume of the droplet mostly constant. We’ve also demonstrated that VRD is compatible with a wide range of different biomolecule types, including sugars (dextran, trehalose), proteins (IgG antibodies), nucleic acids (DNA), small molecule antibiotics (gentamicin), and complex enzyme/substrate/buffer “kit” mixtures (CellTiter-Glo). The device for performing VRD (modified from an OmniTray well plate) benefits from having a thin, transparent glass bottom construction, enabling optical assay readouts including microscopy and luminescence, as well as efficient magnetic droplet manipulation.

We propose that VRD is a highly flexible and widely applicable technique which helps solve some of the issues plaguing traditional DMF systems, potentially enabling the development of self-contained microfluidic systems which can perform complex, multi-step assays with simplicity and ease of operation.

4.3 Materials and Methods

4.3.1 Fabrication of VRD devices

A 43 mm x 60 mm area was cut out of the bottom of an OmniTray single-well plate (Thermo Scientific Nunc) using a computer numerical control (CNC) 3-axis mill (PCNC 770, Tormach). Medical grade double-sided tape (ARCare 90106, Adhesives Research) was cut using a laser engraver (350-60W CO_2 Laser, Automation Technology). After removal of the protective backing on the double-sided tape, a 48 mm x 65 mm x 0.17 mm coverslip (Gold Seal Cover Glass) was aligned and adhered to the double-sided tape. The coverslip with the attached tape was then aligned and adhered to the bottom of the OmniTray cutout. To further prevent oil leakage, the outer edges along the coverslip were sealed using Duro Super Glue. The coverslip bottom OmniTrays were then treated with oxygen plasma for 2 min at 100 W (Diener Electronic Femto, Plasma Surface Technology). After plasma treatment, the OmniTray was placed in a vacuum desiccator with 2 trays (40 µL each) of PDMS silane (1,3'dichlorotetramethylsiloxane, Gelest, SID3372.0). The desiccator was then pumped down to vaporize and condense the PDMS silane onto the device surface at RT for at least 1 hour to functionalize the device surface. The OmniTray was then thoroughly rinsed with 100% isopropyl alcohol then dried using an air gun to remove residual unattached PDMS silane. An image of the finished device containing dried spots of food dye on the device surface is shown in Figure 4.2.

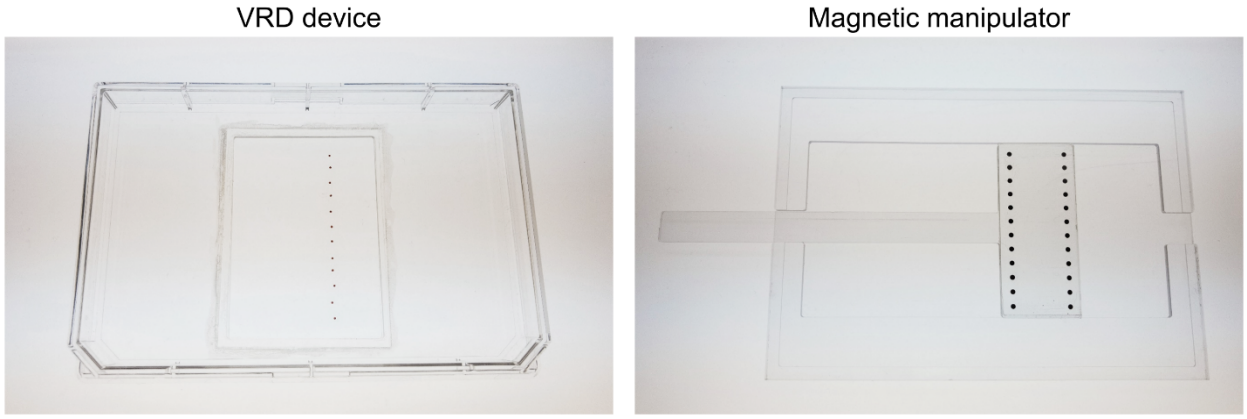

Figure 4.2: Images of the device for performing VRD (modified from a commercial OmniTray well plate) with dried spots of food dye (left) and the magnetic manipulator (right) for performing PMP and droplet actuation.

To form the ELR surface, a drop of silicone oil (viscosity: 5 cSt, Sigma Aldrich) was deposited on the device surface, then blown off using an air gun to form a thin coating of silicone oil on the surface. The constriction channel inserts and the sliding wall inserts were milled out of 2.4 mm thick polycarbonate sheets (LEXAN 9034, United States Plastic Corporation) using a 3-axis CNC mill (PCNC 770, Tormach). Following milling, the polycarbonate device inserts were thoroughly washed with 100% isopropyl alcohol, dried using an air gun, and plasma and PDMS silane treated in the same way as above. The constriction channel or sliding wall inserts were then placed on top of the coverslip in the OmniTray VRD device. For creating patterned hydrophilic spots on the ELR surface of the device, which can be used as “traps” for capturing and immobilizing aqueous droplets[24], we placed a PDMS mask with a column of 2 mm through-holes on top of the PDMS-silane-treated coverslip and oxygen plasma-treated the device (2 min at 100 W) to selectively etch away the PDMS-silane on the exposed areas of the PDMS mask, followed by removal of the PDMS mask.

4.3.2 Fabrication of magnetic manipulator

A 4 mm polystyrene (PS) sheet (Goodfellow) was CNC milled (PCNC 770, Tormach) to fabricate the magnetic manipulator for performing magnetic bead manipulation. The sliding magnetic manipulator was fitted with individual rare-earth circular magnets (diameter 1.6 mm, thickness 0.8 mm, Magcraft) with a pitch of 4.5 mm between each magnet. An image of the magnetic manipulator is shown in Figure 4.2.

4.3.3 VRD of Texas Red dextran

1 μL droplets of Texas Red dextran (10,000 MW, Invitrogen) at various concentrations (5, 1, 0.2, and 0 μM) were deposited onto the VRD device surface using a pipet, then dried in a vacuum desiccator till all the spots appear fully dry. The device was then placed on the magnetic manipulator, filled with silicone oil (viscosity: 5 cSt, Sigma Aldrich), followed by introduction of 5 μL droplets of water containing 1:10 diluted silica PMPs (MagneSil, Promega) via a pipet. The droplets were pipetted directly on top of each magnet to allow the droplets to be immobilized in place via the PMPs. The droplets were then dragged into contact with the Texas Red dextran spots by sliding the magnetic manipulator and allowed to incubate for ~1 min (incubation time may vary for different types and concentrations of reagent) to reconstitute the Texas Red dextran. 2 μL of the reconstituted droplet was then transferred to a fluorospectrometer (NanoDrop 3300, Thermo Scientific) to perform fluorescence intensity measurements at 610 nm (emission). The input Texas Red dextran solution was diluted 5-fold (to account for the 5-fold dilution when performing VRD with 5 μL droplets on a 1 μL reagent spot) and also measured on the fluorospectrometer to determine the reagent recovery efficiency of VRD.

4.3.4 VRD of IgG antibody

2 µL droplets of Alexa Fluor 488 goat anti-rabbit IgG (Invitrogen) at a concentration of 2, 0.2, and 0 mg/mL in 60 mM Trehalose in ddH_2O were deposited onto the VRD device surface and dried in a vacuum desiccator as described above. The dried IgG spots were imaged on an inverted epifluorescence microscope (Nikon Ti Eclipse) before and after VRD reconstitution to assess if any residual IgG remained. VRD was performed similarly as described above with 2 µL droplets containing 1:10 diluted silica PMPs (MagneSil, Promega). The fluorescence of both the reconstituted droplet and input solution containing Alexa Fluor 488 IgG was measured using a fluorospectrometer (NanoDrop 3300, Thermo Scientific) at 520 nm (emission) to assess recovery efficiency.

4.3.5 VRD of DNA

2 µL droplets of LNCaP cell DNA in buffer AE (Qiagen) at a concentration of 200 and 0 ng/µL were deposited onto the VRD device surface and dried in a vacuum desiccator as described. VRD was performed similarly as described above with 2 µL droplets containing 1:10 diluted silica PMPs (MagneSil, Promega). The absorbance of the reconstituted droplet and input solution containing LNCaP DNA was measured using a UV/Visible spectrophotometer (NanoDrop 1000, Thermo Scientific) at 260 nm to assess DNA recovery efficiency.

4.3.6 Antibiotic dosing of bacteria using VRD

A 1 µL droplet of gentamicin at various concentrations in 2 mM Trehalose (as a carrier) was pipetted onto the ELR device surface as described above. After desiccating the

gentamicin droplets in vacuum, the device was filled with silicone oil, and placed on the magnetic manipulator. 2 μL droplets containing *Pseudomonas aeruginosa* CFP (Strain PA01) at an OD 600 nm of 0.001, 1:10 diluted silica PMPs, and Mueller Hinton broth were then pipetted into the ELR device on top of the individual magnets. The 2 μL droplets were then magnetically transported onto the dried gentamicin spots to perform VRD by sliding the magnetic manipulator. The bacterial droplets were then allowed to incubate at room temperature for 24 h (while sitting on the magnetic manipulator), followed by magnetically dragging the droplets onto a column of patterned hydrophilic spots on the device surface for droplet immobilization and fluorescence microscope imaging on an inverted epifluorescence microscope (Nikon Ti Eclipse). For sequential antibiotic dosing experiments, gentamicin was diluted to 1X, 1/3X, and 1/5X final concentrations and spotted onto the device surface (a single 1 μL gentamicin spot + 4 blank vehicle spots for the 1X concentration condition, 3 gentamicin spots + 2 blank vehicle spots for the 1/3X concentration condition, and 5 gentamicin spots for the 1/5X concentration condition). After drying the gentamicin spots and filling with oil, bacterial droplets were introduced and sequentially magnetically dragged from 1 antibiotic spot to another to perform VRD (with 1 h interval between each VRD addition). Following the 5 additions, the droplets were allowed to incubate at room temperature for 24~48 h, followed by dragging them onto the hydrophilic patterned spots for immobilization and imaging as described above. Fluorescence intensity of the droplets were quantified using Fiji (https://fiji.sc/) with a circular region of interest (ROI).

4.3.7 Antibiotic sequential dosing in well plate

100 µL of *P. aeruginosa* CFP at an OD 600 nm of 0.001 in Mueller Hinton broth was added to a 96-well plate, followed by introduction of 1 µL gentamicin or blank vehicle control at 1 h intervals for a total of 5 additions. The plate was incubated at room temperature for 24~48 h, and bacterial growth was measured via absorbance using an ELISA reader (SpectraMax Plus 384, Molecular Devices) at 600 nm.

4.3.8 VRD of CellTiter-Glo

2 µL droplets of CellTiter-Glo were pipetted onto the ELR device surface. After desiccating the CellTiter-Glo droplets in vacuum, a constriction channel insert was placed onto the glass coverslip bottom of the VRD device then filled with silicone oil. 2 µL silica PMPs diluted 1:10 in PBS were pipetted into column 1 wells of the device insert. 2 µL droplets containing 10000, 1000, 100, 10, and 0 LNCaP cells in RPMI cell media were pipetted into column 2 wells of the device insert. The dried CellTiter-Glo reagents reside within column 3 wells of the device insert. The “extraction channels” between columns 1 and 2 have a cross section of 0.8 mm (width) and 0.3 mm (height), which only allows magnetic beads to traverse and not 2 µL aqueous droplets. The “constriction channels” between columns 2 and 3 have a cross section of 1.2 mm (width) and 2.4 mm (height), which allows 2 µL aqueous droplets to traverse if a dragging force was applied to the PMPs within the droplet. The VRD device was then placed on the magnetic manipulator, and the PMPs were magnetically extracted from column 1 wells into column 2 wells containing the LNCaP cell droplets. The 2 µL cell droplets were then magnetically transported from column 2 wells into column 3 wells onto the dried CellTiter-Glo spots to perform VRD.

The cell droplets were then allowed to incubate at room temperature for 10 min, followed by magnetically removing the PMPs from the cell droplets. Luminescence intensity of the droplets were then immediately measured from the bottom of the plate using a plate reader (PHERAstar FS, BMG Labtech).

4.4 Results and Discussion

4.4.1 Operation principle of VRD

The VRD system consists of reagents that are deposited and dried onto an ELR solid surface. The ELR surface containing dried spots of reagents are then immersed under silicone oil, followed by introduction of aqueous droplets containing analytes of interest which are dragged over the dried reagent spot to perform VRD (Figure 4.1A, Figure 4.3). Although appearing relatively straightforward in principle, we discovered that this operation can be challenging to achieve without the ELR chemistry. For instance, a droplet/PMP ratio that works well for droplet actuation in ELR conditions failed to actuate droplets in a hydrophobic, but non-ELR condition (fluoro silane modified glass with mineral oil) as shown in Figure 4.3. This is likely due to the lower contact angle in the fluoro silane/mineral oil 3-phase system resulting in increased surface adhesion of the droplet.

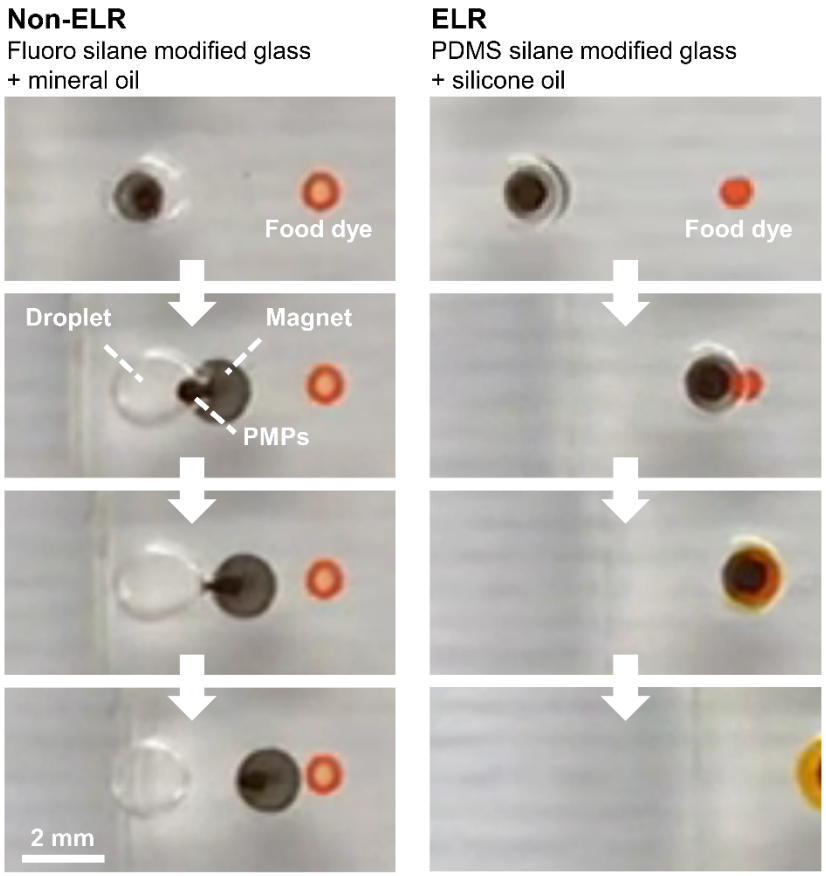

Figure 4.3: ELR (accomplished via a PDMS silane modified glass surface with silicone oil) enables better droplet manipulation via PMPs compared to a non-ELR system (fluoro silane modified glass with mineral oil). Scale bar: 2 mm.

We've developed 3 different configurations of VRD, each with its advantages and disadvantages to suit the desired use case scenario. In the "open surface" configuration of VRD, aqueous droplets containing paramagnetic particles (PMPs) are pipetted onto the VRD device surface to enable contact-less droplet manipulation via an external magnet (Figure 4.1B). This configuration allows for maximal degrees of freedom in droplet movement across all directions on the device surface. However, the open surface configuration also requires that the PMPs be introduced together with the aqueous droplet and pipetted directly on top of a magnet to prevent premature droplet movement on the

hydrophobic ELR surface. If droplet immobilization without a magnet is desired (i.e. for microscope imaging), the device surface will have to be additionally patterned with hydrophilic spots to allow droplets to be “trapped” in a given region of the device. However, once a droplet is trapped in a hydrophilic spot it can no longer be magnetically transported freely on the surface, and hence is more suited for the last step of an assay. The antibiotic dosing experiments in Figure 4.6 and Figure 4.8A employs this configuration. To enable droplet immobilization without the need for a constant external magnetic force or an irreversible hydrophilic droplet trap, we designed a device insert consisting of an array of wells with interconnecting “constriction channels” to physically confine the droplets in the wells (Figure 4.1C). Each well has a diameter of 2 mm and height of 2.4 mm, which can accommodate a 2 μL droplet and allow for easy pipette access. The pitch between each well is 4.5 mm corresponding to that of a 384-well plate to allow for compatibility with conventional plate readers. The wells are interconnected with 1.2 mm wide, 2.4 mm tall constriction channels, which is narrower than the diameter of a 2 μL spherical droplet (~1.56 mm) to provide physical confinement, but still sufficiently wide to allow passage of droplets from one well to another following the application of dragging force via an external magnet (the droplets deform and elongate when traveling through the constriction channels). We tested various widths of the constriction channels ranging from 1 mm to 1.6 mm and found that a width of 1.2 mm is a good balance between good droplet confinement and ease of dragging droplets from one well to another. We’ve also further designed “extraction channels” with a width of 0.8 mm and height of 0.3 mm which permits the passage of magnetic beads but blocks the movement of the droplet, which can be used for removal of magnetic beads from droplets. This configuration is employed in the

CellTiter-Glo VRD experiments in Figure 4.9. Importantly, the constriction channel insert is also ELR-treated, which is essential for preventing the droplets from adhering-to and getting stuck to the channel walls during droplet movement. As such, droplet immobilization in this configuration relies solely on physical confinement, with no hydrophilic surface interactions/wetting involved. The disadvantage of the constriction channel configuration is that it has fewer degrees of freedom in terms of droplet movement compared to the open surface configuration. In both the open surface and constriction channel configurations of VRD, the movement of droplets rely on the use of PMPs in the droplet plus an external magnetic manipulator on the bottom of the device. However, the presence of PMPs can interfere with assays requiring optical readouts (such as microscopy, absorbance, fluorescence, or luminescence measurements) and potentially even the reactions or analytes in the droplet itself. Thus, it would be advantageous to develop an alternative droplet manipulation method for performing VRD that is not dependent on magnetic actuation. Thus, we further developed the “sliding wall” configuration, which adds a device insert consisting of a sliding ELR-treated physical “wall” which entraps the aqueous droplet and allows the droplet to be pushed along the surface of the device by physically sliding the insert (Figure 4.1D). The walls are 2.4 mm tall with a 200 μm tall, 800 μm wide channel cutout to provide clearance for the dried reagent to pass under during droplet movement, but the cutout is shallow enough to prevent aqueous droplets from escaping into the channels. Importantly, the silicone oil also serves as a liquid sealant and lubricant between the sliding wall insert and the bottom ELR device surface, thus preventing any aqueous liquid from seeping into the gap between the insert and the device bottom. Worth noting is that the ELR treatment for the sliding wall insert

is also essential: it prevents droplets from adhering to the walls or wicking into the channel cutouts, and facilitates the formation of a robust oil seal between the sliding wall insert and the device bottom (owing to the high affinity of silicone oil to ELR treated surfaces).

4.4.2 Characterization of VRD performance

To evaluate the reagent recovery performance of VRD, we chose a fluorescently labeled sugar (Texas Red dextran, 10,000 MW) as a model reagent. Droplets of Texas Red dextran at various concentrations were spotted onto the device surface (using the “open surface” configuration device), then dried in a vacuum desiccator. The device was then placed on the magnetic manipulator, filled with silicone oil, then introduced with droplets of water containing 1:10 diluted PMPs via a pipet. The droplets were then dragged into contact with the Texas Red dextran spots by sliding the magnetic manipulator and allowed to incubate for ~1 min to reconstitute the Texas Red dextran. The reconstituted droplet was then transferred to a fluorospectrometer to measure its fluorescence intensity compared to the input Texas Red dextran solution (prior to drying) to evaluate the recovery efficiency of VRD. Results show that the fluorescence intensities of the input and output droplets is very similar for both the 1 and 0.2 μM input concentrations (the fluorescence of the 0.04 μM condition is too low and close to the background to be accurately measured), suggesting very high reagent recovery efficiency (Figure 4.4A). Encouraged by this result, we further performed a sequential VRD experiment to evaluate the ability of the VRD method to perform sequential, multi-step reagent additions. Rows containing 1, 2, 3, and 4 spots of Texas Red dextran were sequentially recovered using VRD to measure the reagent recovery performance ranging from a single addition to 4

sequential additions (Figure 4.4B). Results show that the VRD process not only can successfully perform sequential reagent additions, but also has high reliability as indicated by R^2 value of the regression line (Figure 4.4B), further suggesting near 100% recovery efficiency for each VRD step. To ensure that no cross contamination occurs between adjacent reagent spots, we spotted Texas Red dextran and blank vehicle control in alternating rows and measured the fluorescence of the recovered droplets. As shown in Figure 4.4C, no detectable cross contamination was observed.

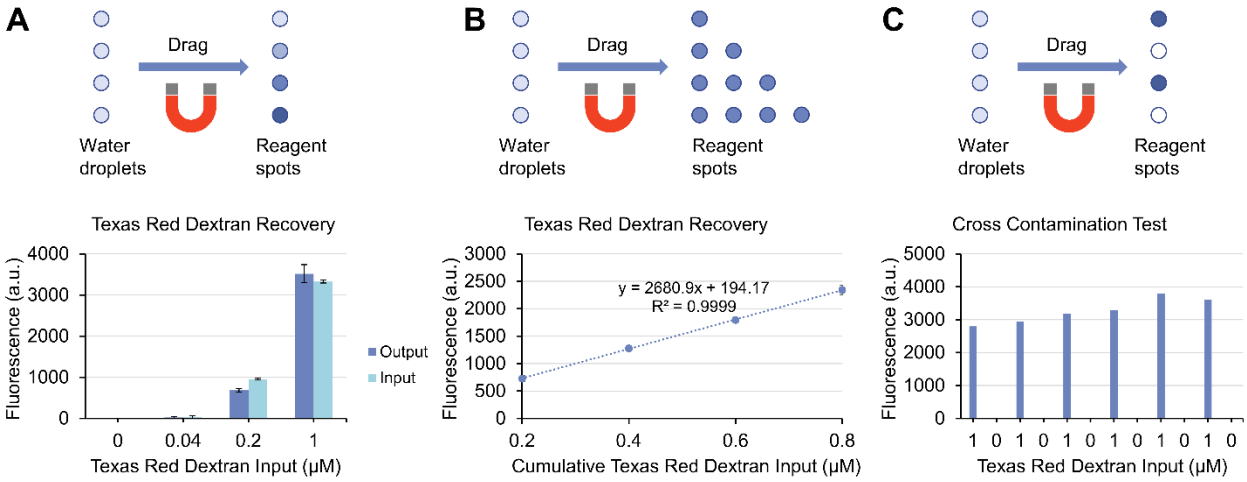

Figure 4.4: Reagent recovery performance of VRD. (A) Recovery of Texas Red dextran at various input concentrations using VRD. (B) Sequential, multi-step recovery of Texas Red dextran using VRD. (C) Blank vehicle and 1 μM Texas red dextran were spotted in alternating sequence and recovered using VRD to demonstrate that cross contamination between adjacent spots does not occur. Error bars denote the standard deviation from 3 technical replicates.

4.4.3 Protein and DNA recovery using VRD

Proteins, especially antibodies, are one of the most widely used molecules in biological assays such as immunoassays and chromatin immunoprecipitation. However, they are also one of the most challenging molecules to work with in DMF systems, especially at high concentrations, often leading to biofouling of the DMF surface which results in process failures stemming from droplets getting stuck at the fouled area[72], or cross-contamination when a droplet is moved across an already used region of the DMF surface[73,74]. This is known to be a significant issue with just actuating an aqueous droplet containing higher concentrations of proteins across a DMF surface, let alone trying to recover a high concentration dried protein spot deposited on the device surface. To test the possibility of recovering proteins using VRD, we spotted a fluorescent antibody solution (Alexa Fluor 488 goat anti-rabbit IgG) at a concentration of 2, 0.2, and 0 mg/mL onto the ELR surface of the device and dried the protein spots in a vacuum desiccator as described above. Trehalose, a commonly used protein stabilizer[75] was included in the antibody solution at a concentration of 60 mM as previously reported[76] for use as a stabilizer and also as a carrier to provide extra “dry mass” for the dried reagent spot, especially for lower amounts of reagent. We imaged the dried IgG spots on an inverted epifluorescence microscope before and after VRD reconstitution to assess if any residual IgG remained on the surface, and also measured the fluorescence intensity of both the input solution and reconstituted droplet using a fluorospectrometer to assess the protein recovery efficiency. Fluorescence images show that barely any fluorescent antibody remained on the surface after performing VRD (Figure 4.5A), even with a high concentration of antibody (2 mg/mL). The measured fluorescence of the input solution

and the reconstituted droplet was also very similar (Figure 4.5B). This, to the best of our knowledge, was not previously achieved in DMF systems. Similarly, we also tested the ability of VRD to reconstitute DNA, a molecule ubiquitously used in molecular bioassays and also explored as a data storage medium in DMF systems[70]. We spotted droplets of LNCaP cell DNA dissolved in buffer AE (Qiagen) at a concentration of 200 and 0 ng/µL onto the device surface and dried the spots under a vacuum as described. After VRD recovery of the DNA spots, the absorbance of the input and reconstituted droplet was measured using a UV/Visible spectrophotometer at 260 nm to assess DNA recovery efficiency, which showed very similar absorbance values for the input solution and reconstituted output droplet (Figure 4.5C), suggesting near complete recovery of the dried DNA with VRD.

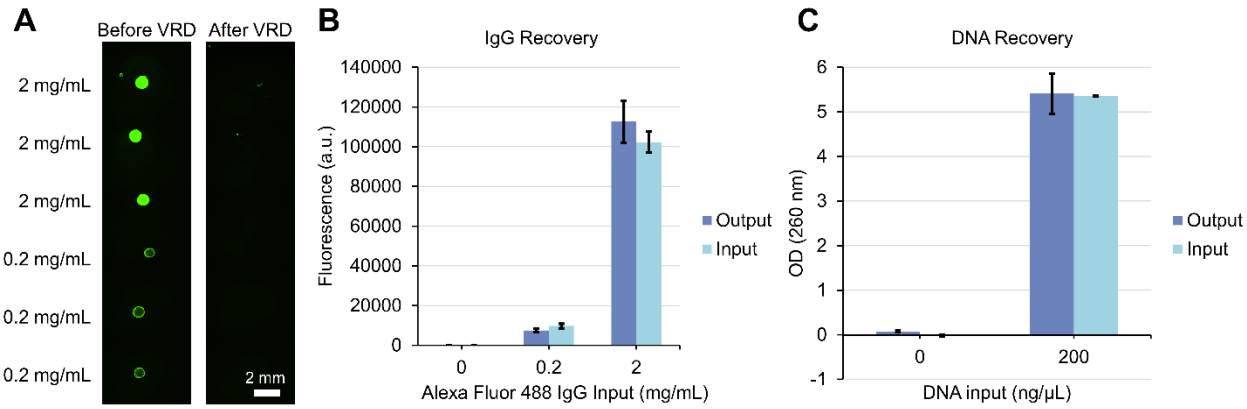

Figure 4.5: Protein (IgG) and DNA recovery efficiency of VRD. (A) Fluorescence microscope images of dried Alexa Fluor 488 IgG spots before (left) and after (right) VRD reconstitution. Scale bar: 2 mm. (B) Fluorescence of the input Alexa Fluor 488 IgG solution (without drying) compared to the output droplet (after VRD reconstitution of the dried reagent) as measured on a fluorospectrometer. (C) Absorbance of the input DNA solution (without drying) compared to output droplet (after VRD reconstitution of the dried reagent) as measured on a UV/Visible spectrophotometer at 260 nm. Error bars denote the standard deviation from 3 technical replicates.

4.4.4 Antibiotic recovery and susceptibility testing of bacteria using VRD

To explore the utility of the VRD method for performing bioassays with live biological specimens, we tried performing an antibiotic dosing experiment with droplets containing fluorescent bacteria (*Pseudomonas aeruginosa* CFP, strain PA01). Gentamicin, an antibiotic known to inhibit *P. aeruginosa*, was spotted and dried onto an "open surface" VRD device containing a patterned column of hydrophilic spots for droplet immobilization during fluorescence microscope imaging. The device was filled with silicone oil (enough to fully cover the 2 µL droplets), followed by introduction of 2 µL droplets containing *P. aeruginosa* CFP and silica PMPs in Mueller Hinton broth. The droplets were then magnetically dragged onto the dried gentamicin spots to perform VRD antibiotic dosing, then incubated at room temperature for 24 h (while sitting on the magnets). After the 24-hour incubation, the droplets were magnetically dragged onto the hydrophilic patterned spots for droplet immobilization and fluorescence microscope imaging (Figure 4.6A).

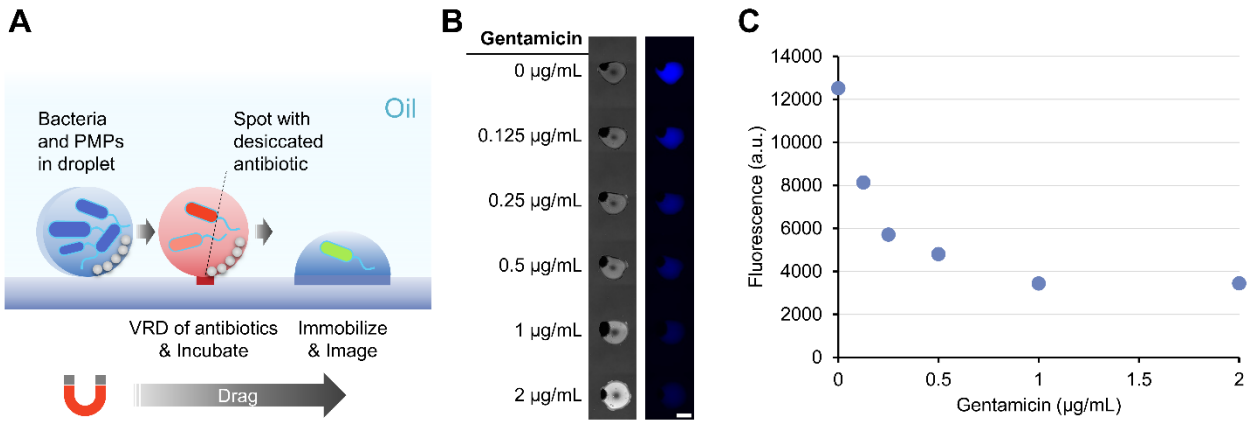

Figure 4.6: VRD of antibiotics (gentamicin) into droplets containing bacteria (*P. aeruginosa* CFP). (A) Schematic of VRD addition of gentamicin into droplets containing *P. aeruginosa* CFP, followed by a 24 h incubation, then immobilization onto patterned hydrophilic spots for microscopic imaging. (B) Bright field (left) and fluorescence (right) image of immobilized droplet containing *P. aeruginosa* CFP after gentamicin treatment with VRD. Scale bar: 1 mm. (C) Quantified fluorescence of immobilized droplets containing *P. aeruginosa* CFP after gentamicin treatment.

The incubation period (which allows the bacteria to grow) was not performed with the droplet immobilized on the hydrophilic spots as we wanted to test the ability of the ELR surface to resist fouling during bacterial growth, especially since *P. aeruginosa* is well known for its ability to form biofilms on mucosal surfaces and medical implants[77]. Results show that the ELR surface was highly effective in resisting biofouling by *P. aeruginosa*, whereas a hydrophobic but non-ELR condition (fluoro silane modified glass with mineral oil) exhibited severe fouling after the same 24 h culture (Figure 4.7).

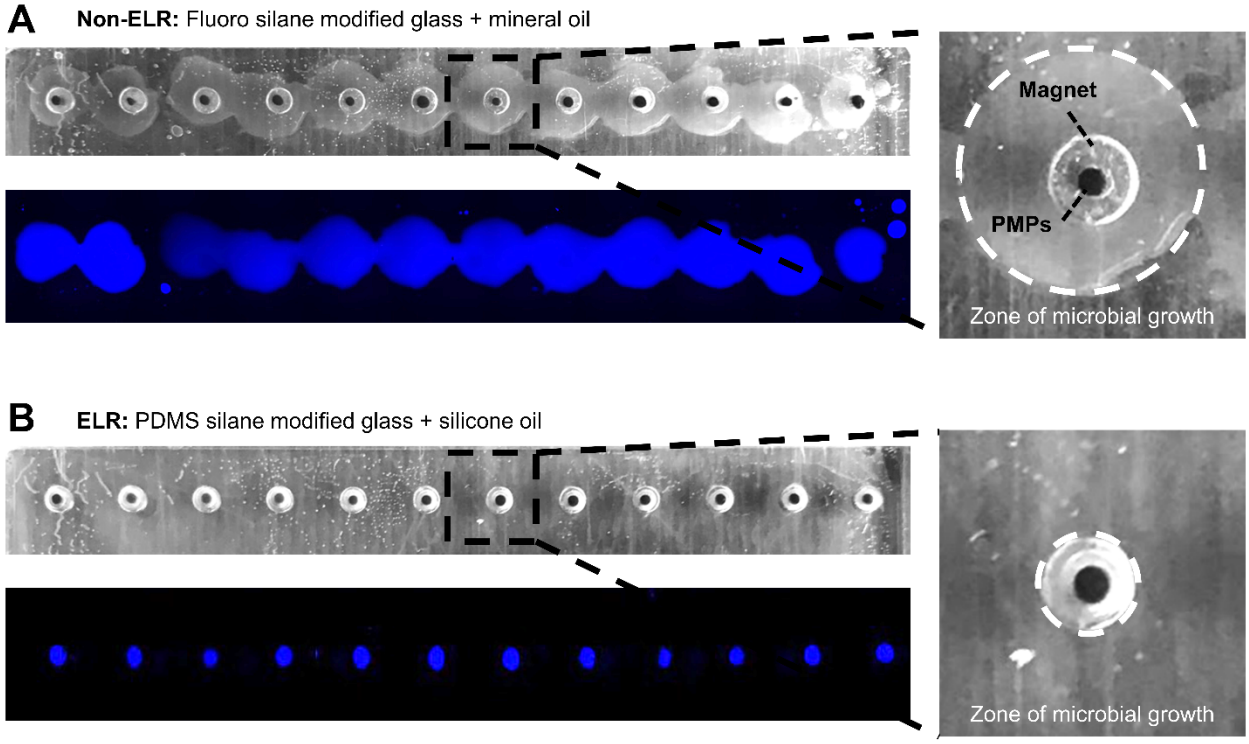

Figure 4.7: Bacterial growth-induced biofouling (droplet spreading) of non-ELR surface (fluoro silane modified glass with mineral oil) compared to no fouling/spreading observed on an ELR surface (PDMS silane modified glass with silicone oil) after a 24 h culture. Bacteria used: *P. aeruginosa* CFP (strain PA01).

Additionally, we were also successful in achieving an antibiotic dose response using this VRD setup (Figure 4.6B and 4.6C), suggesting both successful VRD recovery of the gentamicin antibiotics and culture of *P. aeruginosa* under silicone oil without surface biofouling. Also worth mentioning is that the silicone oil, in addition to providing ELR

properties which enables the VRD process, also greatly reduces liquid evaporation when working with small volumes of liquid over extended periods of time (we found that a 1 μL droplet can be kept under silicone oil for over a week at 37 °C).

4.4.5 Antibiotic sequential dosing of bacteria

After successfully showing both sequential reagent delivery and antibiotic dosing experiments without bacteria-induced biofouling in the VRD system, we then used the VRD system to test a simple biological question to illustrate the assay capabilities of the method: will a higher concentration of antibiotics delivered within a short period of time have the same effect as a lower concentration of antibiotics delivered over a longer period of time, provided the total cumulative dose of the antibiotic remains the same? To test this, we spotted a VRD device with gentamicin at 1X concentration (1 gentamicin spot + 4 blank vehicle spots), 1/3X concentration (3 gentamicin spots + 2 blank vehicle spots), and 1/5X concentration (5 gentamicin spots). After drying the antibiotic spots and filling the device with oil, 2 μL droplets containing *P. aeruginosa* CFP were introduced and sequentially dragged from 1 antibiotic spot to another to perform VRD (with 1 h interval between each VRD addition). After the 5 VRD additions, the droplets were allowed to incubate at room temperature for 24~48 h, then dragged onto a column of hydrophilic patterned spots for droplet immobilization and imaging as described above (Figure 4.8A). For comparison, we also performed a similar experiment in a macroscale 96-well plate. For the macroscale experiment, 100 μL of *P. aeruginosa* CFP bacterial suspension was added to a 96-well plate, followed by introduction of 1 μL gentamicin (to a final concentration of 1X, 1/3X, and 1/5X) or blank vehicle control at 1 h intervals for a total of

5 additions (Figure 4.8B). The plate was similarly incubated at room temperature for 24~48 h, and bacterial growth was measured via absorbance on a plate reader. Interestingly, although no significant difference in growth inhibition was observed for all 3 antibiotic addition conditions (1X dose at 0 h, 1/3X over 2 hours, and 1/5X over 4 hours) in the macroscale well-plate experiment (Figure 4.8B), we saw a significant reduction in antibiotic growth inhibition for the 1/5X dose over 4 hours condition with the VRD method, which only became apparent after a 48-h culture (Figure 4.8A). These results suggest that there are differences in bacterial growth dynamics in microscale droplets in the VRD method compared to a conventional macroscale well plate, which become more apparent under antibiotic stress, but may not show up under normal growth conditions (the control group in the VRD and well plate methods appear very similar as shown in Figure 4.8). Such differences in growth dynamics have also been previously documented for microscale vs. macroscale culture conditions, attributed to differences such as diffusion dynamics[78].

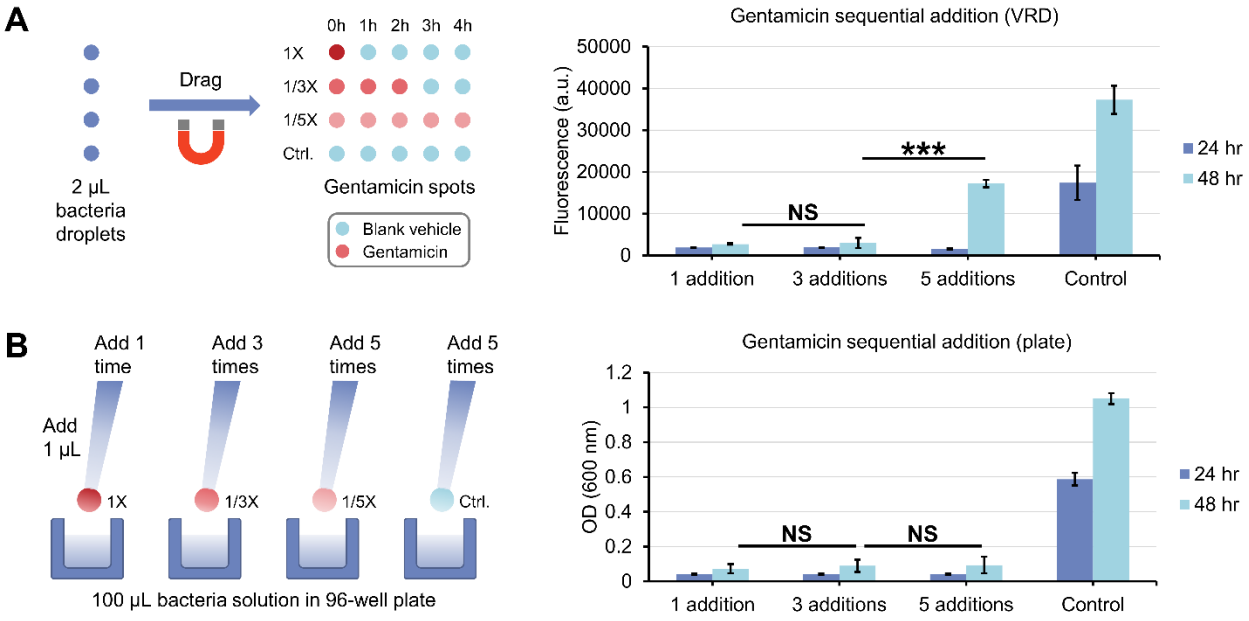

Figure 4.8: Sequential antibiotic dosing of bacteria using VRD compared to a conventional macroscale well plate format. (A) Workflow schematic (left) and results (right) for sequential antibiotic dosing of bacteria (*P. aeruginosa* CFP) using VRD. (B) Workflow schematic (left) and results (right) for sequential antibiotic dosing of bacteria (*P. aeruginosa* CFP) using a traditional 96-well plate workflow. Error bars denote the standard deviation from 3 technical replicates. Statistical significance as determined by Student's t-test is represented by *** $p \leq 0.001$, NS = not significant.

4.4.6 Recovery of complex enzyme assay mixtures using VRD

To test the ability of the VRD method in recovering more complex assay reagent mixtures, we attempted to recover a enzyme assay "kit": CellTiter-Glo (Promega), a luminescence-based enzyme assay reagent used for quantifying viable cells via measurement of cellular ATP, into droplets containing live mammalian cells. Although the exact composition of the reagent is a commercial secret, at a minimum it contains a mixture of luciferase enzyme, the enzyme substrate (luciferin), enzyme reaction buffer, salts, and potentially other additives. Success in performing this assay with the VRD system will require all the following to be accomplished: drying and recovery of all the essential ingredients in the CellTiter-Glo reagent via VRD, maintenance of luciferase enzyme activity following drying and reconstitution, successful lysis of cells via the recovered CellTiter-Glo reagent, successful reaction of the released cellular ATP with the enzyme assay reagents, and lastly, direct measurement of luminescence signal from the droplets in the device. We spotted CellTiter-Glo onto the VRD device and vacuum dried the reagent as described above, followed by placing a constriction channel insert (this version also contains a shallow "extraction channel" for removal of magnetic beads) onto the glass bottom of the VRD device (Figure 4.9A). The device was then filled with silicone oil, then added with 2

μL droplets of silica PMPs into column 1 wells of the device insert. Separately, 2 μL droplets containing 10000, 1000, 100, 10, and 0 LNCaP cells in RPMI cell media were added into column 2 wells of the device insert, and the dried CellTiter-Glo reagents reside within column 3 wells of the device insert. This device design allows the PMPs to be kept separate from the primary reaction droplet except during droplet actuation. To start the assay, the PMPs were magnetically extracted from column 1 wells into column 2 wells containing the LNCaP cell droplets. The LNCaP cell droplets were then magnetically transported via the PMPs from column 2 wells, through the constriction channels and into column 3 wells which contain the dried CellTiter-Glo reagent spots to perform VRD (Figure 4.9A). The cell droplets were then allowed to incubate for 10 min for cell lysis and the enzyme reaction to occur, followed by magnetically removing the PMPs from the reaction droplets to enable better luminescence measurements to be performed via a plate reader. Results show that we were able to achieve a highly linear luminescent signal as a function of input cell number (Figure 4.9B), suggesting that both the VRD recovery and the enzyme assay of CellTiter-Glo were successful.

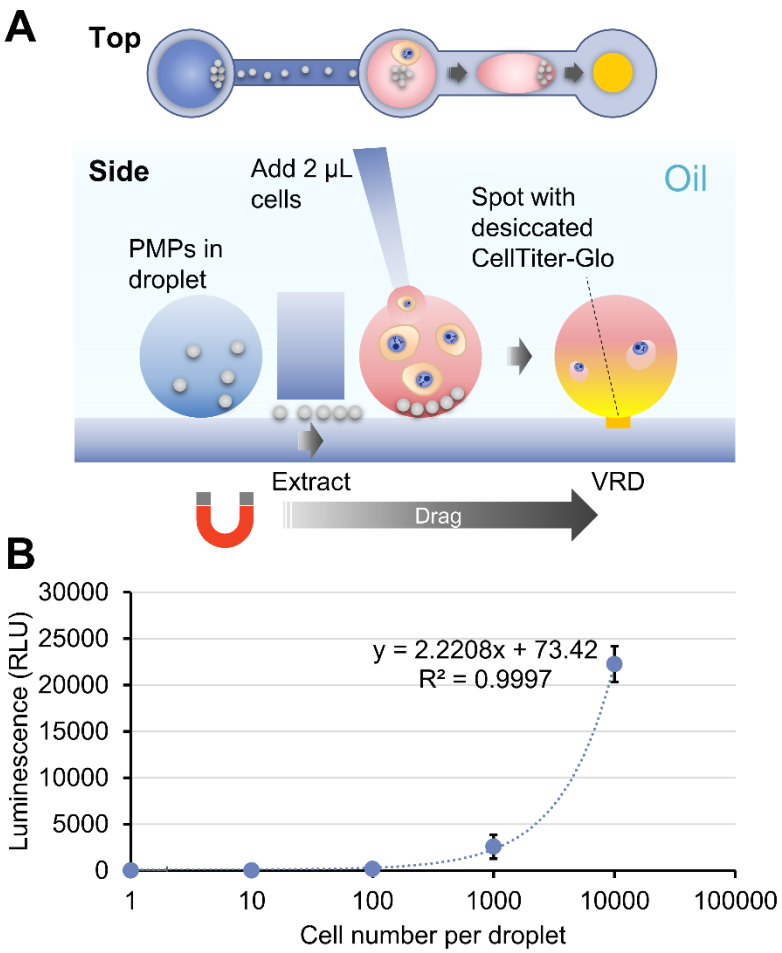

Figure 4.9: VRD of CellTiter-Glo into droplets containing LNCaP cells. (A) Schematic of device and operation process for performing VRD of CellTiter-Glo, an enzymatic assay reagent for quantifying viable cells via luminescence, into droplets containing LNCaP cell suspension. (B) Measured luminescence of droplets after VRD of CellTiter-Glo with the indicated number of input LNCaP cells. The luminescence of droplets is measured on a plate reader (PHERAstar FS, BMG Labtech). Error bars denote the standard deviation from 2 technical replicates.

4.5 Conclusions

Here we report a versatile and powerful reagent delivery method: VRD, for adding reagents to microscale aqueous droplets without increasing volume. VRD enables robust, near complete recovery of a wide range of biomolecule reagents, including sugars, proteins, DNA, and even complex enzyme assay mixtures. The liquid repellency afforded by the ELR 3-phase system also prevents device surface biofouling caused by protein molecules and biofilm forming bacteria, and the oil overlay enables assays involving long-term culture to be performed in microscale droplets without evaporation concerns. These combined advantages highlight the potential of VRD to be employed in a wide range of microscale, digital, and droplet-based bioassays.

However, due to the extremely high contact angle (~180º) achieved in the ELR system[25], we hypothesize that the VRD technique is likely not compatible with DMF droplet actuation methods which rely on electrowetting (EWOD)[50,51], owing to the lack of aqueous liquid wetting that occurs on the ELR surface, although we have yet to prove this. It will also be of interest to explore the compatibility of the VRD method with other DMF droplet actuation methods such as dielectrophoresis (DEP)[52,53] to allow for broader flexibility in integrating the technology with existing DMF systems.

Another consideration worth pointing out when designing assays with the VRD method is the presence of salts, buffers, or other additives in the deposited reagents. Because the volume of the droplet barely increases after each VRD addition, the osmolarity (i.e. concentration of salts, buffers, or other additives) in the reconstituted droplet will increase accordingly if the dried reagent spot contains these additives. As such, we recommend diluting the deposited reagents of interest in a salt/buffer free solution, or if this is not

possible, use a high concentration of reagent so that the additives will not constitute a significant percentage of the droplet after reconstitution. If either approach is not plausible, the change in solution osmolarity when performing a VRD addition may have to be taken into account when designing the assay.

4.6 Acknowledgements

This study was funded by the National Institutes of Health (NIH 1R01CA247479, NIH P30CA014520) and a UW Institute for Clinical and Translational Research pilot grant (NIH UL1TR002373).

Chapter 5

Centrifugation-assisted Immiscible Fluid Filtration (CIFF) for dual-bioanalyte extraction[1]

The extraction of bioanalytes is the first step in many diagnostic and analytical assays. However, most bioanalyte extraction methods require extensive dilution-based washing processes that are not only time consuming and laborious, but can also result in significant sample loss, limiting their applications in rare sample analyses. Here, we present a method that enables the efficient extraction of multiple different bioanalytes from rare samples (down to 10 cells) without washing—Centrifugation-assisted Immiscible Fluid Filtration (CIFF). CIFF utilizes centrifugal force to drive the movement of analyte-bound glass microbeads from an aqueous sample into an immiscible hydrophobic solution to perform an efficient, simple and non-dilutive extraction. The method can be performed using conventional PCR tubes with no requirement of specialized devices, or instruments, making it broadly accessible and cost effective. The CIFF process can effectively remove approx. 99.5% of the aqueous sample in one extraction with only 0.5% residual carryover, whereas a traditional “spin-down and aspirate” operation results in a higher 3.6% carryover. Another unique aspect of CIFF is its ability to perform two different solid-phase bioanalytes extractions simultaneously within a single vessel without fractionating the sample or performing serial extractions. Here we demonstrate efficient mRNA and DNA extraction from low input samples (down to 10 cells) with slightly higher to comparable recovery compared to a traditional column-based extraction technique, and the simultaneous extraction of two different proteins in the same tube using CIFF.

[1]This chapter has been modified from a published manuscript (*Anal. Chem.* 2019, 91, 18, 11848–11855). The manuscript includes as authors Duane S. Juang, Scott M. Berry, Chao Li, Joshua M. Lang, and David J. Beebe.

5.1 Preface

The prior chapters (chapters 2 and 3) all employ custom designed microfluidic devices for performing ESP-based analyte extractions. This chapter describes the development of an alternative method for performing ESP extractions which doesn't require any custom devices or specialized equipment: centrifugation-assisted Immiscible Fluid Filtration (CIFF). Instead of relying on magnet force to drive the movement of the solid phase capture bead, CIFF employs centrifugal force, and can be accomplished using conventional PCR tubes and a benchtop centrifuge, making the technology accessible to the vast majority of biomedical laboratories.

5.2 Introduction

Analyte extraction from a complex sample is the ubiquitous first step in most analytical bioassays[79]. The efficiency and recovery of the extraction process can often determine the success, limit of detection, and signal to noise ratio of the bioassay[80]. However, sample extraction is an often-overlooked aspect of bioassay development and could be a critical bottleneck for developing next generation bioassays for applications such as point-of-care diagnostics, as most traditional sample extraction technologies often require extensive liquid handling and washing steps and are not well optimized for processing rare amounts of analytes due to losses associated with the excessive number of liquid handling steps required[81-83]. Thus, advancements in sample extraction technologies will

have broad impact across multiple fields such as medical diagnostics and basic research to potentially enable “more data” to be gained per sample.

Although a wide variety of analyte extraction methods have been developed[79], they can generally be classified into two main approaches: liquid-phase extractions, and solid-phase extractions. Liquid-phase extractions, such as the classic acid guanidinium thiocyanate-phenol-chloroform extraction for nucleic acid extractions[84-86] utilize the differential partitioning and/or denaturation of proteins, lipids and other cellular debris into an organic phase, whereas nucleic acids of interest remain in the aqueous phase. The nucleic acids in the aqueous phase are then separated from the organic phase via centrifugation and can be further precipitated for additional purity. Liquid-phase approaches are generally reliable and yield high sample recovery[87], owing to the fact that they employ the intrinsic differential solubilities of different types of bioanalytes in aqueous vs. organic solvents. However, it is also time-consuming, requires toxic chemicals, and involves multiple pipetting and tube transfer steps that increase opportunities for sample contamination and mishandling. On the other hand, solid-phase extractions utilize the preferential binding of analytes to a solid support such as a surface-functionalized bead column[88-90] or paramagnetic particles (PMPs)[91,92]. In these platforms, target analytes bind to the solid support in an aqueous solution, whereas non-target biomolecules are eluted through or aspirated from the beads/column to remove contaminants. These approaches are more rapid and simple and do not require toxic organic solvents, as everything can be performed in aqueous solutions. Although results vary depending on the sample source, solid-phase extraction often comes with the tradeoff of lower analyte recovery[93-95], as it is potentially limited by several factors including the binding incidence and affinity

of the analyte to the solid support, removal efficiency of non-target contaminants which share the same aqueous phase as the target analyte, analyte loss during dilutive washing (to effectively remove contaminants), and elution efficiency for freeing the bound analyte from the solid support.

Previously, our group and others have developed a variety of improved solid-phase sample extraction technologies that our group refers to as exclusion-based sample preparation (ESP), which involves the movement of paramagnetic particles (PMPs) bound to an analyte of interest across an immiscible barrier (oil or air) to effectively "exclude" non-target contaminants from the biosample[17-20,32,33,96-100]. These technologies enable much faster processing and higher sample recovery compared to traditional PMP extraction techniques that typically involve multiple liquid aspiration and washing steps, which contribute to analyte loss due to prolonged processing, especially for low-binding affinity analytes[32]. The advantages and versatility of ESP technologies were also comprehensively demonstrated for the extraction of nucleic acids, proteins, and even rare cells[101]. One limitation of these approaches however, is that they generally require specially fabricated devices for immobilization of the immiscible phases via physical barriers and a PMP manipulation apparatus for performing parallel extractions, which could impede broad adoption and accessibility. In this study we report a new form of ESP technology that can be accomplished using common laboratory consumables (PCR tubes) and a benchtop centrifuge. Termed "Centrifugation-assisted Immiscible Fluid Filtration" (CIFF), it utilizes the differential density and hydrophilicity of aqueous, oil, and solid-phase capture beads for creating vertical liquid "barrier interfaces" that serve as an analyte exclusion filter under centrifugation. Its basic components comprise an aqueous

phase sample, underlaid with a dense oil phase, and an even denser solid-phase capture element (glass microbeads). The glass microbeads reside in the aqueous phase under normal conditions owing to their hydrophilicity, but are “extracted” to the oil phase under centrifugal force owing to their higher density. This technique combines some of the advantages of liquid-phase extractions that enable highly efficient exclusion of non-target analytes with the simplicity and efficiency of solid-phase extractions. Further expanding on this concept, we also demonstrated a simultaneous “dual-extraction” using CIFF by overlaying an additional hydrophobic phase that is lighter than the aqueous phase, paired with an even lighter hydrophilic solid phase (buoyant glass microbubbles), which under centrifugal force, are extracted upward to the top of the tube. As the extraction process in CIFF occurs in the vertical axis, this allows parallel extractions to be easily performed in multi-well PCR plates for large scale simultaneous multi-sample processing.

5.3 Materials and Methods

5.3.1 Operation of CIFF

The components of CIFF comprise a tube-shaped vessel of a hydrophobic material (here we used standard 0.2 mL polypropylene PCR tubes, Eppendorf), a fluorinated oil layer that is denser than the aqueous sample (FC-3283 fluorinated oil, d: 1.82 g/mL, 3M Inc.), and an even denser hydrophilic solid-phase capture element (glass microbeads, d: 2.48 g/mL, Polysciences Inc.), and the aqueous sample of interest (d~ 1 g/mL) (Figure 5.1). The additional benefit of using fluorinated oil is that it is highly inert and exhibits low solubility for both hydrophilic and lipophilic molecules (which account for nearly all

biomolecules). Thus, the CIFF process would effectively remove not only hydrophilic contaminants, but also hydrophobic contaminants such as lipids as well.

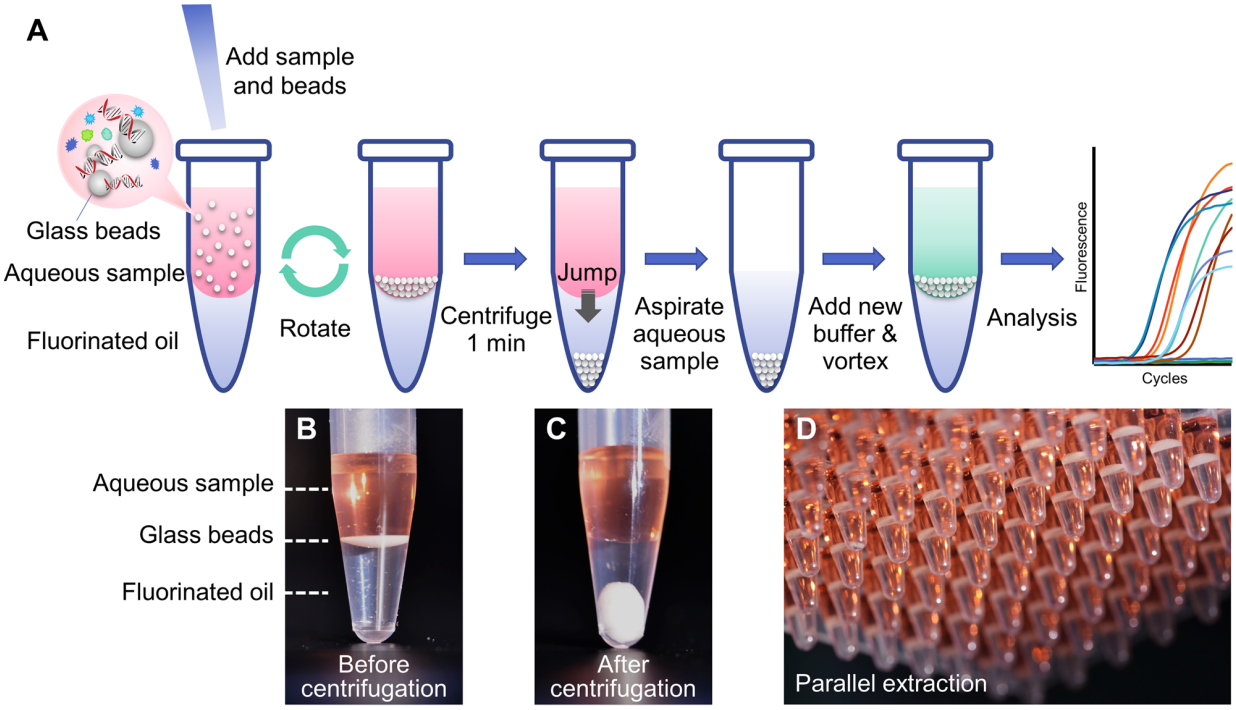

Figure 5.1: Principle of Centrifugation-assisted Immiscible Fluid Filtration (CIFF). (A) CIFF comprises of two immiscible liquid phases, an aqueous phase (d: 1 g/mL) and a hydrophobic phase that is denser than the aqueous phase (FC-3283 fluorinated oil, d: 1.82 g/mL) underlying the bottom of the aqueous sample. Functionalized glass microbeads (d: 2.48 g/mL) are mixed with the aqueous sample to bind analytes of interest, then loaded into a reservoir (here we used a 0.2 mL PCR tube for demonstration). Due to the hydrophilicity of the glass microbeads, they remain trapped inside the aqueous phase even after vigorous mixing (B). Under centrifugation however, the increased centrifugal force allows the glass microbeads to overcome the lipophobic resistance between the glass beads and oil phase and partition according to their density into the bottom oil phase, which effectively removes non-target molecules behind in the aqueous phase (C). (D) Parallel CIFF processes can be performed using conventional multi-well PCR plates.

To perform CIFF, 50 µL of fluorinated oil, 100 µL of aqueous sample, and 10 µL of glass microbeads (concentration 1 g/mL), are pipetted into a PCR tube. The high repellency of

the three phases ensures that proper phase separation will occur, even when pipetting vigorously. The tube was then centrifuged in a conventional benchtop centrifuge (Eppendorf Centrifuge 5424) at 10,000 *RCF* for 1 min to “jump” the dense glass microbeads downward into the bottom oil layer (10,000 *RCF* was used as it’s sufficiently higher than the minimum bead jump threshold determined in Figure 5.2B). After jumping, the dense glass microbeads can be collected directly from the bottom oil layer using a pipette. Alternatively, they can be left in the tube whereas the aqueous phase is aspirated and replaced with another aqueous solution of interest (wash buffer, elution buffer, etc.). The glass microbeads can then be easily re-suspended into the aqueous phase by tapping the tube for approx. 1 s on a conventional benchtop vortex, without residual beads left in the oil phase. (Note: to avoid bead contamination with the aqueous sample or premature bead resuspension, the tube should be kept upright after performing CIFF and not tilted to its side or inverted. If contamination still remains a concern, more fluorinated oil can be added to increase the distance between the bead pellet and aqueous phase). This enables multiple solution exchange/processing steps to be performed in the same tube with hardly any bead loss and cross contamination of aqueous solutions, as the fluorinated oil effectively seals off the beads from the aqueous solution after each CIFF operation. This allows us to easily perform binding, washing and elution steps in the same tube.

5.3.2 Quantification of bead residue

The quantity of residual beads left behind in the aqueous phase (i.e., beads that failed to traverse the aqueous/oil interface) after CIFF was quantified as follows: Glass

microbeads were functionalized with goat anti-mouse HRP (Invitrogen) as described below, a commonly-used enzyme that catalyzes the oxidation of a substrate (such as 3,3',5,5'-Tetramethylbenzidine, TMB), changing it from colorless to a blue-colored liquid in the process. The reaction can be stopped by adding 2N H_2SO_4 which changes the solution to a yellow-colored liquid that absorbs at OD 450 nm. Therefore, the number of residual beads, which is proportional to the amount of HRP enzyme present and hence to the absorbance of the TMB substrate, can be quantified. A normal CIFF process was performed in 100 µL DI water as described above, then 90 µL of the water was removed (leaving the residual beads) and added with 100 µL of TMB substrate (1-step ultra TMB-ELISA, Thermo Fisher Scientific), and incubated for 30 min at RT for color development. 50 µL of 2N H_2SO_4 was added to the tube to stop the reaction, then the liquid was transferred to a multi-well plate and the absorbance was scanned at 450 nm on an ELISA plate reader (Molecular Devices). A dilution curve was obtained by serially diluting HRP-conjugated glass microbeads and incubating with the same TMB substrate and stop solution. Carryover percentage was calculated by fitting the absorbance of the glass microbead reacted TMB substrate to the dilution curve.

5.3.3 Quantification of carryover

To quantitatively measure the amount of liquid carryover from the aqueous phase from CIFF, we prepared a solution of acridine orange at 500 µg/mL in deionized water and also deionized water containing 0.1% Triton X-100. In each experiment, 10 mg of glass beads (30-50 µm diameter, Polysciences Inc.) was added to a 0.2 mL PCR tube containing 100 µL of the acridine orange solution with or without Triton X-100 and underlaid with 50 µL

of FC-3283 fluorinated oil (3M Inc.). After centrifugation and CIFF, the glass beads were collected, resuspended in 100 µL deionized water, and spun down. The fluorescence intensity of the resuspended bead supernatant was measured using a NanoDrop 3300 fluorospectrometer (Thermo Fisher Scientific) at 530 nm, and the percent carryover was calculated by fitting the fluorescence intensity to a serially diluted calibration curve of acridine orange solution.

5.3.4 Oligo(dT) glass microbead surface functionalization

Functionalization of glass microbeads with oligo(dT) was performed as follows: 2 g of glass microbeads (30-50 µm) were placed in a 15 mL conical tube and washed with 10 mL of 1:1 methanol/HCl at RT for 30 min to remove potential organic contaminants on the bead surface. The beads were spun down and washed once with deionized water, followed by incubation with 5 mL of concentrated sulfuric acid to activate the glass microbead surface. The beads were then washed 3 times using deionized water and 3 more times using 99% ethanol, then incubated with 4 % (v/v) (3-mercaptopropyl)trimethoxysilane (Sigma-Aldrich) in 99% ethanol for 45 min at RT to change the surface functionality to a thiol moiety. After washing 3 times, the beads were incubated with N-γ-maleimidobutyryl-oxysuccinimide ester (GMBS, 0.25 mM in DMSO, Sigma-Aldrich), a heterobifunctional thiol to amine crosslinker for 30 min at RT, washed again for 3 times using ethanol and 3 times using PBS, then incubated with 10 µg/mL streptavidin in PBS for at least 1 hour at RT to covalently functionalize the glass microbeads with streptavidin. The streptavidin conjugated glass microbeads can be directly stored at 4 °C for a prolonged period of time before use. Oligo(dT) surface

functionality was introduced by incubating the glass microbeads in 1 nmol/mL biotinylated Oligo(dT) probe (Promega) for 30 min at RT. Before use in mRNA extraction, the microbeads were first washed in mRNA lysis/binding buffer (100 mM Tris-HCl (pH 7.5), 500 mM LiCl, 10 mM EDTA, 1% LiDS, 5 mM dithiothreitol (DTT)).

5.3.5 DNA extraction

DNA extraction using CIFF was performed as follows. In brief, cells in 20 µL of PBS was added 2 µL of Proteinase K and 20 µL of Buffer AL (Qiagen), vortexed for 15 s, then incubated at RT for 30 min to allow for complete cell lysis. 20 µL of 99% ethanol was then added to the tube and vortexed, followed by addition of 10 µL of washed unmodified glass microbeads (in Buffer AL) at a concentration of 1 g/mL, then rotated at RT for 3 min to capture the released DNA from cells onto the beads. After binding, the bead/aqueous mixture was transferred to a PCR tube containing 50 µL of FC-3283 fluorinated oil then centrifuged at 10,000 *RCF* for 1 min to perform CIFF. The aqueous sample was then aspirated out using a pipette leaving the fluorinated oil layer with beads. Washing (optional, for more complete removal of lysis buffer) was performed by adding 100 µL of washing Buffer AW1 (Qiagen) to the tube, vortexing briefly (approx. 1 s) to resuspend the beads back into the aqueous phase, and performing CIFF again by centrifuging at 10,000 *RCF* for 1 min. Buffer AW1 was then aspirated, and the washing process was repeated using Buffer AW2 (Qiagen). Buffer AW2 was then aspirated, and the DNA was eluted from the beads by adding in 100 µL of elution buffer (Buffer AE, Qiagen) to the tube and vortexing to resuspend the beads in the elution buffer. The beads were then removed by centrifuging them into the fluorinated oil phase, leaving the pure DNA eluent in the

aqueous phase, which can be completely recovered without bead contamination. For comparison, DNA extraction using a traditional column-based technique (Qiagen QIAamp DNA Mini Kit) was performed in accordance to manufacturer's protocols.

5.3.6 qPCR analysis of extracted DNA

Following DNA extraction, 5 µL of the 100 µL eluted DNA sample was mixed with 10 µL of SsoAdvanced Universal SYBR Green Supermix (Bio-Rad Laboratories), 3 µL of nuclease free water and 2 µL of primers for Long interspersed nuclear element-1 (LINE1, Forward primer: 5'-CGCAGAAGACGGGTGATTTC-3', Reverse primer: 5'-CCGTCACCCCTTTCTTTGAC-3', Integrated DNA Technologies) in a 96 well PCR plate and sealed with adhesive optically transparent PCR tape. The solution was pre-incubated for 5 min at 98 °C, then amplified for 50 cycles (98 °C for 30 s, 63 °C for 30 s, and 72 °C for 30 s) on a LightCycler 480 (Roche) real-time thermocycler. Threshold cycle (C_T) values were calculated using the built-in second derivative algorithm from the LightCycler 480 software.

5.3.7 mRNA extraction

THP-1 cells at various concentrations were lysed in 100 µL of lysis/binding buffer for 5 min at RT, then added to a PCR tube containing 50 µL of FC-3283 fluorinated oil. 10 µL of washed oligo(dT) functionalized glass microbeads at a concentration of 1 g/mL was added to the tube, then rocked at RT for 10 min to capture the released mRNA from cells onto the beads. After binding, the tubes were centrifuged at 10,000 *RCF* for 1 min to perform CIFF. The aqueous sample was then aspirated out using a pipette leaving the

fluorinated oil layer. A single wash (optional, for more complete removal of lysis buffer which could inhibit downstream PCR activity) was performed by adding 100 µL of RNA washing buffer (10 mM Tris-HCl (pH 7.5), 0.15 M LiCl, 1 mM EDTA) to the tube, vortexing briefly (approx. 1 s) to resuspend the beads back into the aqueous phase, and performing CIFF again by centrifuging at 10,000 *RCF* for 1 min. The wash buffer was then aspirated, and the mRNA was eluted from the beads by adding in 30 µL of elution buffer (10 mM Tris-HCl, pH 7.5) to the tube and vortexing to resuspend the beads in the elution buffer. The beads were then removed by centrifuging them into the fluorinated oil phase, so what remains in the aqueous phase is now pure mRNA eluent which can be completely recovered without bead contamination. As a comparison, mRNA extraction was also performed using matched samples with the same beads and reagents (except without the fluorinated oil), and were washed three times using a conventional “wash, spin-down, aspirate” method inside a 0.2 mL PCR tube instead of doing CIFF.

5.3.8 RT-qPCR analysis of extracted mRNA

After extraction, 10 µL of the 30 µL eluted mRNA samples were mixed with 10 µL 2X RT buffer and 1 µL of 20X RT enzyme from a reverse transcription kit (High Capacity RNA-to-cDNA Kit, Thermo Fisher Scientific) in an 8-well 0.2 mL PCR strip tube (USA Scientific) and reverse transcribed at 37 °C for 1 h followed by heating to 95 °C for 5 min on a thermocycler (Techne, TC-412), as per the manufacturer’s recommendations. 2.5 µL of the converted cDNA was mixed with 5 µL of LightCycler 480 Probes Master (Roche), 2 µL of nuclease free water and 0.5 µL of manufacturer preformulated primer-hydrolysis probe (FAM/MGB) mix for Human large ribosomal protein (RPLP0, Applied Biosystems,

catalog no. 4333761) in a 96 well PCR plate (dot scientific, USA) and sealed with adhesive optically transparent PCR tape. The solution was pre-incubated for 10 min at 95 °C, then amplified for 45 cycles (95 °C for 10 s, 60 °C for 30 s, and 72 °C for 1 s) on a LightCycler 480 (Roche) real-time thermocycler. Threshold cycle (C_T) values were calculated using the built-in second derivative algorithm from the LightCycler 480 software.

5.3.9 Glass microbead and microbubble protein functionalization

Functionalization of glass microbeads and microbubbles with antibodies was performed using a previously reported protocol[102]. In brief, S38 XHS glass microbubbles and glass microbeads were placed in a 15 mL conical tube and washed with 10 mL of 1:1 methanol/HCl at RT for 30 min to remove potential organic contaminants on the bead surface. The beads were spun down then washed 3 times using deionized water and 3 more times using 99% ethanol, then incubated with 10% (v/v) (3-Aminopropyl)triethoxysilane (Sigma-Aldrich) in 99% ethanol for 60 min at RT to functionalize the glass surface with amine groups. The beads/bubbles were washed with ethanol three times, then incubated with 2.5% (v/v) glutaraldehyde in PBS for 1 hour at RT. This was followed by washing three times with PBS, and incubation with proteins of interest (mouse IgG and rabbit IgG isotype control antibodies, Invitrogen, and goat anti-mouse HRP, Invitrogen) to covalently attach the proteins to the bead surface. The bead surface was blocked with 1% BSA in PBS to reduce non-specific binding.

5.3.10 Dual-CIFF

Dual simultaneous bead-based extractions are a unique property enabled by CIFF. Operation of dual-CIFF is similar to single CIFF except that an additional buoyant hydrophilic solid phase (S38 XHS glass microbubbles, d: 0.38 g/mL, 3M Inc.) was added to the aqueous phase and overlaid with an additional lighter hydrophobic phase (silicone oil, d: 0.91 g/mL, Sigma-Aldrich) (Figure 5.6). 50 µL of FC-3283 fluorinated oil, 100 µL of aqueous sample with glass microbeads and glass microbubbles, and up to 100 µL of silicone oil were added to a 0.2 mL PCR tube. The dual-CIFF system was then centrifuged in a conventional benchtop centrifuge (Eppendorf Centrifuge 5424) at 10,000 *RCF* for 1 min to “jump” the dense glass microbeads downward or glass microbubbles upward into their respective top or bottom oil layers. After centrifugation, the top glass microbubbles can be collected using a large-orifice pipette tip (Fisher scientific) together with the silicone oil, whereas the dense glass microbeads can be collected directly from the bottom using a pipette or as described previously, left in the tube whereas the aqueous phase is removed.

5.4 Results and Discussion

5.4.1 Operational theory

The physics underlying the operational principle of CIFF is governed by a competing balance between gravitational inertial forces with lipophobic resistance between the glass beads and the fluorinated oil phase. In brief, successful “jumping” of glass beads into the hydrophobic phase occurs when the gravitational force applied to the glass bead aggregate is higher than the lipophobic resistance keeping them from entering the oil

phase. This is governed by multiple variables including relative centrifugal force *RCF* (a dimensionless unit defined as a multiple of gravitational acceleration at the Earth's surface), mass of the bead cluster (M_{beads}), radius of the tube (r_{tube}), radius of the beads (r_{bead}), as well as the interfacial tension of the glass beads with oil and hydrophilicity of the bead surface (Figure 5.8). A more detailed derivation of the theory governing this phenomenon is included at the end of this chapter (Supplementary Information), but here we present a simplified version based on the following assumptions: the beads spread across the full diameter of the tube (typically observed in our experiments), the thickness of the glass bead cluster is constant across the whole tube, the interfacial tension between the glass beads and oil phase is constant, the hydrophilicity, density, and size of the bead is constant, and beads are packed uniformly and tightly across the entirety of the tube. From these approximations we estimate that the required relative centrifugal force *RCF* for a given mass of beads (M_{beads}) in milligrams is:

$$RCF \approx C/M_{beads}$$

Where C is a constant estimated to be ≈ 12000 · mg for the described CIFF system.

By plugging in this value, we obtain the blue solid curve in Figure 5.2B which shows the same relative relationship of $RCF \approx C/M_{beads}$ as the obtained experimental values (green circular dots, which translate to an estimated C of ≈ 30000 · mg). We believe the discrepancy between the predicted curve and the experimental data is due to difficulties in accurately estimating constant C from the above listed assumptions (see detailed discussion at the end of the chapter).

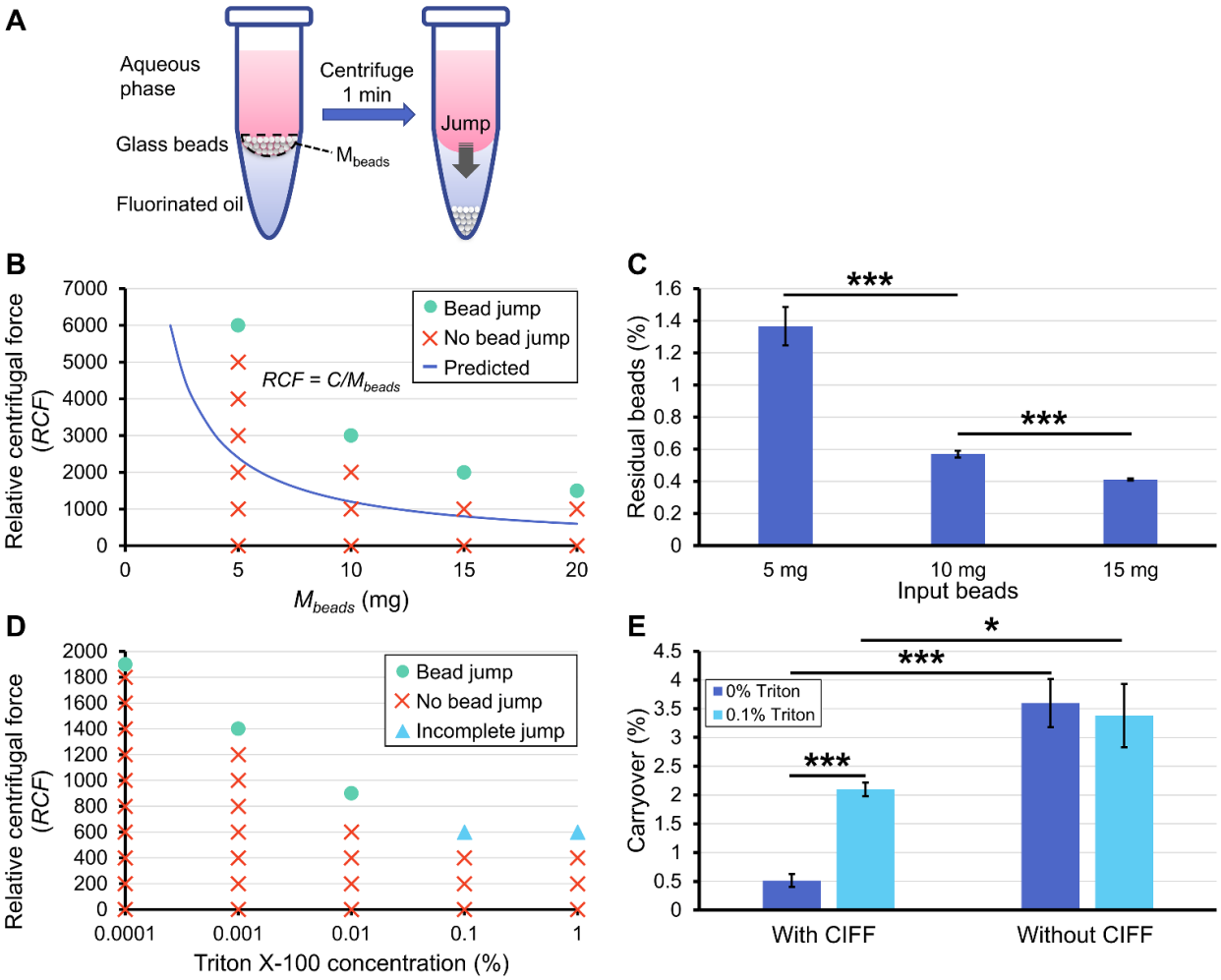

Figure 5.2: Characterization of CIFF. (A) Schematic of the CIFF process. (B) Relation of centrifugal force and amount of glass beads to the "jumping" of beads in CIFF. The smaller the amounts of added beads, the higher the centrifugal force required for the beads to overcome the resistance from jumping into the oil phase. (C) Percentage of residual glass microbeads (relative to input) left in the aqueous phase after performing CIFF for different amounts of input beads. Beads were all spun at 10,000 RCF for this measurement. (D) Relation of centrifugal force and Triton X-100 concentration in the aqueous phase to the "jumping" of 10 mg beads in the CIFF process. (E) Percentage of aqueous phase carryover of 10 mg beads after performing CIFF with or without 0.1% Triton X-100 in the aqueous phase. This was compared to a traditional "spin down beads, aspirate supernatant, and resuspend" approach (without CIFF). Error bars denote the standard deviation from 3 technical replicates. Statistical significance as determined by Student's t-test is represented by * $p \leq 0.05$, ** $p \leq 0.01$ and *** $p \leq 0.001$.

5.4.2 Characterization of CIFF

To determine the threshold centrifugal force required to perform the “jumping” of glass microbeads into the fluorinated oil phase for a given number of beads, we screened four bead amounts ranging from 5 mg to 20 mg per 0.2 mL PCR tube for their respective threshold “jumping” centrifugal force. Results show that the threshold centrifugal force for successful jumping of beads from the aqueous to the fluorinated oil phase is inversely correlated with the number of beads, with 5 mg beads requiring up to 6000 *RCF* of force to traverse the oil/aqueous liquid barrier but 20 mg of beads requiring only approx. 1500 *RCF* of force (Figure 5.2B). However, although the amount of residual beads after CIFF is similar regardless of input (approx. 0.06 mg), the percentage of residual beads relative to input is significantly higher using 5 mg of beads (Figure 5.2C), thus 10 mg of beads was chosen for its lower residual bead amount (which would result in higher recovery) and lower centrifugal force threshold for successful jumping of beads.

As Triton X-100 is a common surfactant known to decrease the interfacial tension between oil and aqueous interfaces[103,104], we also tested whether addition of Triton X-100 might reduce the required centrifugal force during CIFF. Results show that the concentration of Triton X-100 in the aqueous phase (ranging from 0.0001% to 1%) is indeed inversely correlated with the threshold centrifugal force required for jumping the beads, although at higher concentrations of Triton X-100 (0.1% and 1%), it also resulted in the formation of emulsions and incomplete bead jump (Figure 5.2D, blue triangles). The addition of Triton X-100 also resulted in a higher amount of aqueous sample carryover as revealed by acridine orange quantification (Figure 5.2E), which is likely caused by the lowered interfacial tension resulting in reduced filtration efficiency when

the beads traverse the aqueous/oil barrier. Worth noting though, is that the CIFF process successfully removes approx. 99.5% of the aqueous sample in one operation with only 0.5% residual carryover, whereas a traditional “spin-down and aspirate” operation results in a much higher 3.6% carryover (Figure 5.2E). We acknowledge that other physical parameters may also affect the “jumping” and purification efficiency of the CIFF process (bead density, bead surface hydrophobicity, oil density, oil hydrophobicity, etc.), but these parameters are not easily varied in practice as they’re intrinsic properties to the material itself (glass and fluorinated oil) and hence were not explored in this study.

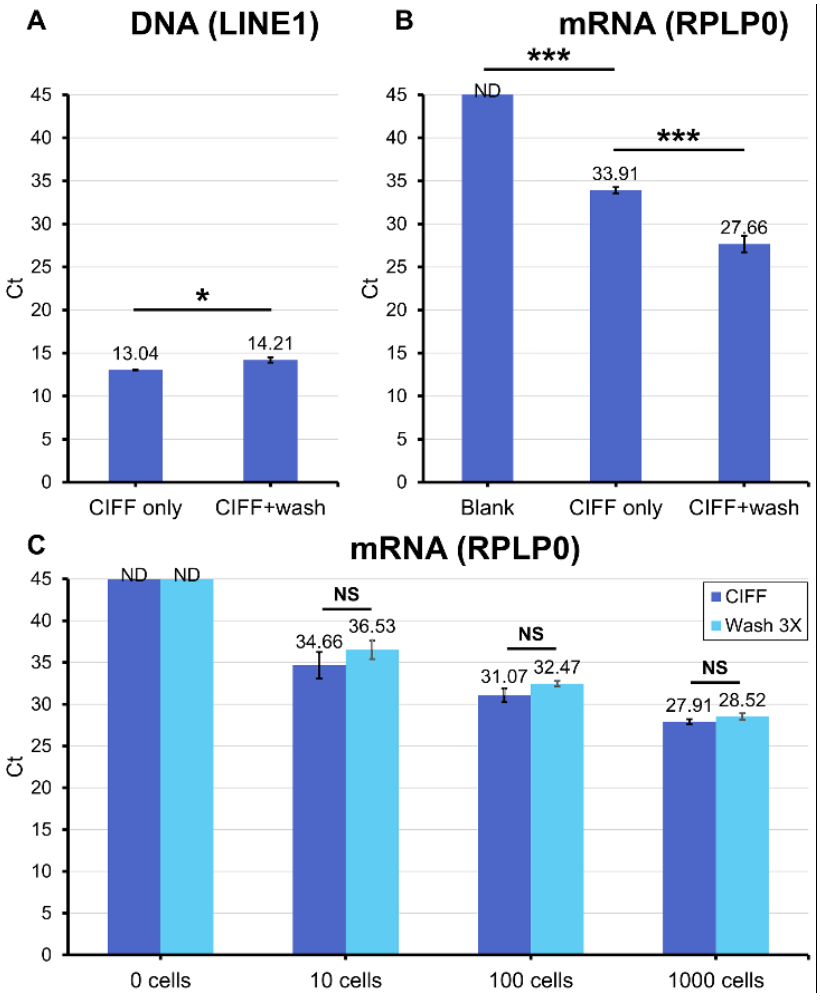

Figure 5.3: DNA and RNA extraction performance in CIFF. (A) qPCR performance of LINE1 DNA extracted using CIFF only, compared to CIFF plus two additional washes with buffer AW1 and

AW2 (Qiagen). (B) RT-qPCR performance of RPLP0 mRNA extracted using CIFF only, compared to CIFF plus one single wash with RNA washing buffer. The RNA sample was not diluted prior to RT-qPCR, thus one extra wash was necessary to further remove residual lysis/binding buffer contamination which causes inhibition of RT-qPCR (see Figure 5.5). (C) mRNA extraction performance of CIFF with one single wash compared to a conventional manual 3-wash operation. ND: Not detected. Error bars denote the standard deviation from 2 technical replicates. Statistical significance as determined by Student's t-test is represented by * $p \leq 0.05$, ** $p \leq 0.01$ and *** $p \leq 0.001$, NS = not significant.

5.4.3 DNA extraction

After showing that CIFF extraction can successfully remove approx. 99.5% of liquid from a 100 µL aqueous sample, we next attempted to perform DNA extraction using CIFF. DNA is known to bind to the surface of silica/glass under high chaotropic salt (such as guanidine hydrochloride or guanidine thiocyanate) concentrations, and elute under low salt conditions, which is the principle of most column and bead-based DNA extraction methods. Here we employed unmodified glass beads paired with a lysis buffer containing guanidinium salts (Buffer AL, Qiagen) for performing CIFF DNA extraction and compared extraction efficiency with or without washing. DNA extraction yield was quantified using qPCR with primers directed against LINE1 (Long interspersed nuclear element-1). Starting with 100,000 THP-1 cells, we showed that CIFF can efficiently extract DNA from cells without washing, followed by subsequent qPCR detection. Results from the qPCR for showed that CIFF yielded better recovery (lower Ct values) for the same amount of input sample without washing compared to CIFF with washing using standard DNA column washing buffers (Buffer AW1 and AW2, Qiagen) (Figure 5.3A). We also showed that CIFF can successfully extract DNA from low input samples (10 to 10,000 LNCaP cells) with comparable to slightly higher recovery compared to a traditional column-based

technique (Qiagen QIAamp DNA Mini Kit) as determined by qPCR (Figure 5.4). Although no washing yielded better results in this application, additional washing could be employed for samples containing excess amounts of PCR inhibitors or when the eluted DNA must be highly concentrated (small elution volume).

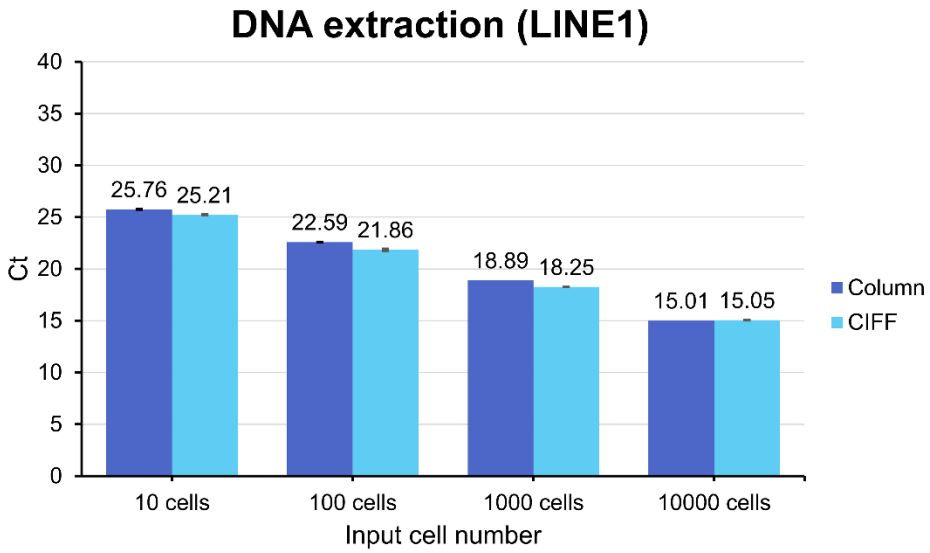

Figure 5.4: DNA extraction efficiency of CIFF compared to a traditional column-based technique for low input samples. qPCR performance of LINE1 DNA extracted from 10 to 10,000 LNCaP cells using CIFF compared to a traditional column-based technique (Qiagen QIAamp DNA Mini Kit).

5.4.4 mRNA extraction

In addition to DNA extraction, we also attempted mRNA extraction using this method, as mRNA extraction is one of the most commonly practiced extractions in biology labs. mRNA extraction efficiency of CIFF was quantified using a housekeeping gene primer RPLP0 (ribosomal protein lateral stalk subunit P0). We initially attempted to perform qPCR directly from a single CIFF extracted sample without any washing, but results showed that PCR threshold cycle (C_T) values were higher (meaning less PCR efficiency) for the single-CIFF extracted sample without washing, compared to two sequential CIFF

extractions with a single wash in between, suggesting that the tiny residual carryover from the aqueous phase (which contain the strongly protein denaturing 1% lithium dodecyl sulfate (LiDS)) could inhibit the downstream PCR reaction (Figure 5.3B). To investigate this possibility, we performed a lysis/binding buffer spike-in contamination experiment for RT and qPCR reactions and found slight inhibition to occur with as low as 0.078% Lysis/Binding buffer contamination for RT reactions, gradual inhibition all the way to 0.625%, and complete inhibition starting at 1.25%. For qPCR, we did not observe significant inhibition all the way to 0.313%, but complete inhibition starting at 0.625% (Figure 5.5).

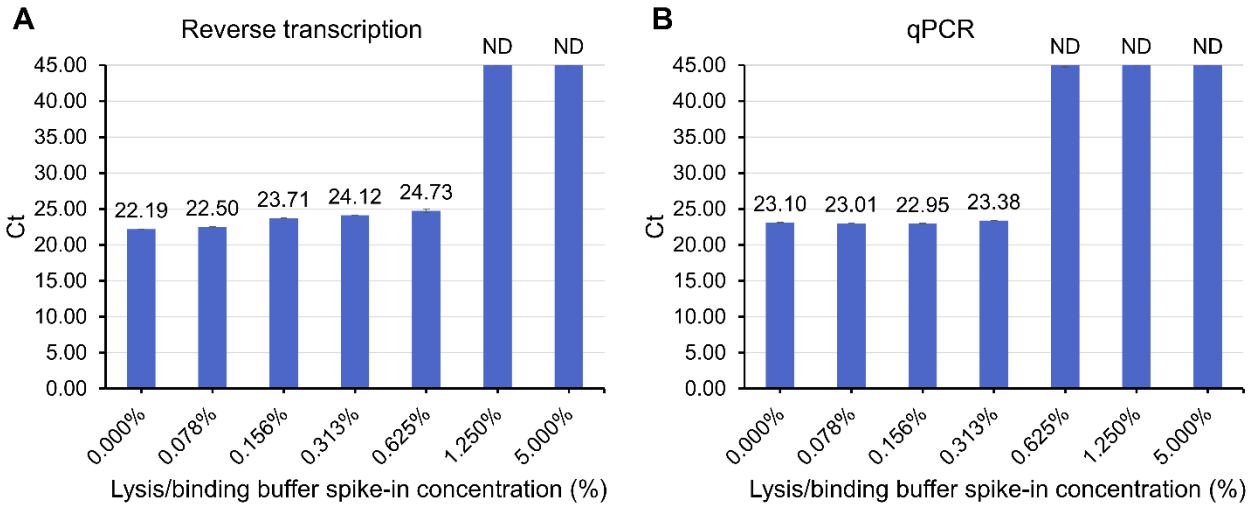

Figure 5.5: Inhibition of reverse transcription (A) and quantitative PCR (B) reactions at various concentrations of mRNA Lysis/Binding buffer (100 mM Tris-HCl (pH 7.5), 500 mM LiCl, 10 mM EDTA, 1% LiDS, 5 mM dithiothreitol (DTT)) contamination in the reaction.

Judging from this data, the 0.5% carryover in CIFF would indeed result in inhibition of both RT and qPCR for undiluted samples, thus necessitating the one additional wash step if maximum sensitivity is desired. Thus, we performed subsequent RT-qPCR assays by two sequential CIFF operations with a single wash in between to further effectively

remove contaminating lysis/binding buffer. Worth noting however, is that we were aiming for maximum sensitivity with the RT-qPCR analysis (down to 10 cells), so the eluted mRNA sample was not diluted prior to use and hence the concentration of the lysis buffer carryover would be higher in the final reaction. With larger samples, dilution of mRNA can be performed to omit the additional wash. We also showed that the CIFF process yields mRNA recovery rates at least comparable or slightly better (lower C_T values) compared to a traditional 3X “wash, spin-down, aspirate” operation using the same matched glass microbeads and samples (Figure 5.3C). This suggests that the non-dilutive extraction and fewer washing operations of CIFF provide an advantage in sample recovery and operational speed compared to traditional washing-based extraction techniques.

5.4.5 Simultaneous dual-CIFF

Although paramagnetic particles are an immensely powerful and versatile tool for performing analyte extractions and have proven to be faster and more affordable than fluorescence labeling-based techniques for performing cell separations (fluorescence-activated cell sorting), it lags behind optical based techniques in one critical aspect: there is only one “flavor” of magnetic force, which means only one target extraction can be performed at one time whereas the multiple different wavelengths of fluorescence dyes and colors affords multi-biomarker labeling and sorting simultaneously. One unique aspect of the CIFF method however, is that although gravitational force also only has one “flavor”, it pulls more strongly on objects with greater mass and density compared to lighter objects. This allows for movement of matter with different densities in two opposite directions in a liquid (sinking or floating) under a single force field (gravitational pull).

Harnessing this property, we demonstrated that CIFF can simultaneously extract two analytes of interest from the same sample in opposite directions by harnessing the differential densities (in the order of decreasing density) of glass microbeads, fluorinated oil, aqueous liquid, silicone oil, and glass microbubbles. While microbubbles are hollow[102,105] (i.e. density lower than water) and microbeads are solid (i.e. density higher than water), both share the same surface chemical properties of soda-lime-borosilicate glass and are equally suitable for chemical modifications. Under centrifugation, glass microbeads extract to the bottom of the tube under centrifugation, whereas glass microbubbles float to the very top of the tube via buoyancy. As a proof of concept, glass microbeads and glass microbubbles were respectively conjugated with rabbit IgG and mouse IgG isotype control antibodies for capturing different targets. They were then incubated with a mixed solution containing Alexa Fluor 488 anti-rabbit IgG and Alexa Fluor 647 anti-mouse IgG, then simultaneously extracted using dual-CIFF.

After extraction, the beads and bubbles were taken out using a pipette and respectively imaged on an epifluorescence microscope (Nikon Ti Eclipse) at 485/525 nm (Excitation/Emission) and 648/684 nm. Results from the overlaid fluorescence images show that the CIFF process was able to highly effectively extract the proteins of interest from the aqueous sample without significant carryover or cross-contamination of the two bead types, resulting in a very clean fluorescence signal for both beads (Figure 5.6).

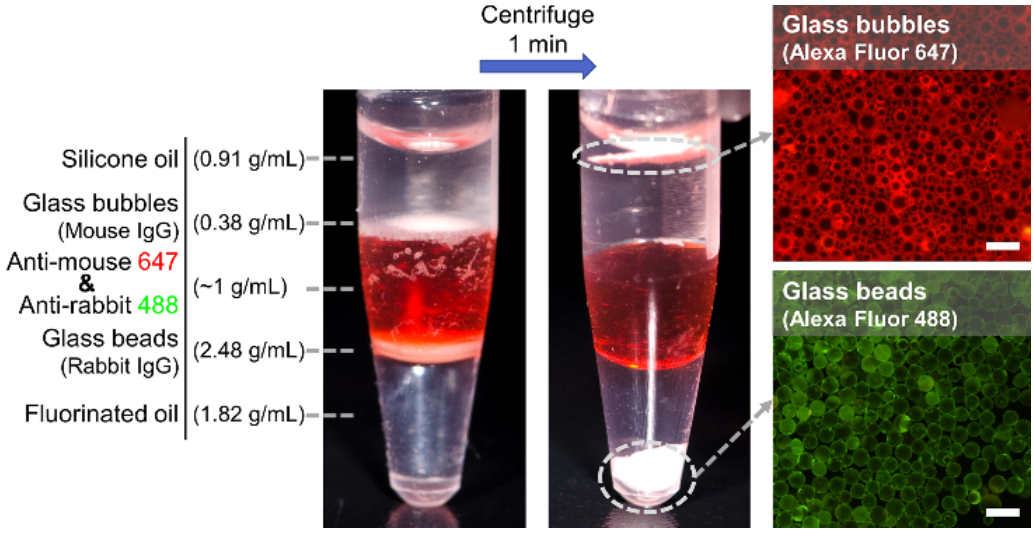

Figure 5.6: Simultaneous extraction of two different proteins (Alexa Fluor 647 anti-mouse IgG and Alexa Fluor 488 anti-rabbit IgG) from the same aqueous phase using dual-CIFF. The differential densities of mouse IgG-conjugated glass microbubbles and rabbit IgG-conjugated glass microbeads allow them to travel in opposite directions (floating vs. sinking) under centrifugation and simultaneously extract different target analytes to their respective top and bottom oil layers. Scale bar: 100 μm.

5.5 Conclusions

To summarize, we have demonstrated a simple and efficient sample extraction method termed CIFF for performing solid-phase analyte extractions with better contaminant removal, comparable or better sample recovery than conventional washing, and much fewer operating steps (Figure 5.7).

CIFF is compatible with a broad range of solid-phase analyte extractions as long as the analyte resides in an aqueous phase (such as DNA, RNA and proteins) or solvent that is of a different density and is immiscible with the oil phase. It does not require specialized equipment, is very cost effective, and is amenable to parallel processing. CIFF is also unique in its ability to perform two different solid-phase bioanalyte extractions

simultaneously within a single vessel, which cuts back on required processing time, especially for analytes that require prolonged incubation. It would be of interest to further expand this concept for performing simultaneous analyte extractions in future bioassay development to enable more information to be garnered per sample. In addition, we believe that the physical properties of CIFF make it intrinsically well suited for performing rare sample extractions due to its low sample volume, efficient processing, and very few washing steps. The relatively low sample volume and low requirement of washing in CIFF could enable better sample recovery and downstream analysis efficiency. Despite its advantages, we acknowledge that the CIFF technique has a few drawbacks. One is the requirement of a benchtop centrifuge to perform the process, which limits the technology's use in resource-poor settings with limited access to electricity. Another is the use of fluorinated oils in the process, which are known to have high recalcitrance to degradation leading to long environmental persistence[106], although the inert properties of fluorinated oils could potentially allow it to be recycled and reused after the extraction process, reducing environmental impact.

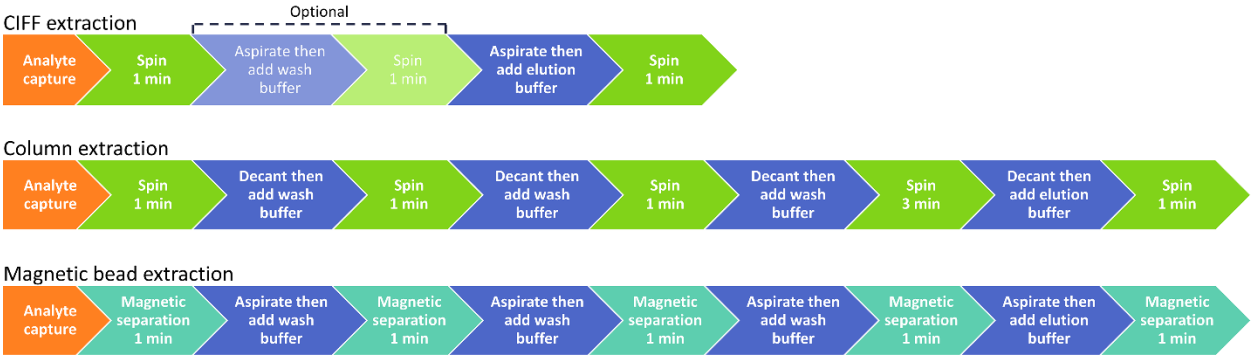

Figure 5.7: Comparison of operation workflow of CIFF extraction, column-based extraction, and magnetic bead-based extraction.

5.6 Supplementary Information

Derivation of the physics governing bead jump in CIFF.

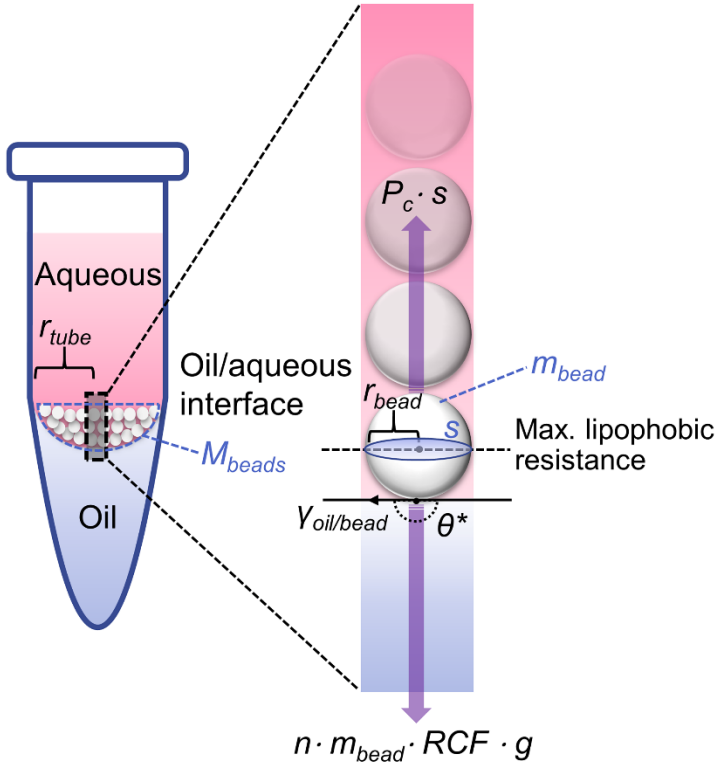

Figure 5.8: Physical variables governing bead jump in CIFF.

The physics governing the conditions of bead jump in CIFF can be written as:

$$n \cdot m_{bead} \cdot RCF \cdot g = P_c \cdot s$$

(equation 1)

where n is the stacking coefficient estimated as $N_{total}/N_{per\ layer}$ on average, N_{total} is the total number of beads in the tube, $N_{per\ layer}$ is the number of beads in the largest circle in the bead pellet, which is $N_{per\ layer} = (r_{tube}/r_{bead})^2$, where r_{tube} is the radius of the centrifugal tube, and r_{bead} is the radius of a bead. m_{bead} is the mass of a single bead, RCF is the relative

centrifugal force (a dimensionless unit defined as the ratio of centrifugal acceleration over gravitational acceleration (g) at the Earth's surface), s is the projected area of a single bead at the oil/aqueous interface equal to πr_{bead}^2, P_c is the capillary pressure (lipophobic resistance) applied on a single bead from the oil phase which is equal to $2\gamma_{oil/bead} \cdot cos\theta/r_{bead}$. $\theta = \pi - \theta^*$ and θ^* is Young's contact angle of the fluorinated oil (FC-3283) on the bead (*i.e.*, glass) surface under water estimated from our previous work,[1] and $\gamma_{oil/bead}$ is the oil-bead interfacial tension.

$$\frac{N_{total}}{N_{per\ layer}} \cdot m_{bead} \cdot RCF \cdot g = 2\frac{\gamma_{oil/bead} \cdot cos\theta}{r_{bead}} \cdot \pi r_{bead}^2$$

(equation 2)

$$\left(\frac{N_{total}}{(r_{tube}/r_{bead})^2}\right) \cdot m_{bead} \cdot RCF \cdot g = 2\frac{\gamma_{oil/bead} \cdot cos\theta}{r_{bead}} \cdot \pi r_{bead}^2$$

(equation 3)

Here we define $M_{beads} = N_{total} \cdot m_{bead}$

$$M_{beads} \cdot RCF = 2\frac{\gamma_{oil/bead} \cdot cos\theta}{r_{bead}} \cdot \pi r_{bead}^2 \cdot (r_{tube}/r_{bead})^2 / g \approx 12000 \cdot \text{mg}$$

(equation 4)

Solving for *equation 4* using constants that represent the actual values or measured values from a previous work,[1] including r_{tube} = 2500 μm, r_{bead} = 20 μm, $\gamma_{oil/bead}$ = 59.0 mN/m,[1] θ^* = 180°, and g = 9.807 m/s^2, gives

$$RCF \approx 12000/M_{beads}$$

(equation 5)

By plotting *equation 5* with M_{beads} as the *x* axis and *RCF* as the *y* axis yields the predicted curve shown in Figure 5.2 of the main text.

Thus, for a given oil/aqueous pair, physical characteristics of bead and centrifugal tube, more beads are added to the tube would result in a larger M_{beads}, and hence a smaller centrifugal force (or *RCF*) would be needed to cause the jumping of beads. It is worth noting that a variance of *n* (the stacking coefficient) across the oil/aqueous meniscus (*i.e.*, larger towards the center and smaller towards the edge) will be seen, especially in cases of smaller M_{beads}. The smaller the *n*, the higher the required *RCF*. In our prediction (*equation 1*), *n* is estimated as an average across the bead pellet, so the predicted RCF is actually smaller than the measured value and the discrepancy between prediction and experiment becomes more noticeable when M_{beads} becomes smaller (Figure 5.2B). This also explains the trend seen in Figure 5.2C where smaller M_{beads} values are associated with a higher percentage of residual beads.

As can be seen in *equation 4*, a more hydrophilic (or lipophobic) surface of beads would result in a larger $\gamma_{oil/bead}$ and thus an increased resistance retaining the beads in the aqueous phase. On the other hand, a smaller $\gamma_{oil/bead}$ which can be achieved for example by adding surfactant to the aqueous phase will allow the jumping of beads to occur much more easily. Similarly, if a tube with a smaller r_{tube} is used, for a given M_{beads}, a smaller centrifugal force (or *RCF*) for bead jump can be expected.

5.7 Acknowledgements

This work is funded by University of Wisconsin Carbone Cancer Center Support Grant P30 CA014520, NIH R01 EB010039 BRG, NIH R01 CA185251, NIH R01 CA186134, NIH R01 CA181648.

Chapter 6

Microbial Community Fitness Landscapes on a Chip[1]

Multispecies microbial communities underlie nearly all microbial ecosystems. Microbe-microbe interactions within the community can affect the survival fitness for individual members and the community as a whole. However, the prohibitively high number of possible interactions within a microbial community has made the characterization of these drivers of community development challenging, especially when using conventional microbial co-culture techniques. Here we report a “microbial community fitness landscape” (μCFL) platform to advance the systematic study of microbial community interactions. The μCFL creates a combinatorial microbial landscape made up of an array of triangular “fitness zones”, each zone comprising a 3-member “tester” microbial community in co-culture with a “target” microbial reporter. The μCFL enables the co-culture of multiple interacting microbial members at the same time but limits the interrogation of interactions to a “localized limited parameter space”, allowing for individual species-level resolution while also providing a more holistic community-level insight. The geometrical design of the μCFL allows complex 3-factorial microbial co-culture experiments to be performed with high combinatorial throughput and simplicity in readout. Using the μCFL we systematically screened a rhizosphere co-isolate community in co-culture with *Bacillus cereus* as a model target strain and identified 3-member communities which increased or decreased the fitness of *Bacillus cereus* in co-culture.

[1]This chapter has been modified from a manuscript in preparation. The manuscript includes as authors Duane S. Juang, Will E. Wightman, Gabriel L. Lozano, Layla J. Barkal, Jiaquan Yu, Manuel F. Garavito, Amanda Hurley, Ophelia S. Venturelli, Jo Handelsman, and David J. Beebe.

6.1 Preface

While the prior chapters were primarily focused on the development of sample preparation and analysis technologies, this chapter describes the development of a different form of assay: functional assays, for studying microbial community interactions. Microbes commonly reside within complex multi-species communities in nature, such as the human gut microbiome. Recent advances in high-throughput metagenomic sequencing technologies have offered unprecedented systems-level insight into the composition and diversity of microbial communities. However, our ability to perform functional studies on microbial communities is comparatively lacking, as most microbial culture tools are optimized for studying individual microbes in isolation. Traditionally, microbial interactions are assayed using pairwise co-cultures performed in conventional laboratory cultureware, which are ill suited for screening and re-assembling the vast parameter space of interactions within communities. Here we report a modular and scalable microbial co-culture platform named the “microbial community fitness landscape” (μCFL) for systematically screening the fitness of a target/reporter strain when co-cultured with a variety of 3-member microbial communities.

6.2 Introduction

Much of modern-day microbiology was established from the one microbe, one disease hypothesis known as Koch’s postulates, formulated by Robert Koch and Friedrich Loeffler in the late 1800s, from which the golden age of microbiology ensued. As such, classic microbiology has primarily been performed using a reductionist approach, i.e. isolating each individual member of the community and studying the individuals in isolation. More

recently, scientists have recognized that this singular microbe-disease causative relationship is an oversimplification – microbes are highly social organisms that reside within complex multi-species communities, and these communities play significant roles in ecology and human health. Although the classic approach of studying individual microbes in isolation offers advantages of simplicity, it cannot recapitulate the emergent phenotypes that result from microbial community interactions. Different microbes within a community can exchange nutrients, energy, and information with each other via diffusible factor signaling (quorum sensing) or physical contact, and these interactions drive the structure and dynamics of the microbial population. The importance of microbial communities in human health and disease has also gained attention in recent years, and spurred efforts in engineering microbial communities for therapeutic interventions[107-109].

Current standard technologies for studying microbial communities include 16S ribosomal RNA (rRNA) sequencing[110,111], fluorescence in situ hybridization (FISH)[112,113], and macroscale (mostly pairwise) co-cultures[114,115]. 16S rRNA sequencing can provide valuable information regarding which microbial members are present within a community but cannot elucidate what interactions occur between which members of the community. FISH can provide information regarding the spatial distribution of different microbial members within a sample, but cannot infer functional readouts, is challenging to perform and is also limited to the number of fluorescent probes and wavelengths available. Pairwise co-cultures are generally performed in conventional laboratory culture vessels like multi-well plates, tubes, and solid agar plates. Although suitable for small scale interaction screens for a handful of microbes, it is not well-suited for the task of screening

and re-assembling the vast parameter space of interactions within natural microbial communities. We argue that a significant bottleneck in microbiome studies is the lack of practical co-culture tools with sufficient throughput to enable systematic functional screening of microbial community interactions. This is a critical piece of the puzzle to enable scientists to gain functional insight and understanding of how different community members interact and drive community behavior within the microenvironment.

One of the main reasons for the lack of large-scale combinatorial co-culture studies is the prohibitively high number of possible combinations for interactions within a microbial community. The number of possible *k* combinations between a number of members *n* increases dramatically with each increasing number of members and can be described as *C (n, k)*, which is defined as the number of combinations of *n* members taken *k*.

$$C\,(n,\,k) = \frac{n(n-1)(n-2)\cdots(n-k+1)}{k!}$$

For example, the possible number of 3-way interactions between 5 different members is 10, for 10 members it is 120, and for 100-members it becomes a huge 161,700 possible combinations assuming just one condition per combination.

To address this need in combination throughput, there have been recent developments in employing microfluidic technologies for the study and assembly of microbial communities. The majority of these studies employ droplet microfluidic technology, i.e. using fluorescently encoded droplets (or microbes) for performing random community assembly by droplet merging[116-119]. Microbial growth is monitored using fluorescent reporter strains or fluorescent metabolism tracking dyes (such as resazurin). Droplet

microfluidics offers very high throughput (>10^5 combinatorial conditions), but the technology still has a few limitations, including 1) difficulty in quantifying the growth of individual strains in a given droplet unless different fluorescent reporter strains are used due to the mixed liquid culture condition, 2) limited culture time due to the small volume (~nL scale) of droplets, 3) only mixed liquid culture conditions can be studied, so interactions that rely on spatial segregation on a solid surface (i.e. agar) cannot be interrogated[120]. While a few non-droplet-based microscale co-culture platforms for microbes have also been developed[121-125], most of these approaches are seldom designed to examine the interactions of more than three different microbial members at one time, with the majority only used for studying pairwise interactions and for a smaller number of interacting members at a given time.

Here we report an alternative microbial community co-culture platform termed the "microbial community fitness landscape" (μCFL). The μCFL enables spatially segregated co-culture of multiple interacting microbial members at the same time but limits the interrogation of interactions to a "localized limited parameter space" for ease in data interpretation. This allows for a more holistic, community-level approach to functional microbial studies but preserves individual species-level resolution for interactions. We further developed a custom software pipeline to automatically generate an optimal combinatorial experimental design layout and automated image data analysis. Lastly, we demonstrated the μCFL platform using 10 rhizosphere microbial co-isolates for screening community-induced changes in fitness in *Bacillus cereus* as a model target strain.

6.3 Results and Discussion

6.3.1 Design of the μCFL device

The μCFL device is developed with the following design goals: 1) it must be compatible with current gold standard microbial culture methods, reagents, and readouts and allow for the flexible adjustment of culture conditions; 2) simple to operate and implement by the microbiological community using only broadly available standard laboratory equipment; 3) ability to generate a relatively large number of combinations with ease; 4) possess a simple and high content data readout; 5) scalable in terms of number of different microbial members. The core design of the μCFL device is an array of equilateral triangular combination wells, which are each connected to 3 circular variable wells by each vertex of the triangle. Each circular variable well is connected to up to six triangular combination wells in a hexagonal layout (Figure 6.1). The variable wells can each be introduced with a different experimental variable, such as a microbe, antibiotic, or other factor, whereas each triangular combination well can be introduced with the same fixed factor “experimentee”, usually a microbial “target” strain. In this way, each combination well can be considered as a combinatorial “fitness zone” expressed as the function of the sum of three variable wells. This design enables the high-throughput screening of three interacting variables within one well at a time.

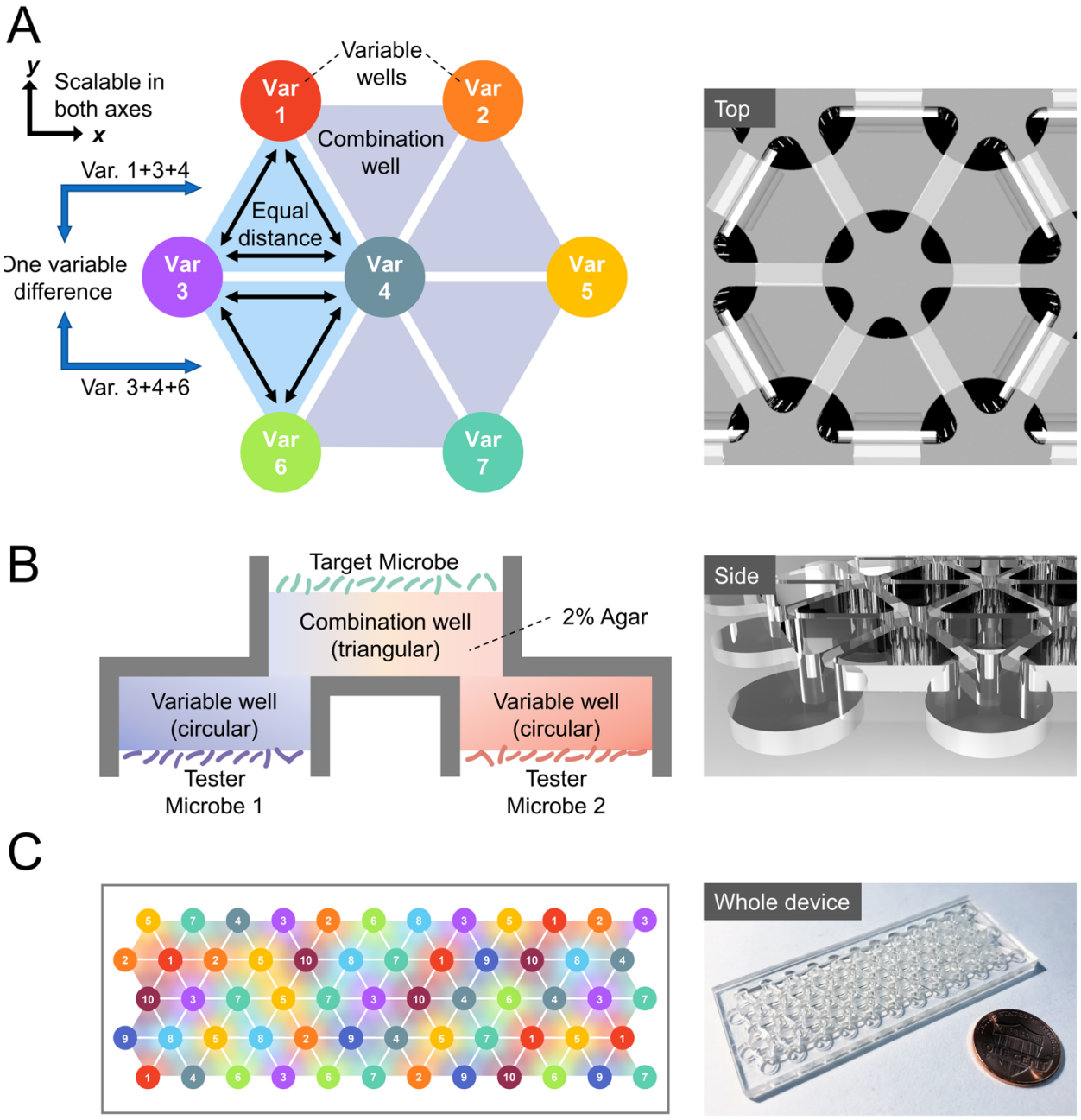

Figure 6.1: Design of the μCFL device. (A) top view, (B) cross section, and (C) whole device schematic and image of the μCFL device. A United States one-cent coin is included for scale. Each combination well generates a 3-variable combination gradient.

The choice of the triangle instead of other geometrical configurations is due to the following considerations: 1) The distance between each vertex of an equilateral triangle is the same, which allows for “equal strength” in terms of interaction distance between

different microbial members, which is not accomplishable using geometries with larger number of sides; 2) The triangle is the most basic unit that can define a planar surface, which allows the community interaction landscape to scale out in both the *x* and *y* dimensions, whereas a linear 2-way interaction network is confined to only one dimension at a time in terms of geometrical design; 3) A triangle can be joined with another equal triangle via 1 side, which allows the two triangles to share 2 connecting vertices, but each having one vertex that is not shared. This allows for a 3-factorial but single variable comparison between any 2 neighboring triangular combination wells; and 4) 3-way interactions are more manageable in terms of scale of experiments compared to higher numbers of combinations for the number of participants within a microbial community.

The μCFL device employs a 2-layer fabrication approach with the variable and combination wells separately milled out of polystyrene then bonded together. In this configuration the variable wells and the combination wells face opposite directions (Figure 6.1B), which allows for soluble factor (contact independent) communication, prevents cross contamination between wells, and allows for co-culture of microbes without intermixing. Although we acknowledge that microbial interactions can be contact mediated, it is challenging to achieve spatial isolation (thus enabling individual optical readouts of growth for each member of a community) using contact-mediated mixed co-cultures. To optimize the design of the μCFL device for microbial community testing, we tested various device sizes with a well pitch ranging from 4.5 mm to 6.5 mm to find an optimal diffusion distance for co-culture (as microbial interactions within the μCFL device are diffusion-mediated). That is, a diffusion distance that is short enough to allow the target strain to show robust community co-culture induced phenotypes within a 1~2 day

culture period, but not too short so that cross-combination-well interference may start to become an issue. We first characterized soluble factor diffusion through the device using a fluorescent small molecule with a similar molecular weight to that of antibiotics (Rhodamine 6G, MW: 479.02) with time-lapse fluorescence microscopy to monitor the diffusion profile over time (Figure 6.2A, 6.2B). Results show that the fluorescent small molecule was more rapidly depleted from the 4.5 mm pitch device, whereas the 5.5 mm, 6 mm, and 6.5 mm device show slower depletion profiles (Figure 6.2C, 6.2D) as is expected due to its shorter diffusion distance. To further investigate the diffusion behavior of the μCFL device, we added a high concentration antibiotic (80 μg/mL gentamicin, MW: 477.6) to one of the variable wells, and inoculated GFP expressing *Bacillus cereus* (*B. cereus* GFP) as a target strain to the combination wells (Figure 6.3A). Fluorescent images of the combination wells were captured following a 1-day culture. Results suggest significant cross-combination well interference in the 4.5 mm pitch device (significant growth inhibition for neighboring combination wells), slight inhibition at the very edge of a neighboring combination well in the 5.5 mm pitch device, and no observed neighboring well inhibition for the 6 mm and 6.5 mm pitch devices (Figure 6.3B). As such, we selected the 6 mm pitch design for all subsequent experiments. We also loaded 4 different colored fluorescent cell tracking dyes into each variable well of the 6 mm device to show that the device can successfully generate a 3-factor combination gradient within each combination well (Figure 6.2E).

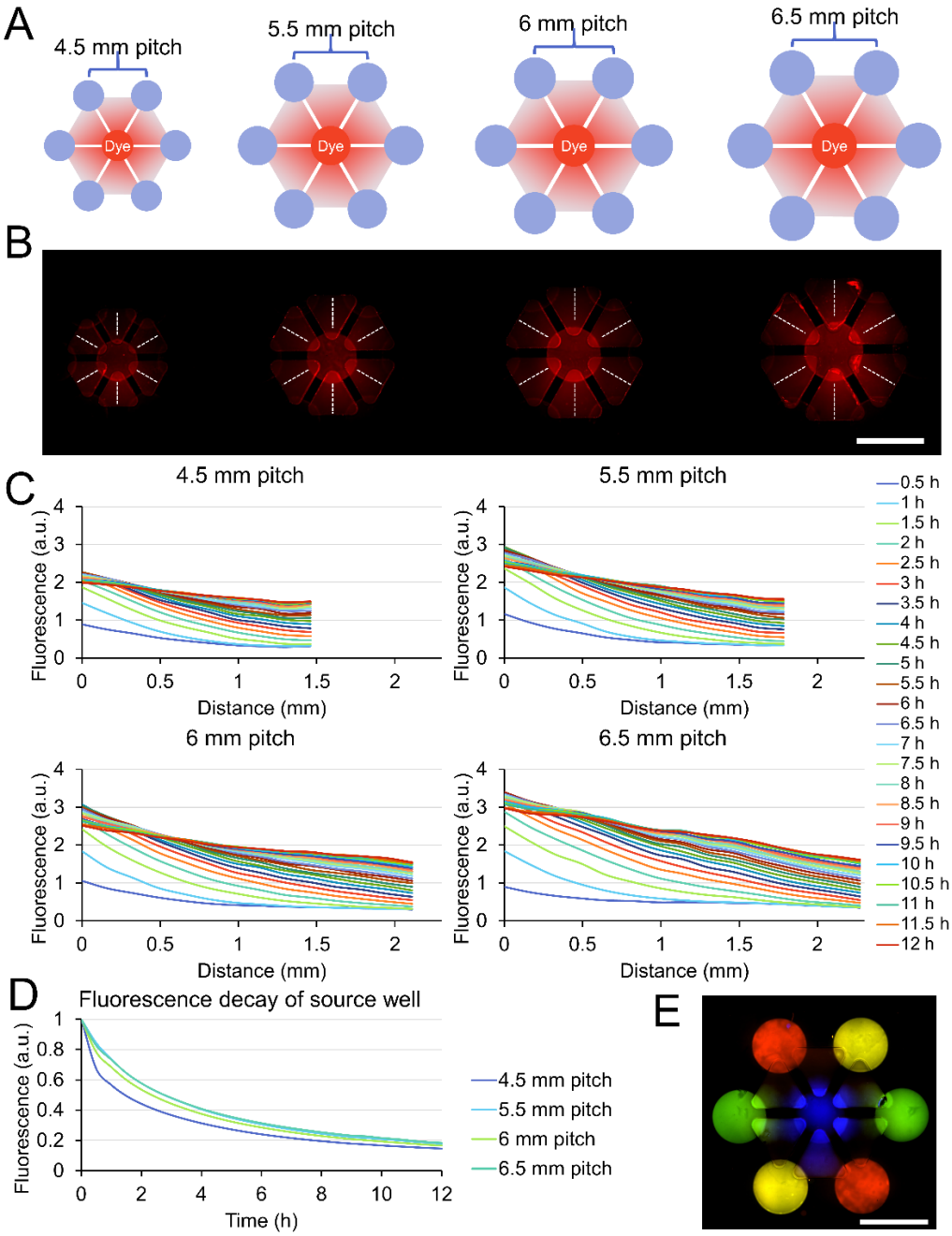

Figure 6.2: Soluble factor diffusion in μCFL device. (A) Diffusion was characterized by adding a fluorescent small molecule dye (Rhodamine 6G) into the center variable well and allowing for passive diffusion over a period of 12 hours. (B) Fluorescence images of Rhodamine 6G diffusion out of the center variable well. Scale bar: 5 mm. (C) Mean fluorescence diffusion profiles across the combination wells (dotted white line in (B)) over a 12-hour period. (D) Fluorescence decay of the center variable (source) well over a 12-hour period. (E) 4-color combinations were accomplished using 4 cell tracking dyes (Blue: cell tracker blue, green: cell tracker green, red: cell tracker red, yellow: cell tracker deep red). Scale bar: 5 mm.

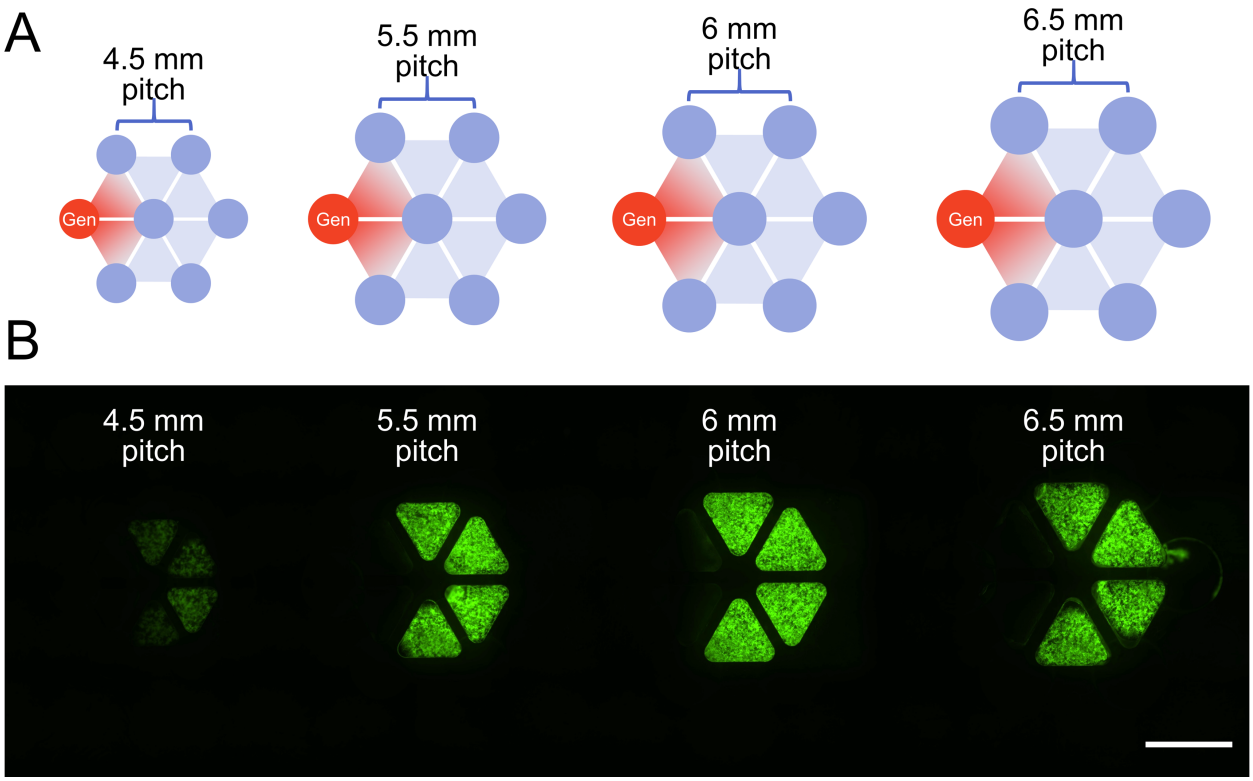

Figure 6.3: Antibiotic diffusion in the μCFL device across different well pitches. (A) Experimental layout of gentamicin diffusion experiment. Gentamicin was added at a concentration of 80 μg/mL into the left-most variable well. The target strain (*B. cereus* GFP) was inoculated into the combination wells and cultured for 1 day. (B) Fluorescence microscopy images of the μCFL device with 4 different well pitches. Scale bar: 5 mm.

Finite element modeling (FEM) using COMSOL Multiphysics software also suggested that a gradient can be maintained across the agar surface of the combination well of the 6 mm device (Figure 6.4A, 6.4B), and the FEM diffusion profiles appear similar to the fluorescence diffusion profiles of Rhodamine 6G (Figure 6.4C). After optimizing the design of the basic hexagonal μCFL unit, we scaled the hexagonal unit to a device with 60 variable wells and 88 combination wells (Figure 6.1C). It's worth noting that different device configurations can be easily made by scaling the modular hexagonal unit, to fit the scale of the experiment (number of combinations required) in question.

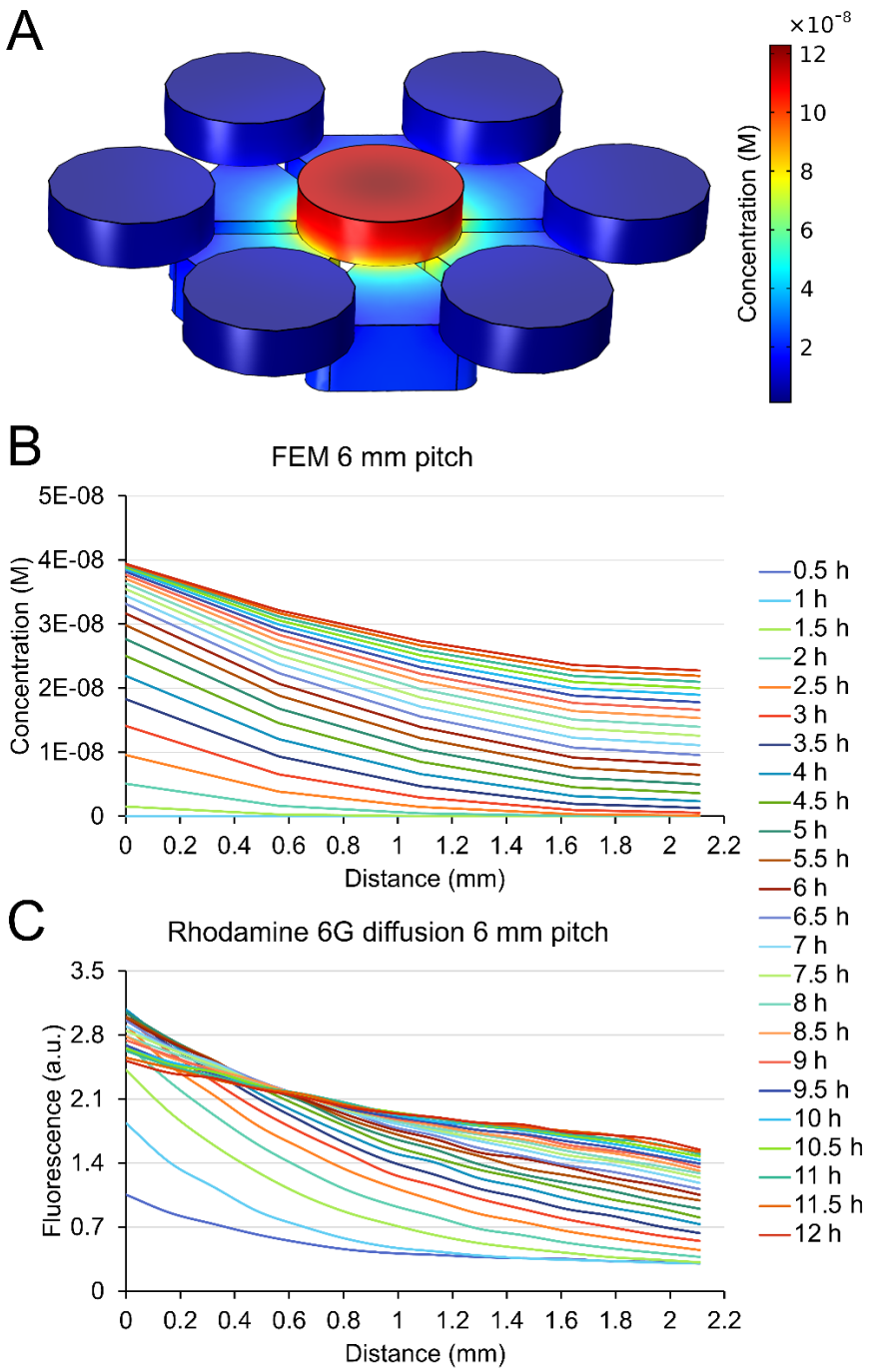

Figure 6.4: Finite element modeling (FEM) of small molecule diffusion in the 6 mm pitch μCFL. (A) 3D Comsol model of diffusion within the μCFL device. (B) FEM diffusion profile across the agar surface of the combination well (where the target microbes reside). (C) Fluorescence diffusion profile of rhodamine 6G across the combination well (same as Figure 6.2C, panel 3).

6.3.2 Detection of soluble-factor-mediated microbial growth inhibition in the μCFL device

To validate that diffusible factors (antibiotics) introduced in the variable wells can result in a measurable differential growth response in the combination wells, we added into the variable wells an antibiotic, gentamicin at a concentration ranging from 5 to 80 μg/mL and blank vehicle control (Figure 6.5A). *B. cereus* GFP was inoculated into the combination wells and cultured for 1 day. After culture, the μCFL device was imaged on a fluorescence microscope and the images were analyzed using ImageJ to quantify the growth of *B. cereus.* Results show a dose-dependent response of *B. cereus* to gentamicin, suggesting that soluble factor-mediated differential growth patterns can be detected on the μCFL with good resolution.

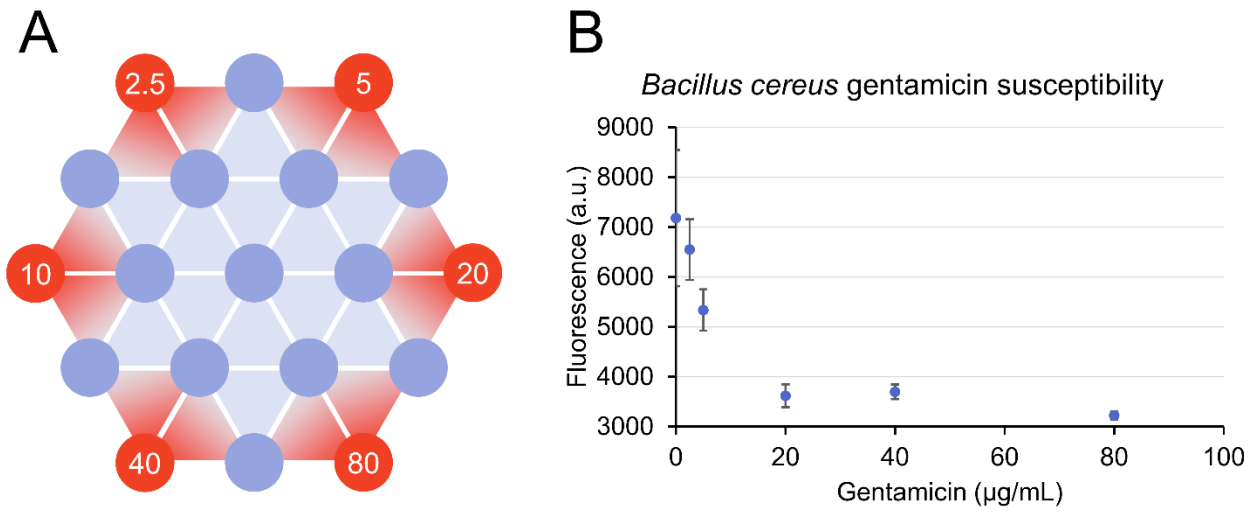

Figure 6.5: Antibiotic susceptibility testing of *B. cereus* in μCFL device. (A) Layout for antibiotic (gentamicin) dosing on μCFL device. Red circles denote the wells that were added gentamicin, and the numbers indicate the antibiotic concentration (in μg/mL). (B) Mean quantified fluorescence of *B. cereus* GFP in the triangle combination wells at the indicated antibiotic dose. Error bars denote the standard deviation from 2 replicates.

6.3.3 Experimental design and workflow of the μCFL device

Owing to the complexity of designing 3-factorial combinatorial experiments for large numbers of microbial strains, we have developed a custom automated experimental design and data processing workflow in MATLAB (The MathWorks, Natick, MA) for the μCFL device (Figure 6.6). In brief, a user inputs the number of variables (tester microbe strains) to be tested for a given experiment into the MATLAB script, which attempts to search for an experimental layout with maximal combinatorial space coverage on the device and minimal repeats (details in Materials and Methods section). Tester microbes are then inoculated in the variable wells according to the generated layout, followed by inoculation of fluorescent target strains in the combination wells. After inoculation, fluorescence images of the target strains in the combination wells (facing down) are captured at set time intervals. The images are analyzed using a custom ROI array in Fiji (https://fiji.sc/) to quantify the mean fluorescence intensity of each combination well (which informs the total growth of the well) and the 3 vertices of the combination well (which informs which tester strain likely contributed more to the increase or decrease in growth of the target strain) (Figure 6.7). The analyzed fluorescence intensity was then imported back into MATLAB, which maps each datapoint to the associated strain combination indicated by the generated experimental layout and plots out the combination-mediated growth patterns into a “heatmap” (Figure 6.8).

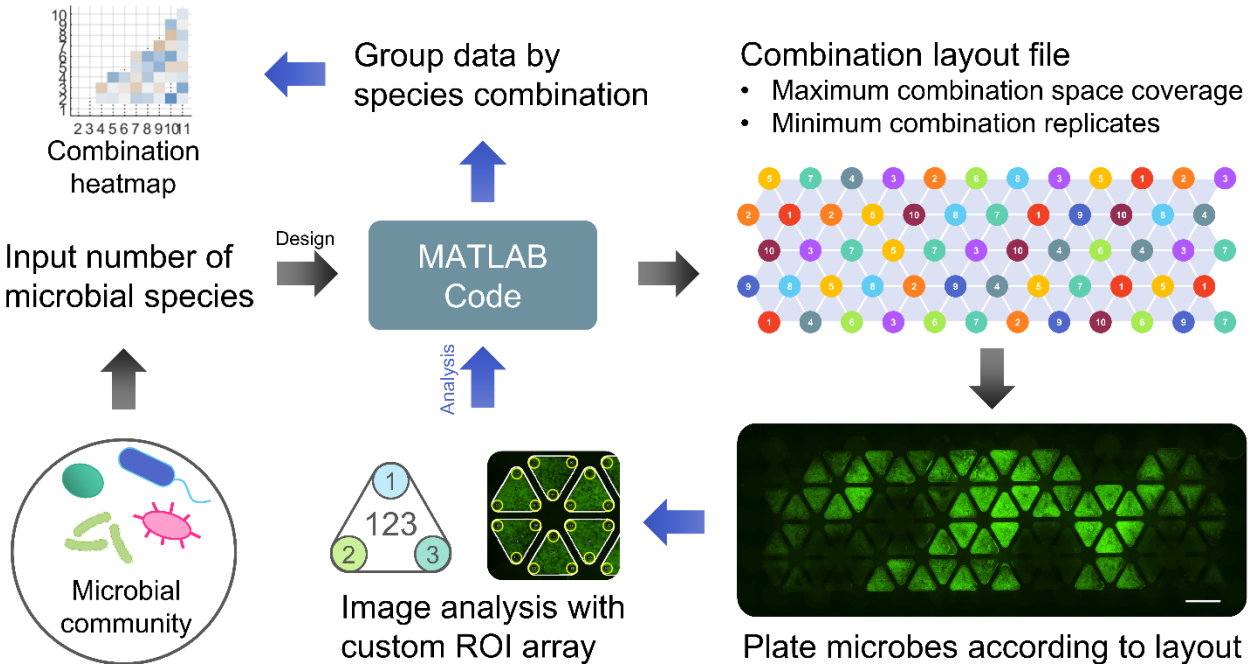

Figure 6.6: Experimental workflow of the µCFL device. A custom MATLAB script generates random experimental layouts according to the number of microbial members to be tested, and for sorting and analyzing the quantified image data following experiments. Scale bar: 5 mm

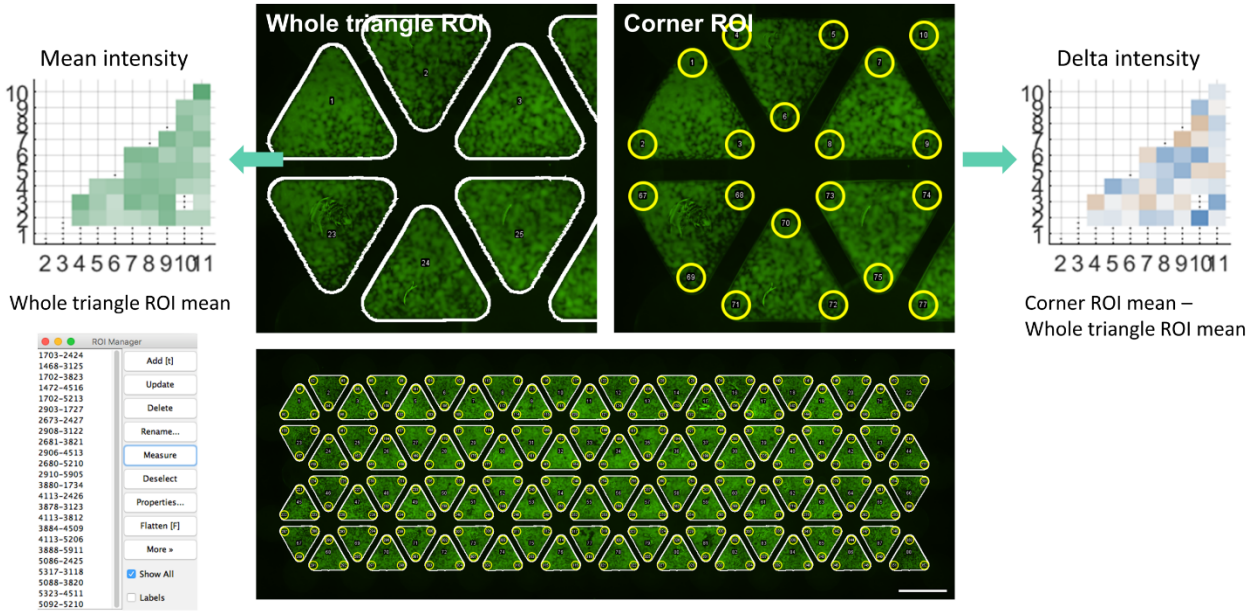

Figure 6.7: Image analysis ROIs for quantification of mean fluorescence intensity in the whole triangle (left) and the corners of the triangle (right). Scale bar: 5 mm

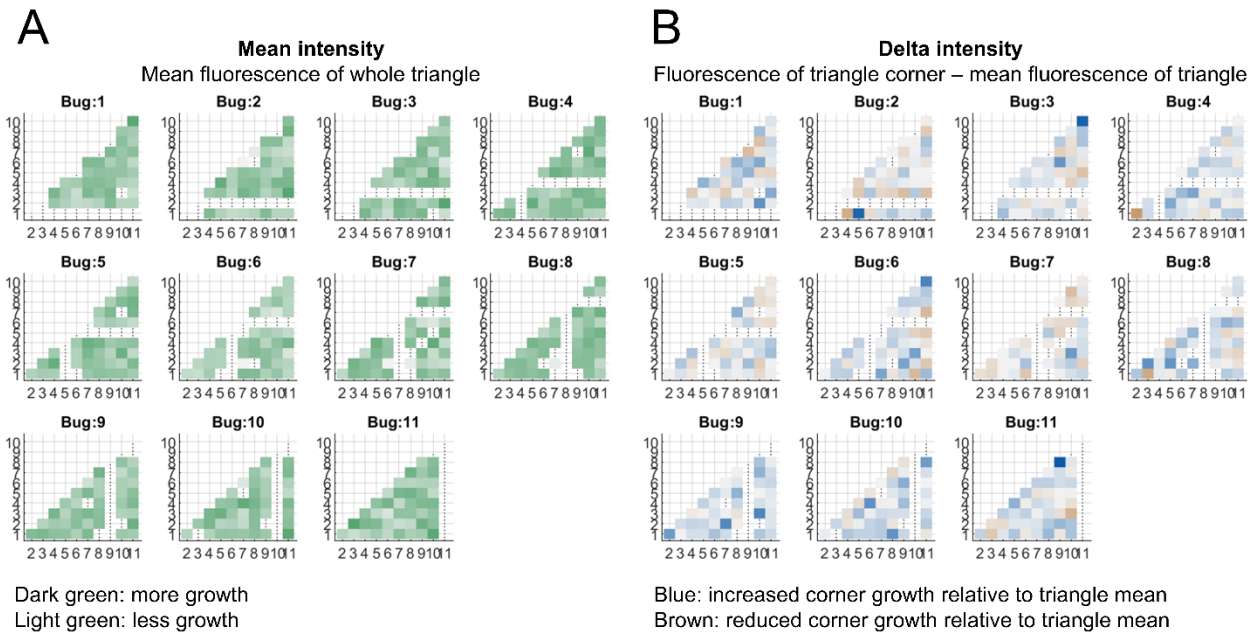

Figure 6.8: Combination heatmaps showing triangle mean (A) and corner delta (B) fluorescence intensity of the target strain sorted by the tester strain (bug) combinations.

6.3.4 Tester strain inoculation time and concentration affects response of the target strain

The outcome of microbe-microbe interactions can be affected by the concentration and sequence of inoculation[126-128]. For instance, microbes show higher tolerance of antibiotics when they've already grown to a high density compared to when their densities are low[129]. In the μCFL device, there is a time lag between inoculation and when the microbes start "sensing" each other in the device as it takes time for secreted factors to diffuse from the tester strains through the agar to reach the target strains in the combination wells. All the while, both tester strains and target strains would be theoretically continuously growing. Initially, we inoculated the tester and target strains simultaneously in the device followed by culture and image acquisition. However, we did not observe large differences in target strain growth when they were co-cultured with different communities, which led us to

hypothesize that the target strains may have already established significant numbers before they start sensing and responding to the secreted factors from the tester strains and hence community-induced phenotypes were muted. We then conducted an inoculation time and concentration experiment using 4 tester microbes and a target microbe (*B. cereus* GFP) selected from a previously reported rhizosphere community[130] (with a total of 3 different 3-tester combinations), and found much greater differences in target strain growth when the tester strains were inoculated 6 hours prior to the target strains compared to when they were inoculated simultaneously (Figure 6.9). For the 24-hour time point, the greatest difference in community-mediated growth was observed when the tester strains were inoculated at 10 times the concentration, 6 hours prior to the target strain (tester strain OD = 0.1, target strain OD = 0.01), (Figure 6.9B). For the 48-hour time point, the greatest difference was observed when tester and target strains were both inoculated at OD = 0.01 (Figure 6.9B). Additionally, at the 48-hour time point, we observed growth greater than the no-tester control when tester were inoculated at OD = 0.01 and 0.001, but all community combinations exhibit growth lower than the no-tester control when the testers were inoculated at OD = 0.1 (Figure 6.9B right panel, Combo236). We thus decided to inoculate the tester strains 6 hours prior to the target strains with an inoculation OD of 0.01 for both tester and target strains for subsequent experiments.

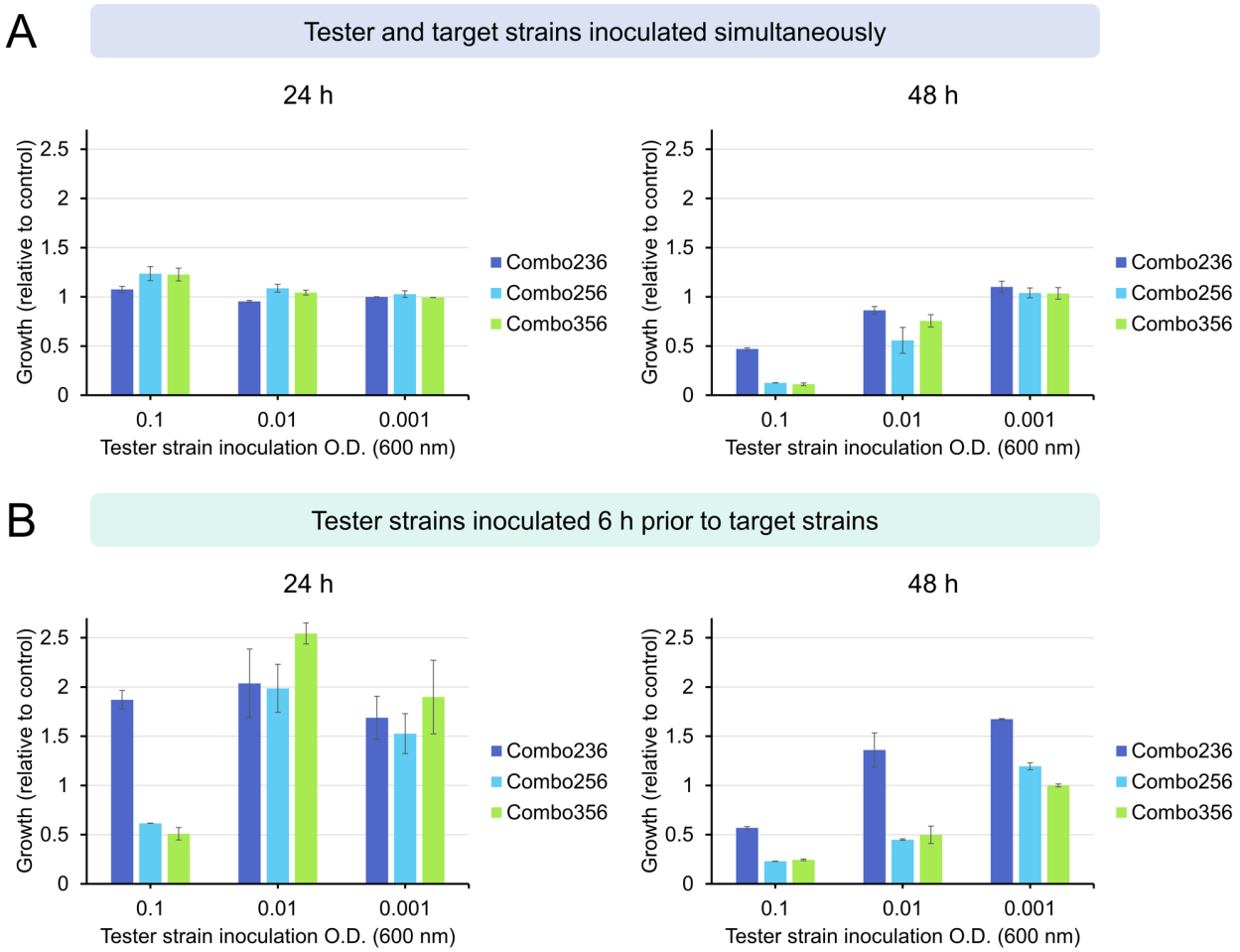

Figure 6.9: Inoculation time and concentration of tester strains affects growth response of target strain in the μCFL device. (A) Tester strains (microbes 2, 3, 5, and 6) inoculated simultaneously with the target strains. (B) Tester strains inoculated and allowed to grow for 6 hours prior to inoculating target strains. Error bars denote the standard deviation from 2 replicates.

Community screening of a 10-member rhizosphere community on the μCFL device

To demonstrate the screening of microbial communities with higher complexity on the μCFL device, we randomly selected 10 microbial strains from a previously reported rhizosphere co-isolate community (24). 10 strains result in a total number of possible 3-way combinations of 120 and, thus, full combination space coverage using 2 devices (88-combination wells/device) can be achieved. Owing to geometrical constraints, some

combinations were thus repeated more than once per experiment. Overnight liquid cultures of tester strains were inoculated at OD 0.01 into the variable wells and cultured for 6 h followed by inoculation of the target strain (*B. cereus* GFP) at OD 0.01 into the combination wells. A control device (variable wells added with vehicle control (PBS)) was also run in parallel to each experiment for growth normalization (Figure 6.10).

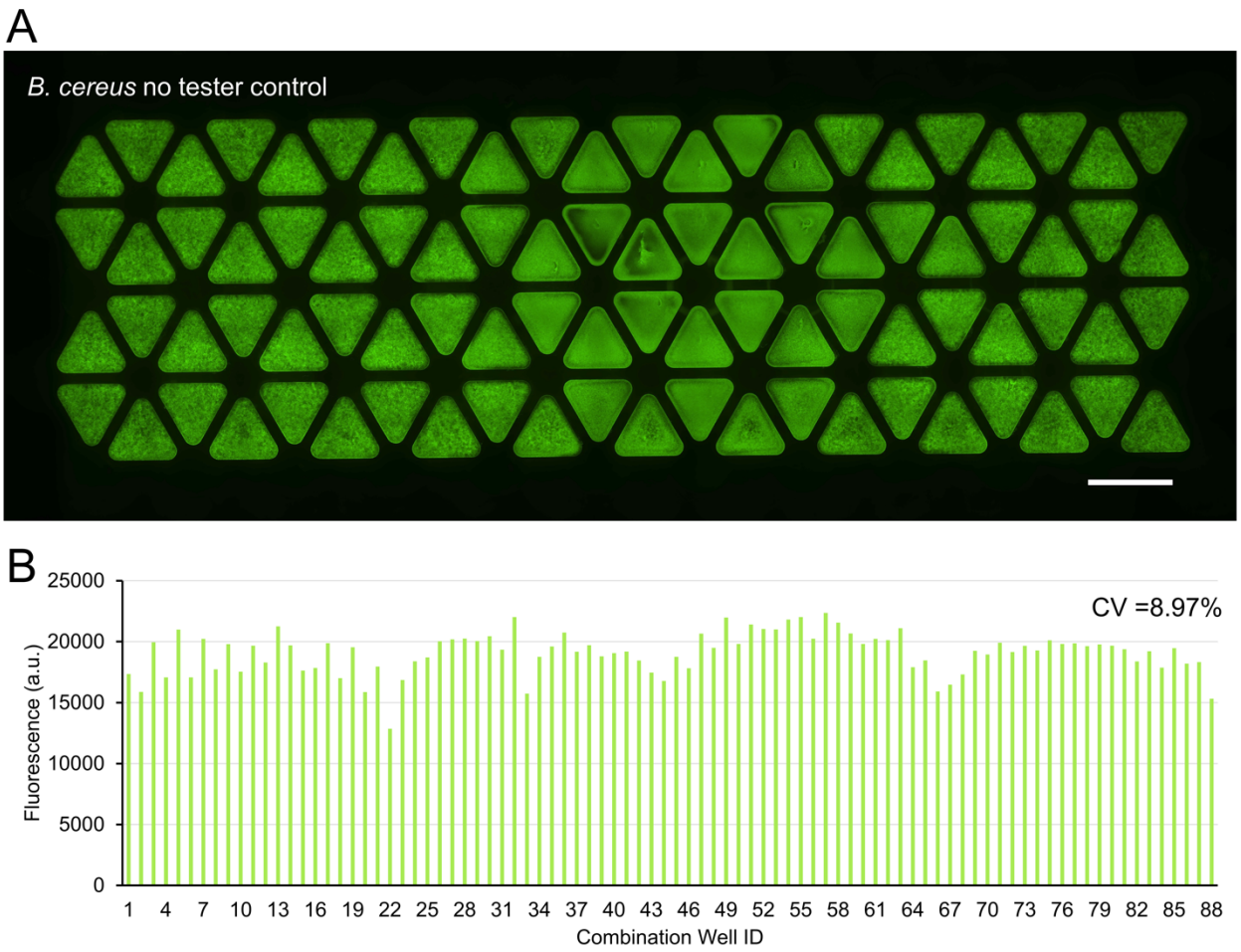

Figure 6.10: No tester (vehicle) control of target strain (*B. cereus* GFP). (A) Fluorescence image, and (B) quantified fluorescence of each well of the μCFL device inoculated with the target strain in the combination wells. Scale bar: 5 mm. CV = coefficient of variation.

The devices were then incubated at RT for 2 days with fluorescence images captured on both day 1 and day 2. Results show by day 1, large differences in growth across different community combinations was observed (Figure 6.11A-B, Table A.3), with both increased and decreased growth relative to no-tester control (Figure 6.11B). We observed similar target strain growth trends across different communities for day 1 and day 2 ($R^2 = 0.8584$), except the fluorescence intensity of the target strain was generally brighter on day 1 across the board (Figure 6.11C), suggestive of growth inhibition. To gain insight into the growth promoting/inhibiting trends of each strain within the community, we sorted the growth data by communities which contain a given tester strain (Figure 6.11D). While each data point represents the integrated effect of a 3-member tester community on the target strain, growth promoting/inhibiting trends for individual tester strains were observed. For instance, microbe 5 (*Pseudomonas sp. CI14*) was found to be correlated with a general reduction in growth across all communities, whereas communities containing microbe 6 (*Achromobacter sp. CI16*) were found to exhibit higher growth trends (Figure 6.11D). Some tester strains are also found to be correlated with a narrower spread in target strain growth trends (i.e., microbes 5, 6, 8), suggesting a stronger growth modulating role in the community than tester strains that exhibit broad target strain growth trends (Figure 6.11D). Consistent with Figure 6.11C, individual strain-correlated growth trends were observed to be similar between day 1 and day 2 (Figure 6.11D). When we plot the fluorescence of the growth of the target strain in the Z-axis, we can obtain a "fitness landscape" plot (Figure 6.12), showing combination areas with higher fitness (the "hills") and lower fitness (the "valleys").

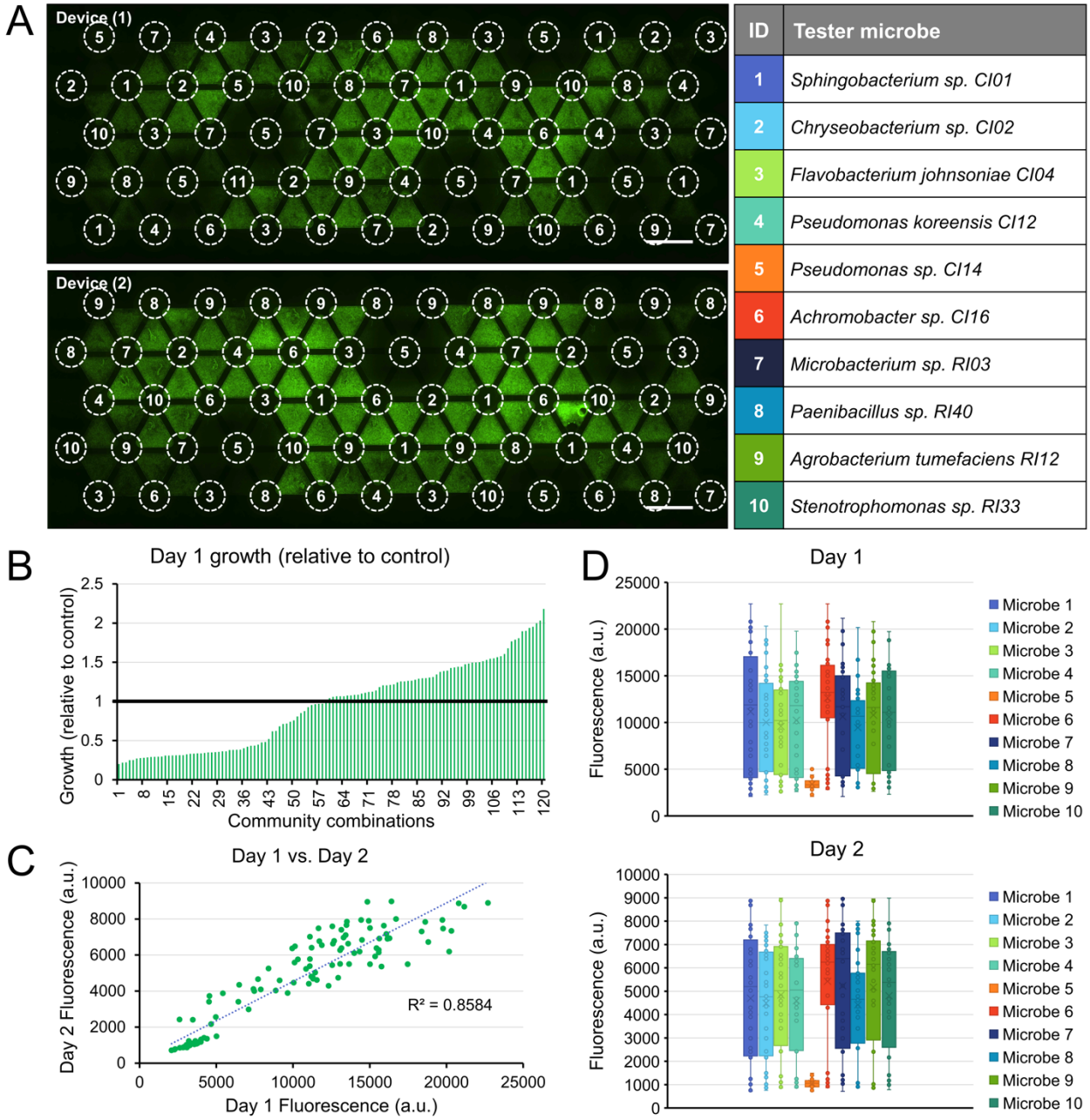

Figure 6.11: Community combination screening of a 10-member rhizosphere community on the μCFL device. Fluorescence microscopy images of target strain *B. cereus* GFP on the μCFL device after co-culture with a 10-member rhizosphere community. Scale bar: 5 mm (B) Quantified growth (relative to no-tester control) of the target strain when co-cultured with each microbial community. Data is organized in increasing order. Growth equal to the no-tester control would have a value of 1 (shown as the black horizontal line). (C) Linear regression of target strain growth on day 1 vs. day 2 across all 3-member tester communities. (D) Target strain growth sorted by tester microbial communities which contain the indicated tester strain (n=3).

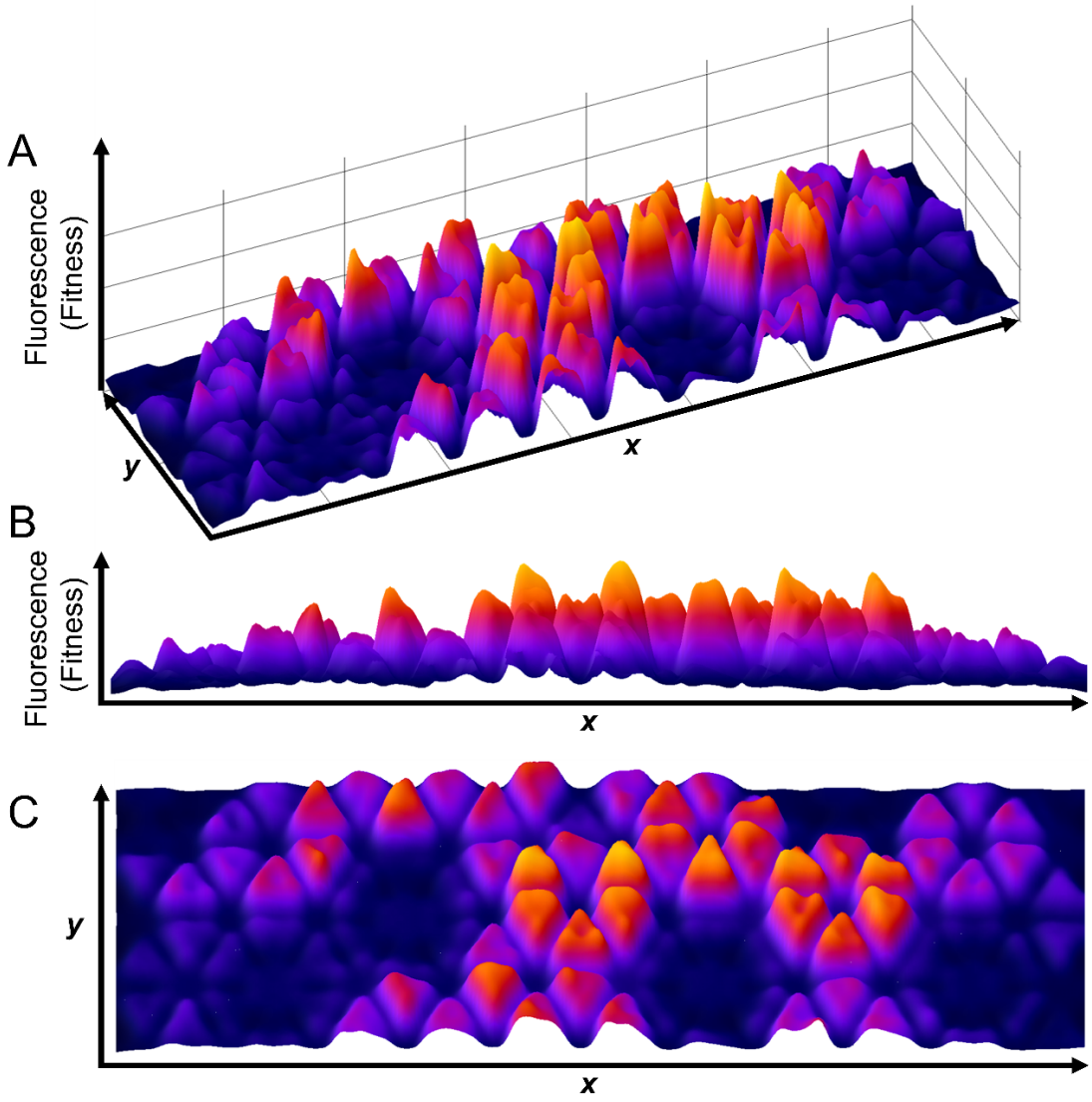

Figure 6.12: Surface "fitness landscape" plots with fluorescence intensity represented in the z-axis. Panels (A-C) represent different views of the fitness landscape plot.

We then performed a time-lapse microscopy experiment to observe community-modulated target strain growth curves over time and found similar strain-specific growth modulating trends (Figure 6.13), with microbe 5 showing the greatest growth inhibition.

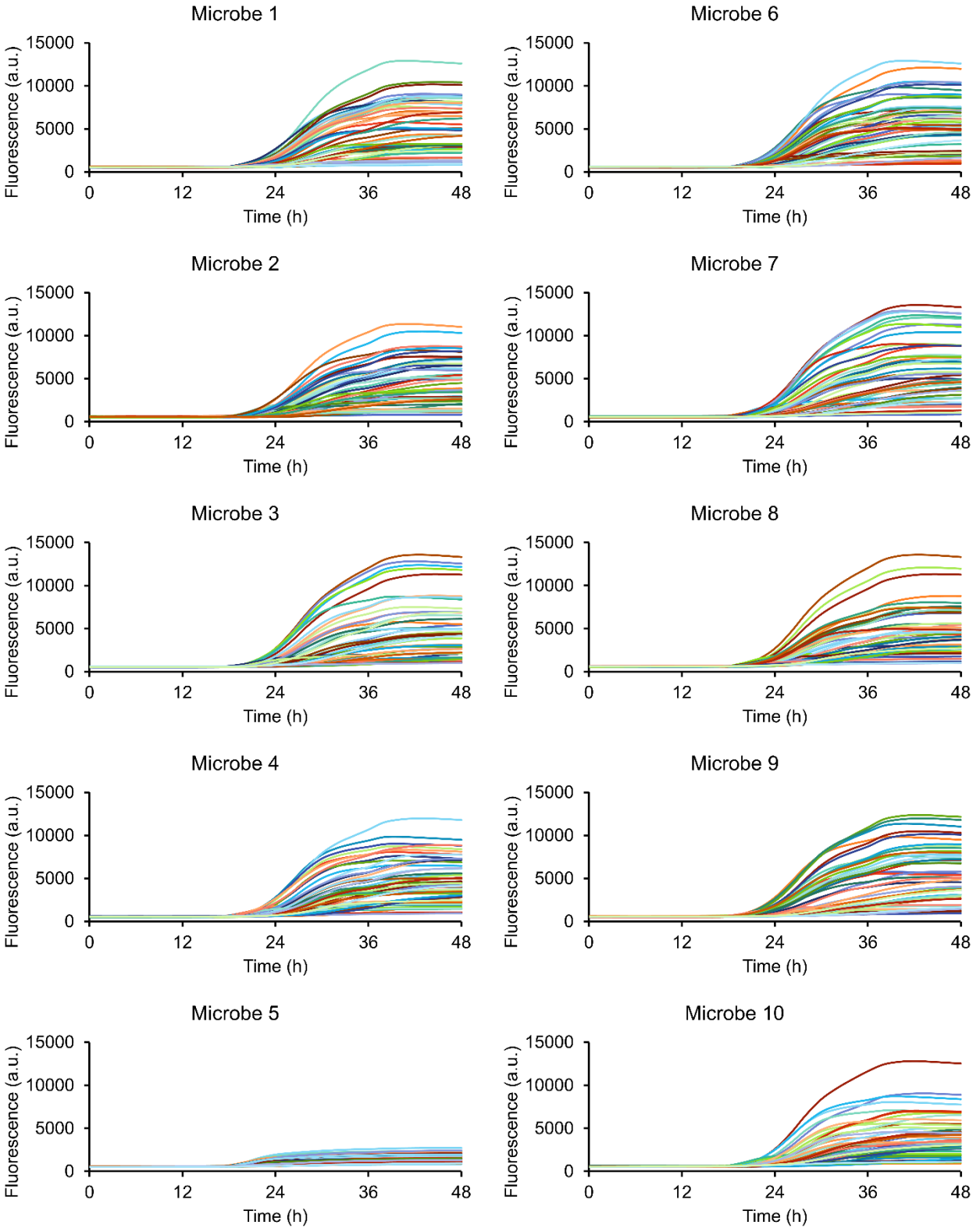

Figure 6.13: 48-hour time-lapse growth curves of target strain sorted by tester microbial communities which contain the indicated tester strain.

We also captured autofluorescence images of the device in the UV channel (excitation 390 nm, emission 440 nm) and surprisingly discovered that microbe 5 secretes a compound that fluoresces in this channel (Figure 6.14). However, we found that the secretion of the autofluorescent compound by microbe 5 is independent of community co-culture, as no significant difference in fluorescence intensity was observed when microbe 5 is cultured in isolation, in co-culture with the target strain, or in co-culture with the target strain and microbes 2, 3, and 6 (Figure 6.15).

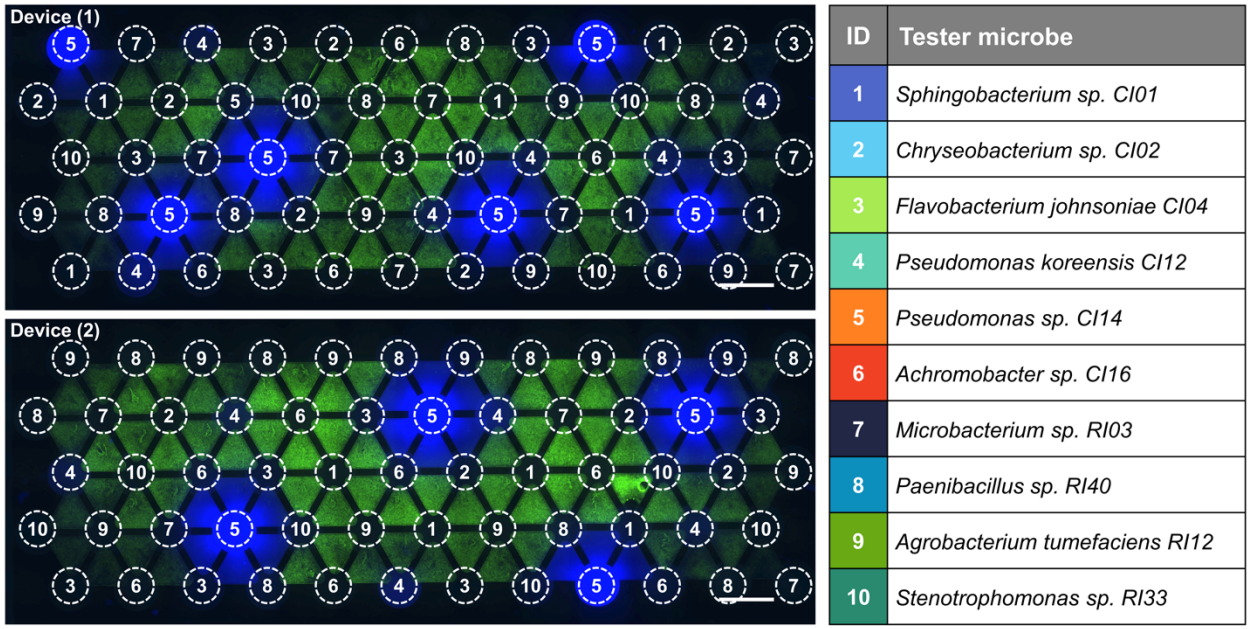

Figure 6.14: Fluorescence microscopy image of community combination screening of a 10-member rhizosphere community on the μCFL device. Green: target strain (*B. cereus* GFP), Blue: autofluorescence. Scale bar: 5 mm.

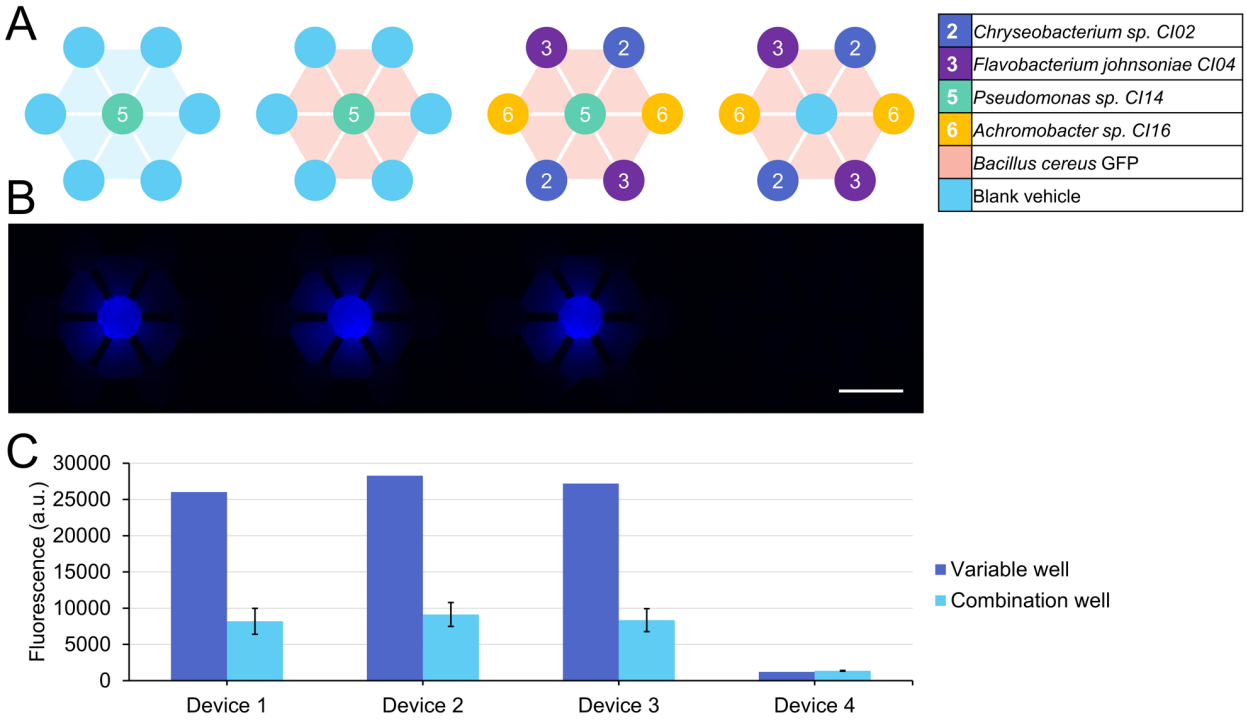

Figure 6.15: Secretion of fluorescent blue compound by microbe 5 in monoculture or co-culture. (A) Experimental layout. (B) Fluorescence image of fluorescent blue compound secreted by microbe 5. Scale bar: 5 mm (C) Quantified fluorescence of the variable wells and combination wells from (B). Error bars denote the standard deviation from 6 replicates.

6.3.5 Towards the development of a multi-kingdom gut-microbe co-culture model using the μCFL platform

Up to this point we've only shown microbe-microbe interaction experiments on the μCFL platform. However, microbes, in addition to interacting with members from its own kingdom, also extensively interact with a wide range of organisms/hosts outside its own kingdom. A well-known and human health-relevant example is the gut microbiome, which has been implicated in a wide range of human diseases and physiologies. The various members of the gut microbial community can interact with the host in ways that can affect the physiology of the host. The role of these interactions in human health and pathology have recently emerged, with various studies showing that microbial communities

inhabiting the gut plays a critical role in human pathologies like diabetes[131], obesity[132], Parkinson's[133], Alzheimer's[134,135], and cancers[136]. However, the majority of research in this field rely primarily on retrospective clinical studies on fecal samples using 16s rRNA sequencing, or animal models (commonly germ-free mice). Unlike traditional cell biology/microbiology studies which have an abundance of *in vitro* models that allows for more mechanistic/high-throughput/exploratory studies, very few practical *in vitro* models are available for multikingdom gut microbiome studies. This is primarily due to the challenges of developing a model that can support simultaneous anaerobic conditions (for culture of gut microbes), and aerobic conditions (for culture of gut epithelial cells). This necessitates development of new tools that can recapitulate host-microbe interactions within an *in vitro* culture environment. These co-culture tools[137] should possess a number of enabling characteristics, including: 1) support growth of both anaerobic gut bacteria and aerobic gut epithelial cells; 2) possess a means of data readout (such as imaging, transcriptional/protein analysis, etc.); and 3) straightforward operation and allow for sufficient long-term culture of the specific microbes and epithelial cells. In order to develop a biologically relevant *in vitro* gut model, several key components of the physiological gut anatomy would ideally have to be replicated. These include a gut epithelial layer, the gut microbial community, and an oxygen gradient with aerobic conditions supporting the epithelial cells and close to complete anaerobic conditions for the microbes. One of the enabling features of the μCFL platform is its compatibility with a broad range of culture methods, including mammalian cell culture which is enabled by its polystyrene material for cell attachment and optical access. The opposing orientations of

the multiplexing chambers and the variable wells also allow for the use of different media and different oxygen concentrations on both sides of the device (Figure 6.16, 6.17).

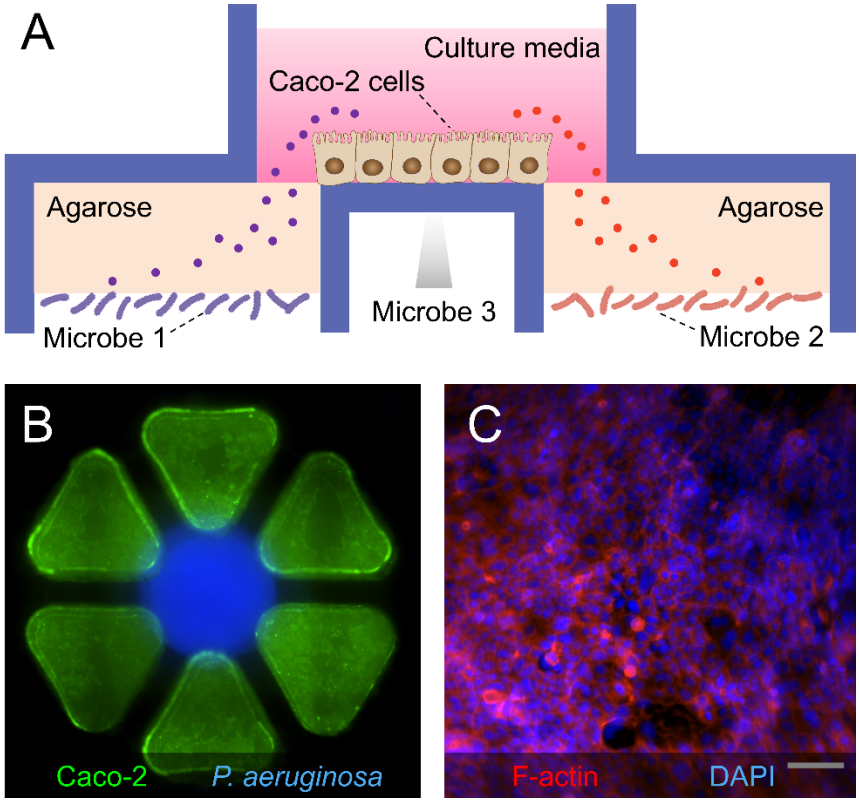

Figure 6.16: A gut-microbial multikingdom co-culture model on the μCFL platform. (A) Schematic of the co-culture of Caco-2 intestinal epithelial cells with 3 microbe species. (B) Co-culture of Caco-2 cells (stained green with Calcein AM live cell stain) with *P. aeruginosa* CFP (blue) on the μCFL platform. (C) Morphology of Caco-2 cells cultured for a week on the μCFL platform. F-actin was stained with Texas Red-X phalloidin, nuclei was stained with DAPI.

Although the majority of gut microbes are anaerobic, simultaneously maintaining anaerobic and aerobic conditions on the same device to allow for multikingdom co-cultures can be quite challenging in terms of engineering complexity. Thus, initially we first optimized the multikingdom μCFL culture model using oxygen tolerant fluorescent gut microbes co-cultured with intestinal epithelial Caco-2 cells. Caco-2 cells are first cultured in the multiplexing chambers of the μCFL for 2 weeks to enable cell differentiation

and polarization, followed by inoculation of the microbes into the variable wells, which were prefilled with solid agarose prior to cell seeding. Following co-culture, Caco-2 cell viability was evaluated using live/dead staining and cell morphology evaluated via Texas Red-X phalloidin staining of F-actin. In preliminary studies, we've successfully performed a 2-week long culture of Caco-2 on the μCFL platform, and co-culture of the Caco-2 cells with *P. aeruginosa* for 1 day with high viability (Figure 6.16).

We've also attempted to develop an anaerobic chamber enclosure to enable co-culture of intestinal epithelial cells with obligate anaerobic gut microbes in the multikingdom μCFL platform. The prototype design (Figure 6.17) consists of an anaerobic chamber on the bottom (the microbial side) of the device where a steady flow of nitrogen continuously purges out oxygen diffusing into the system from the cell culture side (the triangular combination wells), which faces upwards and is open to atmospheric air. This configuration creates a vertical oxygen gradient with the highest oxygen concentration at the top of the cell culture combination wells and the lowest concentration on the bottom agarose surface where microbes are inoculated (Figure 6.17). However, during the testing of this design, we encountered significant liquid evaporation issues leading to loss of cell culture media volume and shrinkage of the agarose gel. This issue is reduced, but still significant, when a humidifier was added to the nitrogen gas source (data not shown). As such, an alternative method for achieving anaerobic conditions for gut microbial culture (such as using an oxygen scavenging reagent in the bottom anaerobic chamber) might be needed to realize a mixed anaerobic/aerobic multi-kingdom gut co-culture model on the μCFL platform.

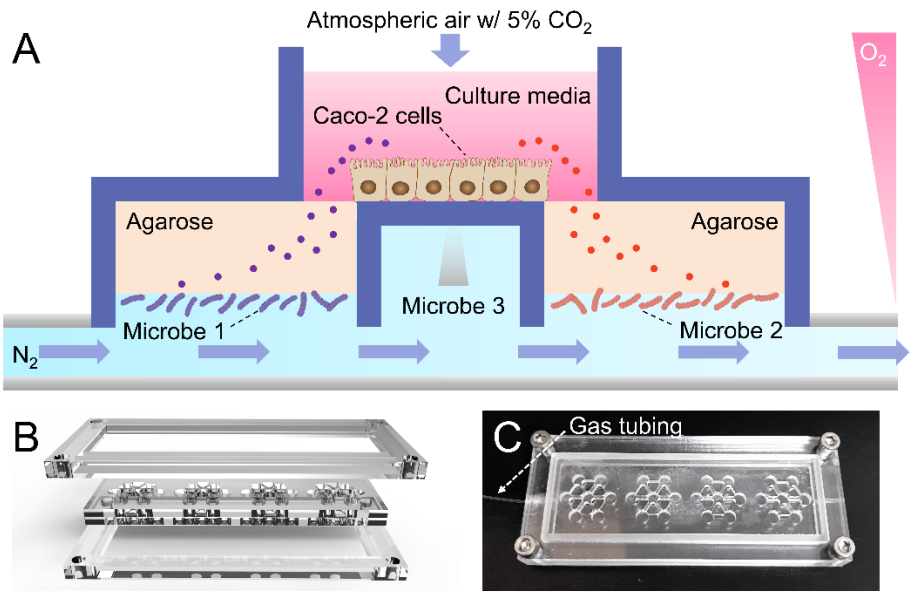

Figure 6.17: Prototype anaerobic gut-microbial multikingdom co-culture model on the μCFL platform. (A) Setup for the co-culture of Caco-2 intestinal epithelial cells with anaerobic gut microbes. (B) Assembly of anaerobic gas chamber (bottom) with μCFL device (center) for creating a vertical oxygen gradient. (C) Image of the assembled device with a gas tubing delivering nitrogen gas to the bottom microbial chamber.

6.4 Conclusions

Here we report a platform for systematically studying microbial community interactions. The μCFL platform is unique in that it allows for observation of localized microbial interaction events within smaller subsets of a larger microbial community, each subset serving as a small 3-member community fitness zone across the vast landscape of the bulk community ecosystem. The μCFL device was also designed to operate without any specialized equipment (just pipettes and a fluorescent microscope) and is relatively straightforward to operate (just simple pipetting), which makes it accessible to non-engineering labs. The polystyrene construction of the μCFL device also makes it

compatible with mammalian cell culture (we've demonstrated a 2-week long culture of Caco-2 intestinal epithelial cells on the device), opening up possibilities for developing a multi-kingdom gut co-culture model on the μCFL platform in the future.

While the μCFL opens up new experimental possibilities, it is not without its limitations. A current limitation is the use of fluorescent reporter microbes as the target strain, which reduces the flexibility of the method in assaying microbes of whom a fluorescent protein reporter is not available. This limits the platform's ability to assay microbial communities in anaerobic conditions (such as gut communities), as most traditional protein fluorophore reporters do not function in anaerobic conditions[138]. It will be of interest to develop alternative microbial growth quantification strategies such as employing a chemical reporter dye and/or imaging and image processing methods to allow for assaying microbes without a fluorescent reporter. We also envision that the μCFL will be a good platform for screening "probiotic" combination candidates for use in treatment of diseases which have a known pathogenic cause, or the study of the resilience or susceptibility of a stable community towards invader strains.

6.5 Materials and Methods

6.5.1 Device design and fabrication

Design of the μCFL devices was done using computer-aided design (CAD) software (AutoCAD, Autodesk Inc), and fabricated using a computer numerical control (CNC) milling machine (Tormach PCNC 770) with polystyrene as the device material as previously described[139]. The μCFL device design employs a 2-layer fabrication approach.

Namely, the variable wells and combination wells are respectively milled out of 1.2 mm and 2 mm polystyrene, then bonded together via acetonitrile-assisted heat bonding. In this configuration the variable wells and the combination wells face opposite directions. Holders for the device (to keep the device suspended) was fabricated with polylactic acid (PLA) polymer using a fused deposition modeling (FDM) 3D printer (Ultimaker 3) and placed in an OmniTray single-well plate (Thermo Scientific Nunc). Luria-Bertani (LB) agar was prepared and sterilized in an autoclave, then pipetted into the μCFL device using a 20 μL pipet while warm (15 μL of LB agar was pipetted into the variable wells first and allowed to solidify, followed by flipping the device over and pipetting 17 μL of LB agar into the combination wells.)

6.5.2 Microbial Culture

The 10 rhizosphere bacterial strains and *B. cereus* GFP (plasmid-dependent) fluorescent reporter strain were cultured as reported previously[130]. Bacteria were grown in liquid culture overnight in 50% strength tryptic soy broth (TSB) at 28°C. Turbidity measurements of the liquid cultures were performed using an ELISA reader at 600 nm. Aliquots of cultures of each strain were centrifuged at 6,000 × g for 6 min, the supernatant was discarded, and the bacterial pellet was resuspended in PBS to an equivalent OD 600 of 0.01. For the variable wells of the μCFL device, 3 μL of 0.01 OD bacterial suspension (the tester strains) was dispensed on the agar surface using a 10 μL pipet. The device was then flipped over, allowing the combination wells to face upwards. Three microliters of 0.01 OD bacterial suspension (the target strains) were dispensed on the agar surface of the combination wells using a 10 μL pipet (either 6 h after or immediately after inoculating

the tester strains). Care was taken to not poke holes on the agar surface with the pipet tip (which can affect image analysis). The devices were then placed in a laminar flow hood for 15 min to allow the liquid on the agar to air dry. The devices were placed on a holder in an OmniTray, which was then sealed on the edges using parafilm to prevent evaporation and drying of the agar. Devices were incubated at RT for 2 days and bacterial growth was monitored using an epifluorescence microscope at set time points.

6.5.3 Fluorescence Microscopy

Imaging of microbial growth was performed using a Nikon Ti Eclipse inverted epifluorescence microscope equipped with a motorized xy stage. A stitched montage image of the whole device was acquired using a 2× objective in bright-field and two fluorescence channels: 390 nm (blue), and 485 nm (green).

6.5.4 Layout Generation and Image Processing

A custom layout generator script was written in MATLAB (The MathWorks, Natick, MA) to generate the layout for plating microbes in the variable wells. The script attempts to maximize combinatorial coverage on the device and minimize repeats. This was achieved by using a random number generator to determine which microbe would reside in each variable well. The number of combination wells containing each microbe was recorded and used to determine the probability distribution for placing each microbe in future wells. Microbes were then plated according to the generated layout. Following culture and image acquisition, the images were then loaded into Fiji (https://fiji.sc/). A custom ROI array was created using the ROI manager of Fiji to measure the mean fluorescence

intensity of each combination well and the three edges of the combination well. The measured fluorescence intensity values were then exported to a CSV file, then imported into MATLAB. We wrote a custom MATLAB script to map each ROI datapoint to the associated strain combination indicated by the custom layout generated previously.

6.5.5 Diffusion Experiments

Six-well μCFL devices with various dimensions ranging from a pitch of 4.5, 5.5, 6, and 6.5 mm (between 2 variable wells) were fabricated and filled with agar as described above. The volume of agar in each well was scaled proportionally according to the volume of the device. A 10 μg/mL solution of Rhodamine 6G (Millipore Sigma) solution in PBS was pipetted onto the surface of the agar in the variable well. Diffusion was monitored at 30 min intervals for 12 hours via time-lapse microscopy using a Nikon Ti Eclipse inverted epifluorescence microscope with the 560 nm excitation channel. A linear ROI was drawn in Fiji starting from the inner edge of the triangular combination well and ending at the midpoint of the outer side of the well to quantify the diffusion profile as reflected in the fluorescence intensity.

6.5.6 Finite Element Modeling

Modeling of diffusion in the μCFL device was performed using COMSOL Multiphysics software (COMSOL, Burlington, MA). A 3-dimensional model of the agar within the μCFL was drawn using AutoCAD and imported into COMSOL. For diffusion analysis, the *Transport of Diluted Species in Porous Media* module was used. The diffusion source was set at the top surface of the agar in the variable well, with a diffusion coefficient of 1

x 10^{-6} $cm^2 \cdot s^{-1}$ (similar to the diffusion coefficient of antibiotics in agar as previously reported[140]). The porosity of the agar was set to 0.9805 (the porosity of 2% agarose gel as previously reported[141]. A time-dependent simulation was performed with 30 min intervals across 12 hours corresponding to the Rhodamine 6G diffusion experiment.

6.6 Acknowledgments

We would like to thank Dr. Jay Warrick, and Dr. Scott Berry for helpful input and suggestions for the project. This study was funded by the National Institutes of Health (NIH P30CA014520), and Office of the Vice Chancellor for Research and Graduate Education SEED program and the State of Wisconsin.

Chapter 7

Conclusion

One of the main jobs of a biomedical engineer is to bridge the gap between 2 disparate scientific disciplines, engineering and biology. Much of my PhD work is aimed at closing that gap, which governs the design choices of simplicity, accessibility, robustness, and cost effectiveness. The “open” microfluidics concepts employed in my PhD work not only embodies a geometrical design form, but also a philosophy: in order for a technology to achieve maximal impact, it should be open and accessible for the broader scientific community, and not enshrouded in the ivory tower of engineering prowess. The engineering scientific academia generally places a high value on demonstrating engineering “capabilities”, whereas matters of reliability and accessibility are often not as emphasized or celebrated, which in fairness, doesn’t sound like a very “cool” achievement. However, bioengineering is in essence, a multidisciplinary field and thus accessibility should also be at the forefront of engineering design considerations. Since its early exploratory days in the 1970s, the microfluidics field has gradually evolved from demonstrating “capabilities” and has now entered the age of maturation and translation, which involves packaging the “capabilities” into a user-easily-accessible form. A first step is bringing the technology to professional users such as biologists and clinicians, and ultimately, into the hands of the masses: the untrained average user. I hope this dissertation can contribute to a step in that direction, and towards realizing the ultimate goal of ambient diagnostics.

Bibliography

1 Pritchard, C. C. *et al.* Inherited DNA-Repair Gene Mutations in Men with Metastatic Prostate Cancer. *New Engl J Med* **375**, 443-453, doi:10.1056/NEJMoa1603144 (2016).

2 Robinson, D. *et al.* Integrative clinical genomics of advanced prostate cancer. *Cell* **161**, 1215-1228, doi:10.1016/j.cell.2015.05.001 (2015).

3 Moore, L. D., Le, T. & Fan, G. P. DNA Methylation and Its Basic Function. *Neuropsychopharmacol* **38**, 23-38, doi:10.1038/npp.2012.112 (2013).

4 Seto, E. & Yoshida, M. Erasers of Histone Acetylation: The Histone Deacetylase Enzymes. *Csh Perspect Biol* **6**, doi:10.1101/cshperspect.a018713 (2014).

5 Clouaire, T. & Stancheva, I. Methyl-CpG binding proteins: specialized transcriptional repressors or structural components of chromatin? *Cell Mol Life Sci* **65**, 1509-1522, doi:10.1007/s00018-008-7324-y (2008).

6 Yegnasubramanian, S. *et al.* Chromosome-wide mapping of DNA methylation patterns in normal and malignant prostate cells reveals pervasive methylation of gene-associated and conserved intergenic sequences. *Bmc Genomics* **12**, doi:10.1186/1471-2164-12-313 (2011).

7 Yegnasubramanian, S. *et al.* DNA Hypomethylation Arises Later in Prostate Cancer Progression than CpG Island Hypermethylation and Contributes to Metastatic Tumor Heterogeneity. *Cancer Res* **68**, 8954-8967, doi:10.1158/0008-5471.Can-07-6088 (2008).

8 Kulis, M. & Esteller, M. DNA methylation and cancer. *Adv Genet* **70**, 27-56, doi:10.1016/B978-0-12-380866-0.60002-2 (2010).

9 Li, L. C., Carroll, P. R. & Dahiya, R. Epigenetic changes in prostate cancer: Implication for diagnosis and treatment. *Jnci-J Natl Cancer I* **97**, 103-115, doi:10.1093/jnci/dji010 (2005).

10 Greenleaf, W. J. Assaying the epigenome in limited numbers of cells. *Methods* **72**, 51-56, doi:10.1016/j.ymeth.2014.10.010 (2015).

11 Lee, W. H. *et al.* Cytidine Methylation of Regulatory Sequences near the Pi-Class Glutathione-S-Transferase Gene Accompanies Human Prostatic Carcinogenesis. *P Natl Acad Sci USA* **91**, 11733-11737, doi:10.1073/pnas.91.24.11733 (1994).

12 Cairns, P. *et al.* Molecular detection of prostate cancer in urine by GSTP1 hypermethylation. *Clinical Cancer Research* **7**, 2727-2730 (2001).

13 Nakayama, M. *et al.* GSTP1 CpG island hypermethylation as a molecular biomarker for prostate cancer. *J Cell Biochem* **91**, 540-552, doi:10.1002/jcb.10740 (2004).

14 Darst, R. P., Pardo, C. E., Ai, L., Brown, K. D. & Kladde, M. P. Bisulfite sequencing of DNA. *Curr Protoc Mol Biol* **Chapter 7**, Unit 7 9 1-17, doi:10.1002/0471142727.mb0709s91 (2010).

15 Yegnasubramanian, S., Lin, X., Haffner, M. C., DeMarzo, A. M. & Nelson, W. G. Combination of methylated-DNA precipitation and methylation-sensitive restriction enzymes (COMPARE-MS) for the rapid, sensitive and quantitative detection of DNA methylation. *Nucleic Acids Res* **34**, e19, doi:10.1093/nar/gnj022 (2006).

16 Manz, A., Graber, N. & Widmer, H. M. Miniaturized Total Chemical-Analysis Systems - a Novel Concept for Chemical Sensing. *Sensor Actuat B-Chem* **1**, 244-248, doi:10.1016/0925-4005(90)80209-I (1990).

17 Berry, S. M., Alarid, E. T. & Beebe, D. J. One-step purification of nucleic acid for gene expression analysis via Immiscible Filtration Assisted by Surface Tension (IFAST). *Lab Chip* **11**, 1747-1753, doi:10.1039/c1lc00004g (2011).

18 Berry, S. M. *et al.* HIV viral RNA extraction in wax immiscible filtration assisted by surface tension (IFAST) devices. *J Mol Diagn* **16**, 297-304, doi:10.1016/j.jmoldx.2014.01.004 (2014).

19 Berry, S. M., Regehr, K. J., Casavant, B. P. & Beebe, D. J. Automated operation of immiscible filtration assisted by surface tension (IFAST) arrays for streamlined analyte isolation. *J Lab Autom* **18**, 206-211, doi:10.1177/2211068212462023 (2013).

20 Berry, S. M., Strotman, L. N., Kueck, J. D., Alarid, E. T. & Beebe, D. J. Purification of cell subpopulations via immiscible filtration assisted by surface tension (IFAST). *Biomed Microdevices* **13**, 1033-1042, doi:10.1007/s10544-011-9573-z (2011).

21 Casavant, B. P. *et al.* The VerIFAST: an integrated method for cell isolation and extracellular/intracellular staining. *Lab Chip* **13**, 391-396, doi:10.1039/c2lc41136a (2013).

22 Juang, D. S., Berry, S. M., Li, C., Lang, J. M. & Beebe, D. J. Centrifugation-Assisted Immiscible Fluid Filtration for Dual-Bioanalyte Extraction. *Anal Chem* **91**, 11848-11855, doi:10.1021/acs.analchem.9b02572 (2019).

23 Li, C., Niles, D. J., Juang, D. S., Lang, J. M. & Beebe, D. J. Automated System for Small-Population Single-Particle Processing Enabled by Exclusive Liquid Repellency. *SLAS Technol* **24**, 535-542, doi:10.1177/2472630319853219 (2019).

24 Li, C. *et al.* Double-exclusive liquid repellency (double-ELR): an enabling technology for rare phenotype analysis. *Lab on a Chip* **18**, 2710-2719, doi:10.1039/c8lc00584b (2018).

25 Li, C. *et al.* Exclusive Liquid Repellency: An Open Multi-Liquid-Phase Technology for Rare Cell Culture and Single-Cell Processing. *Acs Appl Mater Inter* **10**, 17065-17070, doi:10.1021/acsami.8b03627 (2018).

26 Wang, H. *et al.* Phase-adjusted estimation of the number of Coronavirus Disease 2019 cases in Wuhan, China. *Cell Discov* **6**, 10, doi:10.1038/s41421-020-0148-0 (2020).

27 Hui, D. S. *et al.* The continuing 2019-nCoV epidemic threat of novel coronaviruses to global health - The latest 2019 novel coronavirus outbreak in Wuhan, China. *Int J Infect Dis* **91**, 264-266, doi:10.1016/j.ijid.2020.01.009 (2020).

28 Conti, K. M. a. S. Grenova's Plan to Stop Supply Shortages in COVID-19 Testing Labs. (2020). https://richmondgrid.com/grenovas-plan-to-stop-supply-shortages-in-covid-19-testing-labs/.

29 Wu, K. J. Coronavirus testing labs again lack key supplies. *The New York Times* https://www.nytimes.com/2020/07/23/health/coronavirus-testing-supplyshortage.html (2020).

30 Notomi, T. *et al.* Loop-mediated isothermal amplification of DNA. *Nucleic Acids Research* **28**, doi:10.1093/nar/28.12.e63 (2000).

31 Tanner, N. A., Zhang, Y. H. & Evans, T. C. Visual detection of isothermal nucleic acid amplification using pH-sensitive dyes. *Biotechniques* **58**, 59-68, doi:10.2144/000114253 (2015).

32 Berry, S. M. *et al.* Weak protein-protein interactions revealed by immiscible filtration assisted by surface tension. *Anal Biochem* **447**, 133-140, doi:10.1016/j.ab.2013.10.038 (2014).

33 Casavant, B. P., Guckenberger, D. J., Beebe, D. J. & Berry, S. M. Efficient Sample Preparation from Complex Biological Samples Using a Sliding Lid for Immobilized Droplet Extractions. *Anal Chem* **86**, 6355-6362, doi:10.1021/ac500574t (2014).

34 Berry, S. M. *et al.* AirJump: Using Interfaces to Instantly Perform Simultaneous Extractions. *Acs Appl Mater Inter* **8**, 15040-15045, doi:10.1021/acsami.6b02555 (2016).

35 MagNA Pure 96 Instrument. High-throughput robotic workstation for fully automated purification of nucleic acids from up to 96 samples. *Roche Molecular Systems Inc.* https://lifescience.roche.com/en_us/products/magna-pure-96-instrument-382411-1.html (2020).

36 Applied Biosystems™ MagMAXTM-96 Viral RNA Isolation Kit. *Thermo Fisher Scientific Inc.* https://www.thermofisher.com/order/catalog/product/AM1836#/AM1836 (2017).

37 Magnetic bead-based isolation of viral RNA/DNA and bacterial DNA—NucleoMag Pathogen. *Takara Bio Inc.* https://www.takarabio.com/products/nucleic-acid-purification/viral-dna-and-rna-purification-kits/nucleomag-pathogen (2017).

38 Boom, R. *et al.* Rapid and Simple Method for Purification of Nucleic-Acids. *J Clin Microbiol* **28**, 495-503, doi:10.1128/Jcm.28.3.495-503.1990 (1990).

39 Escobar, M. D. & Hunt, J. L. A cost-effective RNA extraction technique from animal cells and tissue using silica columns. *J Biol Methods* **4**, doi:10.14440/jbm.2017.184 (2017).

40 He, H. *et al.* Integrated DNA and RNA extraction using magnetic beads from viral pathogens causing acute respiratory infections. *Sci Rep-Uk* **7**, doi:10.1038/srep45199 (2017).

41 Oberacker, P. *et al.* Bio-On-Magnetic-Beads (BOMB): Open platform for high-throughput nucleic acid extraction and manipulation. *Plos Biol* **17**, doi:10.1371/journal.pbio.3000107 (2019).

42 Yaffe, H. *et al.* LogSpin: a simple, economical and fast method for RNA isolation from infected or healthy plants and other eukaryotic tissues. *BMC Res Notes* **5**, 45, doi:10.1186/1756-0500-5-45 (2012).

43 Scallan, M. F. *et al.* Validation of a Lysis Buffer Containing 4 M Guanidinium Thiocyanate (GITC)/ Triton X-100 for Extraction of SARS-CoV-2 RNA for COVID-19 Testing: Comparison of Formulated Lysis Buffers Containing 4 to 6 M GITC, Roche External Lysis Buffer and Qiagen RTL Lysis Buffer. *bioRxiv*, 2020.2004.2005.026435, doi:10.1101/2020.04.05.026435 (2020).

44 Broughton, J. P. *et al.* CRISPR-Cas12-based detection of SARS-CoV-2. *Nat Biotechnol* **38**, 870-874, doi:10.1038/s41587-020-0513-4 (2020).

45 Broughton JP, D. W., Fasching CL, Singh J, Chiu CY, Chen JS. A protocol for rapid detection of the 2019 novel coronavirus SARS-CoV-2 using CRISPR diagnostics: SARS-CoV-2 DETECTR. *Mammoth Biosciences Inc.* https://mammoth.bio/wp-content/uploads/2020/03/Mammoth-Biosciences-A-protocol-for-rapid-detection-of-SARS-CoV-2-using-CRISPR-diagnostics-DETECTR.pdf (2020).

46 Color Genomics SARS-CoV-2 LAMP Diagnostic Assay Version 1.2. *Color Genomics Inc.* https://www.color.com/wp-content/uploads/2020/05/Color-LAMP-Diagnostic-Assay_v1-2_Updated-052120.pdf (2020).

47 Rabe, B. A. & Cepko, C. SARS-CoV-2 detection using isothermal amplification and a rapid, inexpensive protocol for sample inactivation and purification. *P Natl Acad Sci USA* **117**, 24450-24458, doi:10.1073/pnas.2011221117 (2020).

48 Curtis, K. A. *et al.* A multiplexed RT-LAMP assay for detection of group M HIV-1 in plasma or whole blood. *J Virol Methods* **255**, 91-97, doi:10.1016/j.jviromet.2018.02.012 (2018).

49 BEI Certificate of Analysis for product NR-52286 SARS-Related Coronavirus 2, Isolate USAWA1/2020, Heat Inactivated. *BEI Resources*. https://www.beiresources.org/Catalog/antigen/NR-52286.aspx (2020).

50 Pollack, M. G., Fair, R. B. & Shenderov, A. D. Electrowetting-based actuation of liquid droplets for microfluidic applications. *Appl Phys Lett* **77**, 1725-1726, doi:10.1063/1.1308534 (2000).

51 Pollack, M. G., Shenderov, A. D. & Fair, R. B. Electrowetting-based actuation of droplets for integrated microfluidics. *Lab on a Chip* **2**, 96-101, doi:10.1039/b110474h (2002).

52 Velev, O. D., Prevo, B. G. & Bhatt, K. H. On-chip manipulation of free droplets. *Nature* **426**, 515-516, doi:10.1038/426515a (2003).

53 Hunt, T. P., Issadore, D. & Westervelt, R. M. Integrated circuit/microfluidic chip to programmably trap and move cells and droplets with dielectrophoresis. *Lab on a Chip* **8**, 81-87, doi:10.1039/b710928h (2008).

54 Zhang, Y. & Nguyen, N. T. Magnetic digital microfluidics - a review. *Lab on a Chip* **17**, 994-1008, doi:10.1039/c7lc00025a (2017).

55 Lehmann, U. *et al.* Two-dimensional magnetic manipulation of microdroplets on a chip as a platform for bioanalytical applications. *Sensor Actuat B-Chem* **117**, 457-463, doi:10.1016/j.snb.2005.12.053 (2006).

56 Rezk, A. R., Manor, O., Friend, J. R. & Yeo, L. Y. Unique fingering instabilities and soliton-like wave propagation in thin acoustowetting films. *Nat Commun* **3**, doi:10.1038/ncomms2168 (2012).

57 Renaudin, A., Tabourier, P., Camart, J. C. & Druon, C. Surface acoustic wave two-dimensional transport and location of microdroplets using echo signal. *J Appl Phys* **100**, doi:10.1063/1.2388725 (2006).

58 Miller, E. M., Ng, A. H. C., Uddayasankar, U. & Wheeler, A. R. A digital microfluidic approach to heterogeneous immunoassays. *Anal Bioanal Chem* **399**, 337-345, doi:10.1007/s00216-010-4368-2 (2011).

59 Huang, C. Y. *et al.* A highly efficient bead extraction technique with low bead number for digital microfluidic immunoassay. *Biomicrofluidics* **10**, doi:10.1063/1.4939942 (2016).

60 Neoprep library prep system. *Illumina Inc.* https://support.illumina.com/content/dam/illumina-marketing/documents/products/brochures/brochure-neoprep.pdf (2018).

61 VolTRAX. Automated sample prep for nanopore analyses. *Oxford Nanopore Technologies Inc.* https://nanoporetech.com/products/voltrax (2016).

62 Li, J. & Kim, C. J. Current commercialization status of electrowetting-on-dielectric (EWOD) digital microfluidics. *Lab on a Chip* **20**, 1705-1712, doi:10.1039/d0lc00144a (2020).

63 Miller, E. M. & Wheeler, A. R. A digital microfluidic approach to homogeneous enzyme assays. *Anal Chem* **80**, 1614-1619, doi:10.1021/ac702269d (2008).

64 Sista, R. S. *et al.* Digital Microfluidic Platform for Multiplexing Enzyme Assays: Implications for Lysosomal Storage Disease Screening in Newborns. *Clin Chem* **57**, 1444-1451, doi:10.1373/clinchem.2011.163139 (2011).

65 Robison, K. in *Omics! Omics!* Vol. 2021 (2017).

66 Jebrail, M. J., Bartsch, M. S. & Patel, K. D. Digital microfluidics: a versatile tool for applications in chemistry, biology and medicine. *Lab on a Chip* **12**, 2452-2463, doi:10.1039/c2lc40318h (2012).

67 Samiei, E., Tabrizian, M. & Hoorfar, M. A review of digital microfluidics as portable platforms for lab-on a-chip applications. *Lab on a Chip* **16**, 2376-2396, doi:10.1039/c6lc00387g (2016).

68 Yoon, J. Y. & Garrell, R. L. Preventing biomolecular adsorption in electrowetting-based biofluidic chips. *Anal Chem* **75**, 5097-5102, doi:10.1021/ac0342673 (2003).

69 Yang, H., Luk, V. N., Abeigawad, M., Barbulovic-Nad, I. & Wheeler, A. R. A World-to-Chip Interface for Digital Microfluidics. *Anal Chem* **81**, 1061-1067, doi:10.1021/ac802154h (2009).

70 Newman, S. *et al.* High density DNA data storage library via dehydration with digital microfluidic retrieval. *Nat Commun* **10**, doi:10.1038/s41467-019-09517-y (2019).

71 Cho, S. K., Moon, H. J. & Kim, C. J. Creating, transporting, cutting, and merging liquid droplets by electrowetting-based actuation for digital microfluidic circuits. *J Microelectromech S* **12**, 70-80, doi:10.1109/Jmems.2002.807467 (2003).

72 Ng, A. H. C., Choi, K., Luoma, R. P., Robinson, J. M. & Wheeler, A. R. Digital Microfluidic Magnetic Separation for Particle-Based Immunoassays. *Anal Chem* **84**, 8805-8812, doi:10.1021/ac3020627 (2012).

73 Zhao, Y. & Chakrabarty, K. Cross-Contamination Avoidance for Droplet Routing in Digital Microfluidic Biochips. *Des Aut Test Europe*, 1290-1295 (2009).

74 Lin, C. C. Y. & Chang, Y. W. Cross-Contamination Aware Design Methodology for Pin-Constrained Digital Microfluidic Biochips. *Des Aut Con*, 641-646 (2010).

75 Mensink, M. A., Frijlink, H. W., Maarschalk, K. V. & Hinrichs, W. L. J. How sugars protect proteins in the solid state and during drying (review): Mechanisms of stabilization in relation to stress conditions. *Eur J Pharm Biopharm* **114**, 288-295, doi:10.1016/j.ejpb.2017.01.024 (2017).

76 Cleland, J. L. *et al.* A specific molar ratio of stabilizer to protein is required for storage stability of a lyophilized monoclonal antibody. *J Pharm Sci* **90**, 310-321, doi:10.1002/1520-6017(200103)90:3<310::Aid-Jps6>3.0.Co;2-R (2001).

77 Maurice, N. M., Bedi, B. & Sadikot, R. T. Pseudomonas aeruginosa Biofilms: Host Response and Clinical Implications in Lung Infections. *Am J Resp Cell Mol* **58**, 428-439, doi:10.1165/rcmb.2017-0321TR (2018).

78 Yu, H. M., Meyvantsson, I., Shkel, I. A. & Beebe, D. J. Diffusion dependent cell behavior in microenvironments. *Lab on a Chip* **5**, 1089-1095, doi:10.1039/b504403k (2005).

79 Tan, S. C. & Yiap, B. C. DNA, RNA, and protein extraction: the past and the present. *J Biomed Biotechnol* **2009**, 574398, doi:10.1155/2009/574398 (2009).

80 Cui, F., Rhee, M., Singh, A. & Tripathi, A. Microfluidic Sample Preparation for Medical Diagnostics. *Annu Rev Biomed Eng* **17**, 267-286, doi:10.1146/annurev-bioeng-071114-040538 (2015).

81 Zou, Y. P. *et al.* Nucleic acid purification from plants, animals and microbes in under 30 seconds. *Plos Biol* **15**, doi:10.1371/journal.pbio.2003916 (2017).

82 Zhang, C. S., Xu, J. L., Ma, W. L. & Zheng, W. L. PCR microfluidic devices for DNA amplification. *Biotechnol Adv* **24**, 243-284, doi:10.1016/j.biotechadv.2005.10.002 (2006).

83 Ali, N., Rampazzo, R. D. P., Costa, A. D. T. & Krieger, M. A. Current Nucleic Acid Extraction Methods and Their Implications to Point-of-Care Diagnostics. *Biomed Res Int*, doi:10.1155/2017/9306564 (2017).

84 Chomczynski, P. & Sacchi, N. Single-step method of RNA isolation by acid guanidinium thiocyanate-phenol-chloroform extraction. *Anal Biochem* **162**, 156-159, doi:10.1006/abio.1987.9999 (1987).

85 Chomczynski, P. & Sacchi, N. The single-step method of RNA isolation by acid guanidinium thiocyanate-phenol-chloroform extraction: twenty-something years on. *Nat Protoc* **1**, 581-585, doi:10.1038/nprot.2006.83 (2006).

86 Kingston, R. E., Chomczynski, P. & Sacchi, N. Guanidine methods for total RNA preparation. *Curr Protoc Mol Biol* **Chapter 4**, Unit4 2, doi:10.1002/0471142727.mb0402s36 (2001).

87 Tesena, P., Korchunjit, W., Taylor, J. & Wongtawan, T. Comparison of commercial RNA extraction kits and qPCR master mixes for studying gene expression in small biopsy tissue samples from the equine gastric epithelium. *J Equine Sci* **28**, 135-141, doi:10.1294/jes.28.135 (2017).

88 Nacham, O., Clark, K. D., Varona, M. & Anderson, J. L. Selective and Efficient RNA Analysis by Solid-Phase Microextraction. *Anal Chem* **89**, 10661-10666, doi:10.1021/acs.analchem.7b02733 (2017).

89 Katevatis, C., Fan, A. & Klapperich, C. M. Low concentration DNA extraction and recovery using a silica solid phase. *Plos One* **12**, doi:10.1371/journal.pone.0176848 (2017).

90 Tian, H., Huhmer, A. F. & Landers, J. P. Evaluation of silica resins for direct and efficient extraction of DNA from complex biological matrices in a miniaturized format. *Anal Biochem* **283**, 175-191, doi:10.1006/abio.2000.4577 (2000).

91 Berensmeier, S. Magnetic particles for the separation and purification of nucleic acids. *Appl Microbiol Biotechnol* **73**, 495-504, doi:10.1007/s00253-006-0675-0 (2006).

92 Adams, N. M. *et al.* Comparison of three magnetic bead surface functionalities for RNA extraction and detection. *ACS Appl Mater Interfaces* **7**, 6062-6069, doi:10.1021/am506374t (2015).

93 Zhang, R., Gong, H. Q., Zeng, X., Lou, C. & Sze, C. A microfluidic liquid phase nucleic acid purification chip to selectively isolate DNA or RNA from low copy/single bacterial cells in minute sample volume followed by direct on-chip quantitative PCR assay. *Anal Chem* **85**, 1484-1491, doi:10.1021/ac3026509 (2013).

94 Xiang, X., Qiu, D., Hegele, R. D. & Tan, W. C. Comparison of different methods of total RNA extraction for viral detection in sputum. *J Virol Methods* **94**, 129-135 (2001).

95 Muyal, J. P., Muyal, V., Kaistha, B. P., Seifart, C. & Fehrenbach, H. Systematic comparison of RNA extraction techniques from frozen and fresh lung tissues: checkpoint towards gene expression studies. *Diagn Pathol* **4**, 9, doi:10.1186/1746-1596-4-9 (2009).

96 Strotman, L. N., Lin, G. Y., Berry, S. M., Johnson, E. A. & Beebe, D. J. Facile and rapid DNA extraction and purification from food matrices using IFAST (immiscible filtration assisted by surface tension). *Analyst* **137**, 4023-4028, doi:10.1039/c2an35506j (2012).

97 Berry, S. M., Maccoux, L. J. & Beebe, D. J. Streamlining Immunoassays with Immiscible Filtrations Assisted by Surface Tension. *Anal Chem* **84**, 5518-5523, doi:10.1021/ac300085m (2012).

98 Cui, F. R., Wang, J. J., Opal, S. M. & Tripathi, A. Isolating Influenza RNA from Clinical Samples Using Microfluidic Oil-Water Interfaces. *Plos One* **11**, doi:10.1371/journal.pone.0149522 (2016).

99 Bordelon, H. *et al.* Development of a Low-Resource RNA Extraction Cassette Based on Surface Tension Valves. *Acs Appl Mater Inter* **3**, 2161-2168, doi:10.1021/am2004009 (2011).

100 Sur, K. *et al.* Immiscible Phase Nucleic Acid Purification Eliminates PCR Inhibitors with a Single Pass of Paramagnetic Particles through a Hydrophobic Liquid. *J Mol Diagn* **12**, 620-628, doi:10.2353/jmoldx.2010.090190 (2010).

101 Sperger, J. M. *et al.* Integrated Analysis of Multiple Biomarkers from Circulating Tumor Cells Enabled by Exclusion-Based Analyte Isolation. *Clin Cancer Res* **23**, 746-756, doi:10.1158/1078-0432.CCR-16-1021 (2017).

102 Juang, D. S. & Hsu, C. H. Self-concentrating buoyant glass microbubbles for high sensitivity immunoassays. *Lab Chip* **16**, 459-464, doi:10.1039/c5lc01005e (2016).

103 Gobel, J. G. & Joppien, G. R. Dynamic interfacial tensions of aqueous triton X-100 solutions in contact with air, cyclohexane, n-heptane, and n-hexadecane. *J Colloid Interf Sci* **191**, 30-37, doi:10.1006/jcis.1997.4949 (1997).

104 Phongikaroon, S., Hoffmaster, R., Judd, K. P., Smith, G. B. & Handler, R. A. Effect of temperature on the surface tension of soluble and insoluble Surfactants of hydrodynamical importance. *J Chem Eng Data* **50**, 1602-1607, doi:10.1021/je050074w (2005).

105 Hsu, C. H., Chen, C., Irimia, D. & Toner, M. Fast sorting of CD4+ T cells from whole blood using glass microbubbles. *Technology* **3**, 38-44, doi:10.1142/S2339547815500016 (2015).

106 Key, B. D., Howell, R. D. & Criddle, C. S. Fluorinated organics in the biosphere. *Environ Sci Technol* **31**, 2445-2454, doi:10.1021/es961007c (1997).

107 Ainsworth, C. Therapeutic microbes to tackle disease. *Nature* **577**, S20-S22, doi:10.1038/d41586-020-00201-6 (2020).

108 Charbonneau, M. R., Isabella, V. M., Li, N. & Kurtz, C. B. Developing a new class of engineered live bacterial therapeutics to treat human diseases. *Nat Commun* **11**, 1738, doi:10.1038/s41467-020-15508-1 (2020).

109 Lu, T. K., Mimee, M., Citorik, R. J. & Pepper, K. Engineering the Microbiome for Human Health Applications. *Chemistry of Microbiomes*, 65-75 (2017).

110 Huttenhower, C. *et al.* Structure, function and diversity of the healthy human microbiome. *Nature* **486**, 207-214, doi:10.1038/nature11234 (2012).

111 Clavel, T., Lagkouvardos, I. & Hiergeist, A. Microbiome sequencing: challenges and opportunities for molecular medicine. *Expert Rev Mol Diagn* **16**, 795-805, doi:10.1080/14737159.2016.1184574 (2016).

112 Welch, J. L. M., Rossetti, B. J., Rieken, C. W., Dewhirst, F. E. & Borisy, G. G. Biogeography of a human oral microbiome at the micron scale. *P Natl Acad Sci USA* **113**, E791-E800, doi:10.1073/pnas.1522149113 (2016).

113 Earle, K. A. *et al.* Quantitative Imaging of Gut Microbiota Spatial Organization. *Cell Host Microbe* **18**, 478-488, doi:10.1016/j.chom.2015.09.002 (2015).

114 Kerr, B., Riley, M. A., Feldman, M. W. & Bohannan, B. J. M. Local dispersal promotes biodiversity in a real-life game of rock-paper-scissors. *Nature* **418**, 171-174, doi:10.1038/nature00823 (2002).

115 Powers, M. J., Sanabria-Valentin, E., Bowers, A. A. & Shank, E. A. Inhibition of Cell Differentiation in Bacillus subtilis by Pseudomonas protegens. *J Bacteriol* **197**, 2129-2138, doi:10.1128/Jb.02535-14 (2015).

116 Terekhov, S. S. *et al.* Ultrahigh-throughput functional profiling of microbiota communities. *P Natl Acad Sci USA* **115**, 9551-9556, doi:10.1073/pnas.1811250115 (2018).

117 Hsu, R. H. *et al.* Microbial Interaction Network Inference in Microfluidic Droplets. *Cell Syst* **9**, 229-+, doi:10.1016/j.cels.2019.06.008 (2019).

118 Kehe, J. *et al.* Massively parallel screening of synthetic microbial communities. *P Natl Acad Sci USA* **116**, 12804-12809, doi:10.1073/pnas.1900102116 (2019).

119 Park, J., Kerner, A., Burns, M. A. & Lin, X. X. N. Microdroplet-Enabled Highly Parallel Co-Cultivation of Microbial Communities. *Plos One* **6**, doi:10.1371/journal.pone.0017019 (2011).

120 Gude, S. *et al.* Bacterial coexistence driven by motility and spatial competition. *Nature* **578**, 588-+, doi:10.1038/s41586-020-2033-2 (2020).

121 Connell, J. L., Ritschdorff, E. T., Whiteley, M. & Shear, J. B. 3D printing of microscopic bacterial communities. *P Natl Acad Sci USA* **110**, 18380-18385, doi:10.1073/pnas.1309729110 (2013).

122 Hong, S. H. *et al.* Synthetic quorum-sensing circuit to control consortial biofilm formation and dispersal in a microfluidic device. *Nat Commun* **3**, doi:10.1038/ncomms1616 (2012).

123 Barkal, L. J., Berthier, E., Theberge, A. B., Keller, N. P. & Beebe, D. J. Multikingdom microscale models. *Plos Pathog* **13**, doi:10.1371/journal.ppat.1006424 (2017).

124 Mohan, R. *et al.* A microfluidic approach to study the effect of bacterial interactions on antimicrobial susceptibility in polymicrobial cultures. *Rsc Adv* **5**, 35211-35223, doi:10.1039/c5ra04092b (2015).

125 Kim, H. J., Boedicker, J. Q., Choi, J. W. & Ismagilov, R. F. Defined spatial structure stabilizes a synthetic multispecies bacterial community. *P Natl Acad Sci USA* **105**, 18188-18193, doi:10.1073/pnas.0807935105 (2008).

126 Svoboda, P., Lindstrom, E. S., Osman, O. A. & Langenheder, S. Dispersal timing determines the importance of priority effects in bacterial communities. *Isme J* **12**, 644-646, doi:10.1038/ismej.2017.180 (2018).

127 Sprockett, D., Fukami, T. & Relman, D. A. Role of priority effects in the early-life assembly of the gut microbiota. *Nat Rev Gastro Hepat* **15**, 197-205, doi:10.1038/nrgastro.2017.173 (2018).

128 Martinez, I. *et al.* Experimental evaluation of the importance of colonization history in early-life gut microbiota assembly. *Elife* **7**, doi:10.7554/eLife.36521 (2018).

129 Gutierrez, A. *et al.* Understanding and Sensitizing Density-Dependent Persistence to Quinolone Antibiotics. *Mol Cell* **68**, 1147-+, doi:10.1016/j.molcel.2017.11.012 (2017).

130 Lozano, G. L. *et al.* Introducing THOR, a Model Microbiome for Genetic Dissection of Community Behavior. *Mbio* **10**, doi:10.1128/mBio.02846-18 (2019).

131 Zeevi, D. *et al.* Personalized Nutrition by Prediction of Glycemic Responses. *Cell* **163**, 1079-1094, doi:10.1016/j.cell.2015.11.001 (2015).

132 Turnbaugh, P. J. *et al.* A core gut microbiome in obese and lean twins. *Nature* **457**, 480-U487, doi:10.1038/nature07540 (2009).

133 Sampson, T. R. *et al.* Gut Microbiota Regulate Motor Deficits and Neuroinflammation in a Model of Parkinson's Disease. *Cell* **167**, 1469-+, doi:10.1016/j.cell.2016.11.018 (2016).

134 Wu, S. C., Cao, Z. S., Chang, K. M. & Juang, J. L. Intestinal microbial dysbiosis aggravates the progression of Alzheimer's disease in Drosophila. *Nat Commun* **8**, 24, doi:10.1038/s41467-017-00040-6 (2017).

135 Vogt, N. M. *et al.* Gut microbiome alterations in Alzheimer's disease. *Sci Rep* **7**, 13537, doi:10.1038/s41598-017-13601-y (2017).

136 Helmink, B. A., Khan, M. A. W., Hermann, A., Gopalakrishnan, V. & Wargo, J. A. The microbiome, cancer, and cancer therapy. *Nat Med* **25**, 377-388, doi:10.1038/s41591-019-0377-7 (2019).

137 von Martels, J. Z. H. *et al.* The role of gut microbiota in health and disease: In vitro modeling of host-microbe interactions at the aerobe-anaerobe interphase of the human gut. *Anaerobe* **44**, 3-12, doi:10.1016/j.anaerobe.2017.01.001 (2017).

138 Ozbakir, H. F., Anderson, N. T., Fan, K. C. & Mukherjee, A. Beyond the Green Fluorescent Protein: Biomolecular Reporters for Anaerobic and Deep-Tissue Imaging. *Bioconjugate Chem* **31**, 293-302, doi:10.1021/acs.bioconjchem.9b00688 (2020).

139 Guckenberger, D. J., de Groot, T. E., Wan, A. M. D., Beebe, D. J. & Young, E. W. K. Micromilling: a method for ultra-rapid prototyping of plastic microfluidic devices. *Lab on a Chip* **15**, 2364-2378, doi:10.1039/c5lc00234f (2015).

140 Meulemans, A., Paycha, F., Hannoun, P. & Vulpillat, M. Measurement and Clinical and Pharmacokinetic Implications of Diffusion-Coefficients of Antibiotics in Tissues. *Antimicrob Agents Ch* **33**, 1286-1290, doi:10.1128/Aac.33.8.1286 (1989).

141 Pluen, A., Netti, P. A., Jain, R. K. & Berk, D. A. Diffusion of macromolecules in agarose gels: Comparison of linear and globular configurations. *Biophys J* **77**, 542-552, doi:10.1016/S0006-3495(99)76911-0 (1999).

Appendix

Additional Tables:

- From Chapter 3: Table A.1 and Table A.2
- From Chapter 6: Table A.3

Table A.1: Clinical sample results. (+) OIL-TAS positive, (−) OIL-TAS negative, (Δ) OIL-TAS inconclusive. Discrepant OIL-TAS results compared with RT-qPCR are highlighted in pink.

Sample ID	Medium	RT-qPCR Ct	OIL-TAS rep 1	OIL-TAS rep 2	OIL-TAS rep 3	OIL-TAS result (n=3)
1	PBS	19.32				+ 3/3
2	PBS	16.53				+ 3/3
3	RT M4	Neg				− 0/3
4	UTM	Neg				− 0/3
5	UTM	30.16				+ 3/3
6	PBS	18.71				+ 3/3
7	UTM	Neg				− 0/3
8	PBS	23.79				+ 3/3
9	RT M4	Neg				− 0/3
10	UTM	Neg				− 0/3
11	UTM	Neg				− 0/3
12	UTM	Neg				− 0/3
13	PBS	24.31				+ 3/3
14	RT M4	Neg				− 0/3
15	UTM	34.22				Δ 1/3
16	PBS	Neg				− 0/3
17	UTM	Neg				− 0/3
18	UTM	23.5				+ 3/3
19	UTM	28				+ 3/3
20	UTM	16.51				+ 3/3
21	UTM	17.3				+ 3/3

22	PBS	15.7				+ 3/3
23	UTM	39				– 0/3
24	UTM	28.9				+ 3/3
25	UTM	32				+ 3/3
26	UTM	17.5				+ 3/3
27	UTM	28.4				+ 3/3
28	UTM	23.1				+ 3/3
29	UTM	29.6				+ 3/3
30	UTM	25.8				+ 3/3
31	UTM	16.4				+ 3/3
32	UTM	19.4				+ 3/3
33	UTM	21.4				+ 3/3
34	UTM	23.2				+ 3/3
35	UTM	17.7				+ 3/3
36	UTM	20.5				+ 3/3
37	UTM	20				+ 3/3
38	UTM	21.3				+ 3/3
39	PBS	24				+ 3/3
40	UTM	18.5				+ 3/3
41	PBS	28.2				+ 3/3
42	PBS	15.5				+ 3/3
43	PBS	16.6				+ 3/3
44	PBS	16.5				+ 3/3

45	PBS	16.5				+ 3/3
46	PBS	28.5				+ 3/3
47	UTM	32.7				Δ 1/3
48	UTM	21.5				+ 3/3
49	UTM	23.9				+ 3/3
50	UTM	17.7				+ 3/3
51	UTM	25.5				+ 3/3
52	UTM	26.2				+ 3/3
53	UTM	21.5				+ 3/3
54	UTM	28.2				+ 3/3
55	UTM	18.2				+ 3/3
56	UTM	15.5				+ 3/3
57	UTM	25.4				+ 3/3
58	UTM	14.4				+ 3/3
59	UTM	23.9				+ 3/3
60	UTM	19.6				+ 3/3
61	UTM	18.5				+ 3/3
62	UTM	21.9				+ 3/3
63	UTM	30.3				+ 3/3
64	UTM	35.6				+ 3/3
65	UTM	18.7				+ 3/3
66	Saline	23.3				+ 3/3
67	Saline	36.5				− 0/3

Controls				
Sample ID	**Medium**	**Concentration**	**OIL-TAS Image**	**OIL-TAS result**
PC3	PBS	10^3 copies/μL		+
PC2	PBS	10^2 copies/μL		+
PC1	PBS	10^1 copies/μL		+
NC	PBS	0 copies/μL		−

Table A.2: LAMP primer sequences

Primer Set	Sequence
***N* gene**	
F3	AACACAAGCTTTCGGCAG
B3	GAAATTTGGATCTTTGTCATCC
FIP	TGCGGCCAATGTTTGTAATCAGCCAAGGAAATTTTGGGGAC
BIP	CGCATTGGCATGGAAGTCACTTTGATGGCACCTGTGTAG
LF	TTCCTTGTCTGATTAGTTC
LB	ACCTTCGGGAACGTGGTT
As1e	
F3	CGGTGGACAAATTGTCAC
B3	CTTCTCTGGATTTAACACACTT
FIP	TCAGCACACAAAGCCAAAAATTTATTTTTCTGTGCAAAGGAAATTAAGGAG
BIP	TATTGGTGGAGCTAAACTTAAAGCCTTTTCTGTACAATCCCTTTGAGTG
LF	TTACAAGCTTAAAGAATGTCTGAACACT
LB	TTGAATTTAGGTGAAACATTTGTCACG
RNase P	
F3	TTGATGAGCTGGAGCCA
B3	CACCCTCAATGCAGAGTC
FIP	GTGTGACCCTGAAGACTCGGTTTTAGCCACTGACTCGGATC
BIP	CCTCCGTGATATGGCTCTTCGTTTTTTTCTTACATGGCTCTGGTC
LF	ATGTGGATGGCTGAGTTGTT
LB	CATGCTGAGTACTGGACCTC

Table A.3: Growth of *B. cereus* GFP target strain in co-culture with 3-member tester microbial communities (data from Figure 6.11B).

ID	Tester microbe
1	*Sphingobacterium sp. CI01*
2	*Chryseobacterium sp. CI02*
3	*Flavobacterium johnsoniae CI04*
4	*Pseudomonas koreensis CI12*
5	*Pseudomonas sp. CI14*
6	*Achromobacter sp. CI16*
7	*Microbacterium sp. RI03*
8	*Paenibacillus sp. RI40*
9	*Agrobacterium tumefaciens RI12*
10	*Stenotrophomonas sp. RI33*

Tester community combination	Target strain growth (relative to control)
1,5,7	20.02%
1,2,5	21.84%
1,5,10	22.23%
2,3,4	24.99%
3,5,9	25.22%
4,5,6	27.13%
2,3,5	27.74%
1,5,9	28.07%
5,6,9	28.60%
4,5,8	29.09%

5,9,10	29.36%
5,8,9	29.49%
2,5,9	29.71%
5,6,10	30.83%
1,3,5	30.92%
1,5,6	31.14%
5,7,9	31.32%
5,8,10	31.39%
2,4,5	31.41%
3,4,5	32.56%
4,5,9	33.14%
1,7,9	33.31%
5,6,8	33.66%
1,5,8	33.66%
3,5,8	34.28%
4,5,10	34.88%
4,5,7	34.91%
3,5,7	35.31%
5,7,8	35.66%
2,5,10	36.37%
2,5,8	36.39%
5,6,7	37.91%
1,4,5	38.09%
3,5,10	38.37%
2,5,7	38.44%
5,7,10	40.32%

3,5,6	42.15%
1,3,7	43.43%
3,4,7	43.71%
1,2,10	44.79%
1,4,8	47.75%
2,5,6	48.18%
3,8,10	52.13%
1,2,8	61.85%
2,4,8	62.38%
1,2,7	68.29%
7,8,10	71.31%
3,4,8	71.83%
2,9,10	74.13%
1,2,3	75.89%
2,3,10	80.74%
2,4,7	85.25%
2,3,9	87.66%
1,8,10	92.65%
3,9,10	95.55%
4,8,10	96.47%
1,3,8	97.01%
4,9,10	97.24%
3,6,8	99.09%
2,3,7	104.21%
3,8,9	105.92%
2,8,10	106.60%

3,6,10	106.67%
2,6,8	106.68%
3,6,7	107.53%
4,7,9	107.72%
2,3,8	108.35%
4,8,9	108.63%
1,8,9	109.95%
8,9,10	110.98%
7,8,9	112.05%
6,7,8	112.50%
2,3,6	114.11%
1,4,6	118.31%
2,8,9	120.62%
6,7,9	120.65%
7,9,10	121.04%
1,7,10	121.80%
2,4,10	124.33%
4,7,8	125.50%
4,6,8	125.57%
3,4,9	126.30%
2,4,6	126.38%
2,6,9	127.74%
3,6,9	129.02%
1,7,8	129.53%
3,7,8	129.76%
1,3,9	130.57%

4,6,10	131.21%
1,4,9	134.37%
4,6,9	137.75%
1,3,4	138.73%
2,4,9	139.27%
3,7,9	142.65%
4,7,10	143.45%
6,8,10	144.24%
2,7,8	144.27%
6,9,10	147.45%
4,6,7	148.30%
1,6,10	149.67%
1,3,10	149.76%
3,4,6	150.07%
1,4,10	151.45%
2,7,10	152.94%
2,7,9	154.49%
3,4,10	155.15%
6,7,10	156.51%
3,7,10	157.69%
6,8,9	160.52%
1,2,4	167.82%
2,6,7	176.60%
1,2,9	178.84%
2,6,10	180.73%
1,9,10	189.60%

1,4,7	190.05%
1,6,8	193.79%
1,2,6	195.19%
1,6,9	199.81%
1,6,7	203.26%
1,3,6	218.12%